SURFACE CHEMISTRY ASPECTS OF FLOURITE AND BASTNAESITE FLOTATION SYSTEMS

by

Xia Zhang

A dissertation submitted to the faculty of
The University of Utah
in partial fulfillment of the requirements for the degree of

Doctor of Philosophy

Department of Metallurgical Engineering

The University of Utah

May 2014

The University of Utah Graduate School

STATEMENT OF DISSERTATION APPROVAL

The dissertation of **Xia Zhang**

has been approved by the following supervisory committee members:

Jan D. Miller	, Chair	**March 6, 2014** Date Approved
Xuming Wang	, Member	**March 6, 2014** Date Approved
Manoranjan Misra	, Member	**March 6, 2014** Date Approved
Michael L. Free	, Member	**March 6, 2014** Date Approved
Vladimir Hlady	, Member	**March 6, 2014** Date Approved

and by **Manoranjan Misra**, Chair of the Department of **Metallurgical Engineering**

and by David B. Kieda, Dean of The Graduate School.

ABSTRACT

In this dissertation research, the surface chemistry aspects of the alkaline earth semisoluble salt mineral fluorite (CaF_2) and the rare earth (RE) semisoluble mineral bastnaesite ((Ce, La) CO_3F) were investigated. The primary objective is to provide fundamental understanding of the surface chemistry features for both fluorite and bastnaesite minerals including the wetting characteristics, electrokinetic features as well as collector adsorption properties.

First, the surface chemistry aspects of fluorite were examined with particular interest in investigating the effect of crystal structure differences on the wettability as well as the surface charge characteristics. Results from contact angle measurements, MD simulations and sum frequency vibrational spectroscopy (SFVS) analysis indicate that the different fluorite surfaces (111, 100 and 110) exhibit different wettability features. The 111 surface exhibits moderate hydrophobicity, while the 100 and 110 surfaces are hydrophilic. Flat plate streaming potential measurements at the different fluorite surfaces show that cleaning procedure has a significant effect on the surface charge of fluorite surfaces. The controversial zeta potentials at different fluorite surfaces might be due to the different cleaning methods.

Then the surface chemistry features of bastnaesite including wetting characteristics, electrokinetics and hydroxamate adsorption at low concentrations were investigated. Effect of CO_2 pressure on the stability diagram of bastnaesite was considered and the surface charge properties from electrophoresis measurements were

explained using the stability diagram. Bastnaesite was found to be naturally hydrophilic from both contact angle measurement and MD simulations. The adsorption isotherm at low levels of hydroxamate adsorption was established by the solution depletion technique and contact angle measurements. The relationship between hydrophobicity and adsorption density was examined by MD simulations for the first time. The SFVS spectra indicate a well-ordered monolayer was formed at a hydroxamate concentration of about 1 $\times 10^{-4}$ M.

It is expected that the findings for this dissertation will provide fundamental understanding of the flotation chemistry for fluorite and bastnaesite, make improvements in procedures for the strategy of flotation chemistry and provide a foundation for improved flotation technology in the future.

TABLE OF CONTENTS

LIST OF TABLES

LIST OF FIGURES

ACKNOWLEDGEMENTS

I would like to express my sincere appreciation to my advisor, Professor Jan D. Miller, for all his mentorship, guidance, encouragement, and patience during my dissertation research. His mentorship is paramount and precious for my long-term career goals. I am always deeply touched and motivated by his passion, enthusiasm and devotion to science. He is a great mentor carrying immense knowledge. I learned a lot from him not only from the courses he taught but also the discussions we had regarding my dissertation research.

My appreciation is extended to my committee members: Dr. Vladimir Hlady, Dr. Manoranjan Misra**,** Dr. Michael Free, and Dr. Xuming Wang, for their precious time reviewing my dissertation and providing valuable comments. Particularly, I want to thank Dr. Xuming Wang for his help and advice for my dissertation research.

Thanks are extended to Dr. Hongfei Wang at Pacific Northwest National Lab and Dr. Zhou Lu from the Chinese Academy of Sciences for their help, advice and sharing of knowledge on SFVS. Thanks to Dr. Xihui Yin from Kemira and Dr. Hao Du from the Chinese Academy of Sciences for their great help in molecular dynamics simulations.

Thanks are also extended to all the faculty and staff in the Department of Metallurgical Engineering at the University of Utah for providing me this great opportunity working with researchers from all over the world. I would also like to thank Dr. Shoeleh Assemi for her help in this dissertation research and all my colleagues and friends for their support and encouragement during my dissertation research.

I am grateful to the Division of Chemical Sciences, Geosciences and Biosciences, Office of Basic Energy Sciences, of the U.S. Department of Energy through Grant Number DE-FG03-93ER14315 for their financial support on this research project.

Last, but not least, I would like to express my love and appreciation to my family and my husband for their support and encouragement all these years.

CHAPTER 1

INTRODUCTION

Semisoluble salt minerals are characterized by their ionic bonding and are distinguished from soluble salt minerals by their limited solubility in water. One group of semisoluble salt minerals are the alkaline earth minerals such as fluorite (CaF_2), calcite ($CaCO_{3)}$, and apatite ($Ca_5F\ (PO_4)_3$) as well as celestite ($SrSO_4$) and barite ($BaSO_4$). Many of these minerals occur together, which makes flotation separation difficult due to similarities in their surface properties (Marinakis and Shergold, 1985). Another group of semisoluble salt minerals are the rare earth (RE) semisoluble minerals including bastnaesite ((Ce, La) FCO_3), monazite ((Ce, La,Y, Th) PO_4), xenotime and pyrochlore. The alkaline earth and RE semisoluble salt minerals have many similarities but differ with respect to the cation size and charge.

In this chapter literature on the surface chemistry of semisoluble salt minerals including both alkaline earth and rare earth semisoluble salts is first reviewed followed by specific attention to the surface chemistry of fluorite and then bastnaesite. The discussion includes electrokinetic behavior, wetting characteristics, and collector adsorption.

1.1 Semisoluble Salts Minerals

Semisoluble salt minerals are characterized by their ionic bonding and are distinguished from soluble salt minerals by their limited solubility in water. One group of

semisoluble salt minerals is the alkaline earth minerals and another group of semisoluble salt minerals is the rare earth (RE) semisoluble minerals.

1.1.1 Electrokinetic Features

The characteristics of the mineral/water interface including surface charge for some systems can have a significant effect on flotation behavior. In any case, the electrokinetic feature helps to describe interfacial phenomena of a particular mineral system. In general the surface charge of all semisoluble salt minerals will be dependent on the pH of the system and will be sensitive to solution composition due to hydrolytic and/or metathetic exchange reactions at the mineral surface. The interfacial chemistry of these minerals and the interaction between minerals and solution will determine the surface charge developed. For alkaline earth semisoluble salt minerals, including calcium bearing semisoluble salts, such as fluorite(CaF_2), there are some differences in the reported electrokinetic phenomena, wetting characteristics, and collector adsorption density (Fa et al., 2003).

The flotation response and interactions of these semisoluble salt mineral particles depend on the surface composition, structure, and charge as well as solution chemistry. It has been reported that distinct floatability of alkaline earth semisoluble salt minerals including calcite, fluorite, and apatite was reduced due to interactions between these semisoluble salt minerals taking place in their suspended solution (Fa et al., 2003; Fa et al., 2006). The surface properties of one mineral are altered by the dissolved species in the solution from other minerals. As a result, the corresponding flotability difference is diminished (Fa et al., 2003; Fa et al., 2006).

The PZC and surface charge are determined by acid-base characteristics of the

surface, as frequently dictated by the oxyanions at the mineral surface. Consequently, the surface charge of the semisoluble salt minerals is dependent on pH and the hydrogen ion can be considered to be a potential determining ion (PDI). The PZC is the pH at which the zeta potential is zero.

In addition to the intrinsic surface components, the surface properties of mineral surfaces can be altered due to reaction with dissolved species in solution. The ability of an ion at the mineral surface to preferentially dissolve over its counter ion may account for surface charging and such lattice ions are also classified as potential determining ions (PDIs). In this way carbonate and calcium are identified as the PDI for calcite (Heberling et al., 2011). This in turn results in either a net positive or negative surface charge at the mineral surface. The nature of surface charge generation includes lattice substitution, preferential hydration of surface lattice ions, as well as surface acid group dissociation (Miller et al., 2004). For ionic solids such as the semisoluble salt minerals, preferential hydration of surface lattice ions is of particular interest. As mentioned, it is well known that solution chemistry is a critical factor in the development of flotation technology for these minerals. Thus, electrokinetic characteristics are useful for both interfacial characteristics and understanding flotation phenomena but also for improving the flotation separation and recovery of semisoluble salt minerals.

The electrokinetic features of alkaline earth and rare earth (RE) semisoluble salt minerals as reported in the literature are summarized in Table 1.1 and Table 1.2. The controversies in the reported data for the point of zero charge might be due to different source of minerals and consequently different composition. The experimental conditions under which the measurements were made may also be different.

Table 1.1 - Summary of points of zero charge (PZC) for selected alkaline earth semisoluble salt minerals.

Mineral	Formula	PZC (pH)	Technique	Reference
Fluorite	CaF_2	10.2	Sedimentation	(Miller and Hiskey ,1972)
		7.0	Electrophoresis	(Choi, 1963)
		10.6	Electrophoresis	(Fuerstenau et.al, 1967)
		8.5		(Miller and Hiskey, 1972)
	Synthetic CaF_2	9.5		(Rao, 1968)
				(Rao, 1968)
	Natural CaF_2	6.2-8.8		
Fluorite		10.2 (IEP)		(Orthgiess and Dobiáš, 1994)
		9.5 (IEP)	Electrophoresis	(Marinakis and Shergold, 1985)
		10.5	Micorelectrophoresis	(Pugh and Stenius, 1985)
		9.8	Electrophoresis	(Miller et al., 2004)
	CaF_2(111) flat surface-nonequlibrium	Negative for all pH values	Streaming potential	(Miller et al., 2004)
Apatite	$Ca_5(PO_4)_3(F,Cl,OH)$	4	Electrophoresis	(Rao et al., 1990)
		3	Microelectrophoresis	(Pugh and Stenius, 1985)
		7.4	Electrophoresis	(Amankonah and Somasundaran, 1985)
Calcite	$CaCO_3$	10.5 (IEP)		(Orthgiess and Dobiáš, 1994; Amankonah and Somasundaran, 1985)
		10		(Fuerstenau and Pradip, 1984)
		9.5	Microelectrophoresis	(Pugh and Stenius, 1985)
		8	Electrophoresis	(Martínez-Luévanos et al., 1999)
Barite	$BaSO_4$	7.0 (IEP)		(Orthgiess and Dobiáš, 1994)
		10		(Fuerstenau and Pradip, 1984)
		4.5	Electrophoresis	(Rao et al., 1990; Marinakis and Shergold, 1985)
		5.8	Electrophoresis	(Smith and Shonnard, 1986)
Celestite	$SrSO_4$	2.6	Sedimentation	(Ozkan and Yekeler, 2004)
		3	Streaming potential	(González-Caballero et al., 1989)
		3	Electrophoresis	(Martínez-Luévanos et al., 1999)
		5.8		(López-Valdivieso et al., 2000)

Table 1.2 - Summary of points of zero (PZC) charge for selected rare earth semisoluble salt minerals.

Mineral	Source	PZC (pH)	Technique	Reference
Bastnaesite (Ce, La) FCO_3	Mountain Pass (hand-picked)	9.5		(Pradip, 1981)
	Mountain Pass	5.3		(Houot et al., 1991)
	Mountain Pass	6.8		(Houot et al., 1991)
	Mountain Pass	7.2		(Houot et al., 1991)
	Bayan Obo	7.0		(Xiangyong, 1984)
		7.8		(Ren et al., 2000)
		8.0	Microelectrophoresis	(Ren et al., 1997)
Monazite	$CePO_4$	5.5		(Viswanathan, 1970)
		5.5		(Abeidu, 1972)
		3.4	Microelectrophoresis	(Houot, 1991)
		5.0		(Luo et al., 1984)
		5.3		(Cheng et al., 1993)
		5.2	Electrophoresis	(Pavez et al., 1996)
		4.7		(Ren et al., 2000)
		7.0		(Cheng, 2000)
Xenotime	YPO_4	3.0	Malvern Zetasizer IIc	(Cheng et al., 1993)
		7.0		(Cheng, 2000)
		2.3	Microelectrophoresis	(Pereira and Peres, 1997)
		3.0		(Pereira and Peres, 1997)
		4.0		(Pereira and Peres, 1997)
		5.0		(Pereira and Peres, 1997)

The electrokinetic characteristics of the rare earth phosphates reported in literature are reported in Table 1.2. The PZCs of monazite and xenotime are both on the acidic side, pH 5 and pH 3 respectively. For bastnaesite, a fluorocarbonate rare earth mineral, the PZC is higher, about pH 8. The reason for this difference is attributed to the anion properties. The dissociation constant for carbonic and phosphoric acids are presented in Table 1.3. The pK_a values for both the first (pK_{a1}) and second (pK_{a2}) acid dissociation constants of carbonic acid are larger than phosphoric acid. In other words, the carbonate lattice ion CO_3^{2-} is likely to adsorb hydrogen ions in the solution to a greater degree than the phosphate lattice ion PO_4^{3-}. Thus, the electrokinetic state of the bastnaesite surface is more alkaline, the PZC is pH 8, while the phosphate rare earth minerals have more acidic PZC values.

In addition to the surface acid properties of these oxyanion salts which generally accounts for the pH dependence of their zeta potential and reported PZC values, metathetic reactions at the surface of the semisoluble salts also occur and influence the surface charge. Surface carbonation of fluorite by CO_2 from the atmosphere was established (Miller and Hiskey ,1972). Subsequently, other surface carbonation reactions have been established. For example, the surface carbonation reaction was found to occur at celestite surfaces. In the presence of carbonate species in solution, the surface of celestite was converted to strontium carbonate at pH 7.8 as confirmed by the broad band at 1500 cm^{-1} in the IR spectra. The flotation of celestite occurs with the anionic collector sodium dodecyl sulfate but depression was found above pH 10 due to specific adsorption of HCO_3^- and CO_3^{2-} species under these conditions which inhibit collector adsorption (López-Valdivieso et al., 2000).

Table 1.3- Acid dissociation constants for carbonic and phosphoric acids.

Acid	**First pK_{a1} , 25^{o}C**	**Second pK_{a2} , 25^{o}C**	**Reference**
Carbonic, H_2CO_3	6.367	10.329	(Greenwood ,1997)
Phosphoric, H_3PO_4	2.12	7.21	(Brown, 2008)

Evidence of transformation of barite to barium carbonate in barite suspensions containing added carbonate has also been reported by Fuerstenau (Fuerstenau et al. ,1992). With added carbonates, the pH of both barite and barium carbonate suspension increases with increasing levels of added carbonate. At 8×10^{-4} M added carbonate, the same pH was measured for barite and barium carbonates suspensions, indicating that barite behaves like barium carbonate. Electrokinetic behavior of barite reveals that the zeta potential of barite resembles that of barium carbonate in aqueous carbonate solutions with a concentration higher than 8×10^{-4} M, confirming the transformation of barite to barium carbonate under these conditions.

Somasundaran et al. found that such metathetic exchange reactions take place in the apatite-calcite system. Interchange of the PZC between apatite and calcite occured when the particles were conditioned in the supernatants of the other salt. The apatite surface became more positively charged in calcite supernatant and the PZC shifted towards the calcite PZC. The zeta potential of calcite was reduced drastically in the presence of apatite supernatant and the PZC shifted towards that of apatite. When apatite and calcite were present in a mixed supernatant with 1:1 ratio, identical electrokinetic characteristics were observed. All of the above results indicate that through surface reaction and bulk precipitation, an apatite surface can be converted to a calcite surface and visa versa (Amankonah and Somasundaran ,1985).

Finally, fluoridation is another interesting example in which collophanite reacts with fluoride ion in solution. Complete flotation of collophanite can be achieved even at low fluoride concentrations given sufficient conditioning time due to the fluoridation reaction. Fluorite may form at the surface of collophanite and results in an improved flotation

response. At elevated temperature, a sharp increase in flotation recovery was observed in the presence of NaF (10^{-2} M), while in the absence of NaF, increasing temperature did not have any effect on flotation recovery (Miller et al. ,1987).

1.1.2 Wetting Characteristics

Interfacial chemistry of the solid-liquid interface plays a key role in many areas of technology. In particular, the structure of interfacial water molecules at solid surfaces is of great interest in a wide range of fields, including lubrication, corrosion, catalysis, chemical separations, oil recovery, waste processing as well as a variety of other biological, chemical and physical processes (Becraft et al., 2004; Gupta, Nath et al., 2002; Hopkins, McFearin et al., 2005; Roy and Hore, 2012; Verreault et al., 2012). In flotation chemistry, which involves the attachment of hydrophobic particles to air bubbles and subsequent separation from an aqueous suspension, understanding of interfacial water structure at mineral water interfaces is a fundamental feature of mineral recovery by flotation.

Not many studies have been conducted on the wetting characteristics of semisoluble salt minerals including alkaline earth and rare earth minerals. Generally, fluorite and apatite, which have a lower polarity, exhibit some degree of hydrophobicity. Results from current research indicate that the rare earth semisoluble salt minerals are hydrophilic due to their high polarity. The wetting characteristics of apatite have been reported. Interestingly, Suzuki et al. measured the contact angle of water droplets on single crystals of strontium chloroapatite ($Sr_5Cl(PO_4)_3$) and barium chloroapatite ($Ba_5Cl(PO_4)_3$) as summarized in Table 1.4 (Suzuki et al., 2004). The results presented in Table 1.4 indicate that the chloroapatite single crystal surfaces possess a larger contact angle than the 111

Table 1.4 - Contact angles for water droplets at the surface of apatite crystals at 20 ^{o}C.

Mineral	**Surface**	**Contact angle (sessile drop measurment)**	**Reference**
$Ba_5Cl(PO_4)_3$	$10\bar{1}0$	52 ± 5^{o}	(Suzuki, Hirose, and Oishi, 2004)
	$10\bar{1}1$	33 ± 1^{o}	(Suzuki, Hirose, and Oishi, 2004)
$Sr_5Cl(PO_4)_3$	$10\bar{1}0$	74 ± 8^{o}	(Suzuki, Hirose, and Oishi, 2004)
	$10\bar{1}1$	53 ± 5^{o}	(Suzuki, Hirose, and Oishi, 2004)
Apatite ($Ca_5F(PO_4)_3$)	Fresh random surface	8^{o}	(Wang, 2004)

surface of fluorite (~20^{o}), while the calcium fluoroapatite surface seems to be hydrophilic. The reason might be due to different experimental procedure including crystal size, cleaning method, etc. Suzuki et al. was using a crystal 3 mm in length and less than 0.5 mm in width. The crystals were washed in ethanol using supersonic cleaner and well dried, followed by fixing the crystals on a glass plate using a small bit of clay. The water drop used for contact angle measurement was 0.2 μl. However, for the fluorite and calcium apatite contact angle experiments, much larger crystal sizes (fluorite size: 45 ×25 × 3mm) were used. Also, a different cleaning procedure was used. These differences may account for the different contact angle results. The wetting characteristics of RE semisoluble salt minerals are not described in the literature.

1.1.3 Collector Adsorption

Collectors frequently used for the flotation and separation of the semisoluble salt minerals include fatty acids, sulfonates, sulfoscuccinates, sulfates, and hydroxamates, together with modifying agents.

1.1.3.1 Alkaline Earth Semisoluble Salts

Extensive studies have been conducted on collector adsorption features at alkaline earth semisoluble salt minerals surfaces, including fluorite, apatite, calcite, etc. In general, pH has a significant effect on oleate adsorption (Free and Miller ,1996). Temperature also influences the adsorption density (Rao et al. ,1990; Rao and Forssberg ,1991; Kellar et al. ,1991). Fatty acids were mostly investigated and a chemisorption mechanism is frequently found based on fourier transform infrared spectroscopy (FTIR) studies (Lu et al. ,1998). In addition, the effect of modifiers as well as mixture of cationic and anionic

collectors was also investigated and improved recovery obtained (Helbig et al. ,1998).

Due to the preferential floatability of fluorite from apatite, calcite and other gangue minerals, sodium oleate is most widely used as a collector for fluorite flotation (de Leeuw et al. ,1998). At low equilibrium oleate concentrations ($< 1\times10^{-5}$ M), monolayer coverage of oleate at the fluorite surface is reached and the adsorption density of oleate at the fluorite surface is 2-4 times higher than at the surface of calcite and apatite (Lu et al. ,1998). Atomistic simulations confirmed the preferential adsorption of methanoic acid at a fluorite surface when compared to calcite (de Leeuw et al. ,1998). Combined applications of anionic and cationic collector mixtures for fluorite flotation have also been studied and enhanced recovery of fluorite obtained (Helbig et al. ,1998). Others (Orthgiess and Dobiáš ,1994) studied the effect of modifiers on the flotation of fluorite, calcite and barite. For example, complexing agents with both oxygen and nitrogen as donor atoms were studied using both cationic and anionic collectors. Some complexing agents were found to act as depressants in flotation with anionic collectors, whereas activation was observed during fluorite flotation with a cationic collector. Collectors used in plant operations for the flotation of alkaline earth semisoluble salt minerals are summarized in Table 1.5.

The nature of oleate collector adsorption at the surface of alkaline earth salt minerals, including fluorite, apatite, calcite, etc., has been studied extensively by many researchers. It has been found that solution pH has a significant effect on oleate adsorption (Free and Miller ,1996). Temperature also influences the adsorption density (Rao, et al. ,1990; Rao and Forssberg ,1991; Kellar et al. ,1991). FTIR vibrational spectroscopy has established that fatty acid collectors such as oleate chemisorb at the surface of alkaline earth

Table 1.5 - Collectors used in plant operations for the flotation of alkaline earth semisoluble salt minerals.

Salt mineral	Collector	Flotation strategy	Conditions	Reference
Fluorite (CaF_2)	Fatty acid: 0.25-1kg/ton;	Use quebracho (0.25-0.5 kg/ton) depress carbonates; Use Na_2CO_3 and NH_4CO_3 (0.5-3.5 kg/ton) to disperse clay slimes.	pH not mentioned	(Bentzen, 1986)
Apatite ($Ca_5F(PO_4)_3$	Fatty acid: 0.4-1kg/ton	Use NaOH or Ammonia to adjust pH; Use fuel oil (0.5-2.0 kg/ton) to fortify the hydrophobic surface layer.	pH 8-9	(Bentzen, 1986)
Barite ($BaSO_4$)	Sulfonate or sulfonate mixtures: 0.25-0.75 kg/ton	25 to 50 % solids	pH 8.5-9.2	(Bentzen, 1986)

semisoluble salt minerals. The adsorption density of oleate by fluorite, calcite and apatite is compared in Figure 1.1 (Lu et al. 1998). The difference in magnitude of the adsorption density has been attributed to the different surface site densities of calcium ions for the three minerals. Table 1.6 shows the surface site densities and oleate adsorption densities for fluorite, calcite and apatite (Lu et al., 1998). The chemisorbed monolayer has been demonstrated by FTIR analysis and thermochemical measurements, which shows that the chemisorption reaction is an endothermic reaction (Miller et al., 1989; Kellar et al., 1991). Lu and Miller (Lu and Miller, 2002) further studied the nature of the chemisorbed calcium carboxylates at fluorite surfaces. It was found that the calcium-to-carboxylate ratio was 2:1, indicating that a bridging coordination between two calcium ions and one carboxylate group occurs, as is illustrated in Figure 1.2 and as confirmed by FITR spectra. Fatty acid molecules can form well ordered self-assembled monolayers at fluorite surfaces as revealed from FTIR/IRS (internal reflection spectroscopy) studies (Jang and Miller, 1995). Also, it can been shown that, for both stearic acid and oleic acid, only the head group of these fatty acids in the first monolayer reacts with the calcium sites of fluorite (Jang and Miller, 1993).

Contact angle measurements with water and diazomethane found that transferred Langmuir-Blodgett (LB) monolayers of fatty acids at fluorite surface are stable due to the complete interaction of the fatty acid monolayer with the fluorite surface. By spontaneous adsorption and self-assembly from aqueous solution, closely packed well-ordered stearate monolayer can be formed at fluorite surfaces, which is similar to a transferred LB monolayer (Jang et al., 1995).

The relationship between contact angle and adsorption density has also been studied

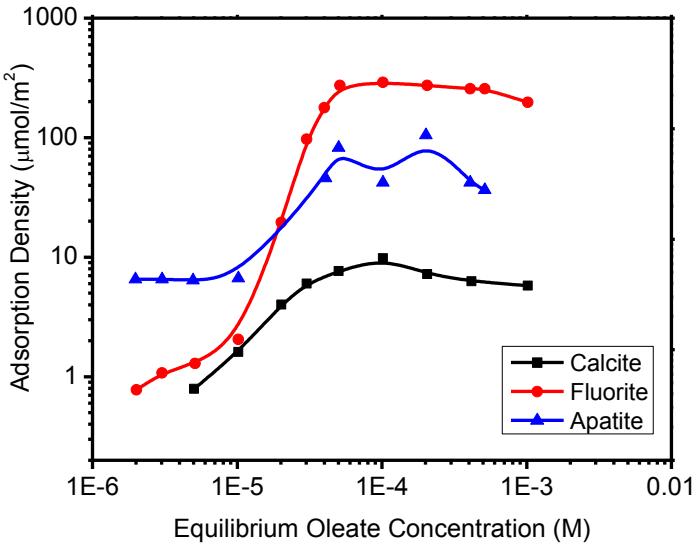

Figure 1.1 - Comparison of oleate adsorption isotherms at apatite, fluorite, and calcite surfaces at about pH 9.5 and a temperature of 20°C to 25°C (Data source: Lu et al., 1998).

Table 1.6 - Significance of calcium surface site density in oleate adsorption for selected semisoluble salt minerals (Data source: Lu et al., 1998).

Surface	Calcium surface site density, μ mol/m^2	Adsorption density from 1 $\times 10^{-5}$ M oleate solution, μmol/m^2
Fluorite (111)	12.9	6.5-6.7
Calcite ($11\bar{1}1$)	8.2	2.5-3.2
Apatite (0001)	6.6	1.5-2.0

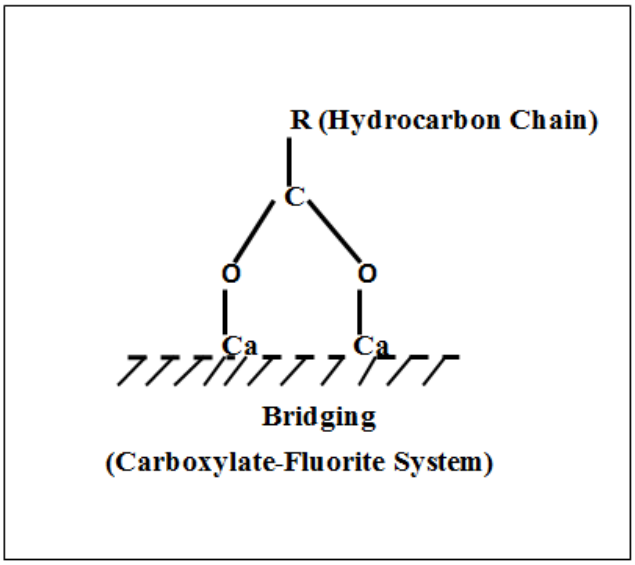

Figure 1.2 - The bridging coordination believed to define the nature of carboxylate chemisorption at the fluorite surface (Data source: Lu and Miller, 2002).

and compared by researchers for calcite and fluorite surfaces at high and low concentrations of oleate (Young and Miller, 1999). In-situ FTIR/IRS adsorption isotherms for fluorite and calcite show that oleate adsorbs at both surfaces and submonolayer monolayer coverage occurs approximately below 1×10^{-5} M oleate concentrations, above which multilayer adsorption begins. The finding that at low concentrations of oleate, adsorption density increases with increasing temperature implies an endothermic reaction and chemisorption for both minerals at this range (region I). The high oleate concentrations region (region II) exhibits calcium dioleate surface precipitation features indicated from infrared studies (Young and Miller, 1999).

At low concentrations of oleate as shown in Table 1.7, both contact angle and flotation recovery increase with increasing temperature and oxygen content in the case of fluorite surface. The hydrophobicity of calcite only increased with elevated temperature. These results confirmed the conclusion that at low concentrations of oleate, an endothermic chemisorption occurred at both surfaces. The effect of oxygen on fluorite might be attributed to the double-bond reactivity of chemisorbed oleate and the subsequent formation of a polymerized species at the surface as indicated from both ex-situ and in-situ infrared studies (Young and Miller, 1999). Besides, at similar oleate concentrations and flotation conditions, the contact angle values, adsorption density as well as flotation recovery are consistently higher than that of calcite. This appears to be due to the higher surface site density of fluorite than that of calcite, as indicated in Table 1.6. Consequently, more oleate molecules can be accommodated at the fluorite surface than at the calcite surface for the monolayer coverage region, resulting in a higher degree of hydrophobicity for fluorite. Furthermore, when the oleate adsorption density is similar,

Table 1.7 – Effect of temperature and oxygen on the hydrophobicity of fluorite and calcite surfaces at pH 9.2 in the chemisorption region (Region I) at 1×10^{-5} oleate (Data source: Young and Miller, 1999).

Mineral	Flotation conditions	Recovery	Contact angle	Equilibrium [Na Oleate]	Adsorption density
Fluorite	N_2&O_2 20°C	57%	70-74°	8.8×10^{-6} M	3.1 μmol/m^2
	O_2&O_2 20°C	71%	88-90°	8.8×10^{-6} M	3.1 μmol/m^2
	N_2&O_2 60°C	83%	88-91°	6.6×10^{-6} M	9.0 μmol/m^2
	O_2&O_2 60°C	100%	97-101°	6.6×10^{-6} M	9.0 μmol/m^2
Calcite	N_2&O_2 20°C	15-21%	NC	9.0×10^{-6} M	2.2 μmol/m^2
	O_2&O_2 20°C	18-22%	NC	9.0×10^{-6} M	2.2 μmol/m^2
	N_2&O_2 60°C	36-44%	53-57°	9.0×10^{-6} M	2.2 μmol/m^2
	O_2&O_2 60°C	38-44%	54-58°	8.8×10^{-6} M	2.7 μmol/m^2

70^{o} to 90^{o}, while no contact angle was observed for calcite under such conditions. The reason seems to be that only a submonolayer is obtained for calcite under these conditions, while oleate adsorption at fluorite surface results in full monolayer coverage. Consequently, fluorite exhibits a much larger hydrophobicity than calcite.

Although a lot of studies have been conducted on collector adsorption features of alkaline earth semisoluble salts minerals, particularly at low collector concentrations, including adsorption isotherm, identification of chemisorption region, and contact angle measurements for characterization of hydrophobic surface state, research on these fundamental aspects for collector adsorption for rare earth minerals has not been reported. Pradip (1981) studied the surface properties of bastnaesite, but only high concentrations of collector (hydroxamate) ($>1\times10^{-4}$ M hydroxamate) was investigated and no contact angle measurements were reported to describe the hydrophobic surface state. The relationship between contact angle and adsorption density below monolayer coverage of hydroxamate has not been established. All these aspects will be studied and discussed in Chapter 3 of this dissertation.

1.1.3.2 Rare Earth Semisoluble Salts

Bastnaesite ((Ce, La) FCO_3) and monazite ((Ce, La,Y, Th) PO_4) are two major rare-earth semisoluble minerals being produced in the United States, Australia, China, India and Brazil. Xenotime and pyrochlore are other rare earths minerals of less importance. The mineral bastnaesite consists mainly of the cerium subgroup or the lighter rare earths. Two major deposits of bastnaesite are Mountain Pass in the USA and Bayan Obo in China (Houot, 1991). The major gangue minerals for bastnaesite are barite, celestite, and calcite, all of which have similar surface properties. In industrial flotation of the

Mountain Pass ore, fatty acids are used as collectors together with soda ash and lignin sulfonate as depressants. Smith et al. (Gerdel and Smith, 1989) studied the effect of lignin sulfonate on the flotation of bastnaesite from barite and found that the lignin sulfonate has a stronger depressing effect for barite than for bastnaesite. Hydroxamic and phosphonic acids as well as fatty acids have been tested as collectors for Bayan Obo ore in China (Houot, 1991; Li et al., 1989). The problem with the use of fatty acid collectors is the low level of selectivity for such separations (Fuerstenau, 1988). Hydroxamates, such as the alkyl hydroxamate, potassium octyl hydroxamate, as well as modified hydroxamic acids (MOHA), are promising collectors, because the functional group's specificity for rare-earth cations is higher when compared to alkaline-earth cations. In this way the hydroxamates exhibit a better selectivity than fatty acids in the flotation of bastnaesite (Fuerstenau, 1988; Pradip and Fuerstenau, 1985; Ren et al., 1997). Besides collector, the depressant is also important in the flotation of rare-earth minerals (Houot, 1991). Specifically, Houot has reported that Na_6SiF_6 is a good depressant for calcite, barite and fluorite in the flotation of Mountain Pass ore. Collectors used in plant operations for the flotation of bastnaesite salt minerals are summarized in Table 1.8.

1.2 Fluorite

Fluorite as an alkaline earth semisoluble salt mineral is the most common fluoride mineral. It is used in the production of open-hearth steel in the preparation of synthetic cryolite for aluminum production (Janczuk et al., 1993; Wu and Forsling, 1995), and in the production of hydrofluoric acid. Fluorite is also widely used in other industrial applications, including fabrication of optical windows and mirrors, and apochromatic lenses (Fa et al., 2006; Michael et al., 2004; Reichling et al., 1996; Schick et al., 2004).

Table 1.8 - Type of collector used in plant practice for the flotation of bastnaesite minerals.

Rare earth mineral	Type of collector	Example	Condition	Reference
Bastnaesite ((Ce, La) CO_3F) or monazite ((Ce, La, Y, Th) PO_4)	Alkyl carboxylic acid	Fatty acid, Oleate Tall oil	pH 6-9	(Wang, 1996) (Jianzhong Cheng, 2007)
Bastnaesite ((Ce, La)CO_3F)	Alkyl phosphoric acid	Alkyl phosphate Easter P538	pH 4-5	(Chi et al., 1996) (Cheng et al., 2007)
Bastnaesite ((Ce, La)CO_3F)	Hydroxamic acid	Hydroxamate H205 L108 DH	pH 8-8.5	(Chi et al., 1996 Cheng et al., 2007)
Bastnaesite ((Ce, La)CO_3F)	Aromatic phosphonic acid	Styrene phosphonic acid	pH 6-10	(Chi et al., 1996) (Cheng et al., 2007)
Bastnaesite ((Ce, La)CO_3F	Aromatic carboxylic acid	O-phthalic acid	pH 5	(Chi et al., 1996) (Cheng et al., 2007)
Bastnaesite ((Ce, La)CO_3F)	Aromatic amide		pH 5-6	Chi et al., 1996 Cheng et al., 2007
Bastnaesite ((Ce, La) CO_3F) or monazite ((Ce, La, Y, Th) PO_4)	Combination reagent	Mixture of fatty acid and hydroxamate		(Chi et al., 1996) (Cheng et al., 2007)

The recovery of fluorite as a mineral resource is mostly achieved by flotation, a separation process which depends on control of the surface chemistry and the selective creation of a hydrophobic surface state. In this regard, the surface charge of the fluorite surface is of particular importance in understanding the fundamental features of the flotation separation process.

1.2.1 Electrokinetic Features

As discussed earlier, besides surface acid properties of the oxyanion salts which generally account for the pH dependence of their zeta potential and reported PZC values, metathetic reactions at the surface of the semisoluble salts also occur and influence the surface charge. A surface carbonation reaction was also found to occur at fluorite surfaces. Fluorite is positively charged in its saturated solution as has been clearly demonstrated experimentally and established theoretically from lattice ion hydration theory (Miller and Hiskey, 1972; Miller et al., 2004; Hu et al., 1997). Figure 1.3 shows that surface carbonation of fluorite begins at pH 8 as evidenced by the appearance of a doublet band centered at 1440 cm^{-1}. The surface carbonation reaction accounts for the change in electrokinetic behavior of fluorite and reversal of the zeta potential measured at about pH 10 under atmospheric conditions as shown in Figure 1.4.

Microeletrophoretic mobility measurements of fluorite particles reported in the literature have shown that fluorite particles exhibit a high positive zeta potential in the absence of surface carbonation (Rao et al., 1991; Miller and Hiskey, 1972), although few other researchers reported a negative surface charge of fluorite particles (Oberndorfer and Dobiáš, 1989). As shown in Figure 1.4, fluorite particles exhibit a high positive zeta potential in the absence of surface carbonation.

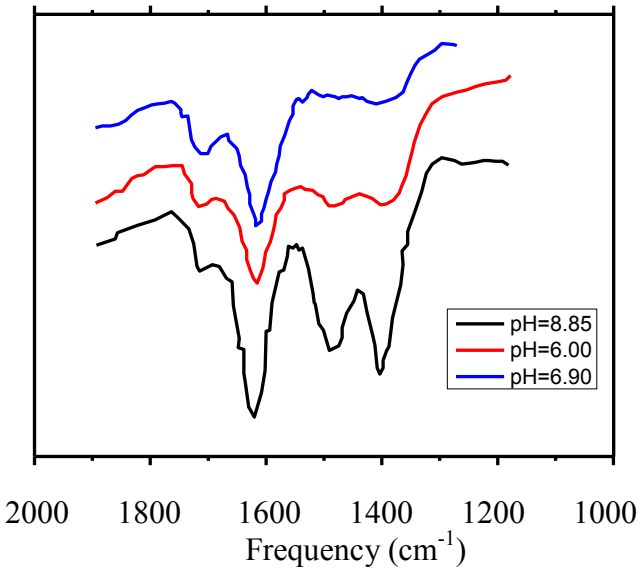

Figure 1.3 - Infrared spectra of fluorite at selected pH values in suspensions open to atmospheric conditions (Data source: Miller and Hiskey, 1972).

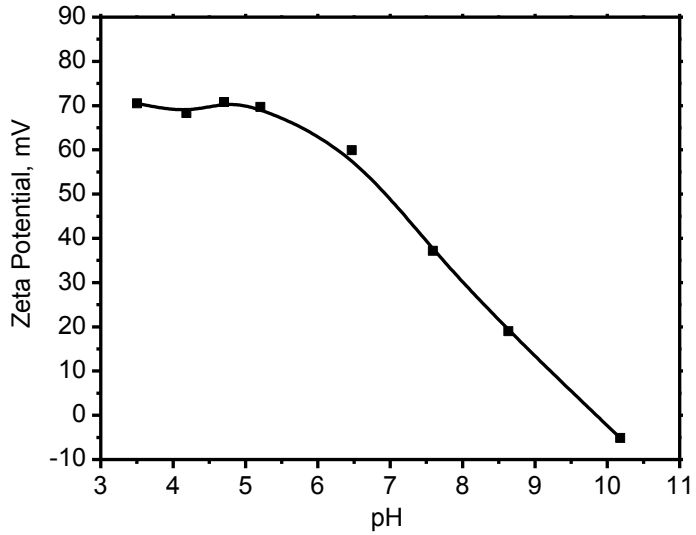

Figure 1.4 - Zeta potentials of 16 different fluorite particle samples as a function of solution pH (Data source: Miller et al., 2004).

De Bruyn and Agar (1962) first established the lattice ion hydration theory for the description of surface charge development for nonreactive ionic solids, which do not react with water to form weak surface acid groups (hydrolysis) or undergo surface oxidation reactions. According to this theory, surface hydration occurs through reaction between the mineral surface and the lattice ions. Consequently, differential hydration of the ions at the mineral surface determines the sign of the surface charge. However, for valence-asymmetric nonreactive ionic solids, such as CaF_2, lattice energy effects, crystal structure and preferential cleavage plane have to be considered together with gaseous ion hydration free energies (Miller et al., 2004; Fa, 2004). The sign of the surface charge can be predicted by comparing the relative magnitude of the hydration energies. Calara and Miller (1976) estimated the net free energy of fluorite lattice ions hydrating and joining the solution phase from a hard sphere electrostatic model. Calcium ions were calculated to have a net free energy of 1100 kcal/mol and fluoride ions were found to be 505 kcal/mol. Based on this, the positive sign of the zeta potential of fluorite was explained as the lower free energy fluoride ions would hydrate to a larger degree than the calcium ions. Fa (2004) also conducted flat plate streaming potential (FPSP) measurement at the 111 surface of fluorite and a negative zeta potential (~-15 mV) was calculated. Also, when cleaning fluorite only with DI water and when the solution is saturated with respect to CaF_2, positive zeta potential was also found from the flat plate streaming potential measurements, as is shown in Figure 1.5. In their measurement, they did not consider the effect of cleaning procedure on the surface charge of fluorite and only used DI water to clean the surface. In Chapter 2 of the present dissertation, the zeta potential of different fluorite crystal surfaces (111, 100) will be measured by flat plate streaming potential

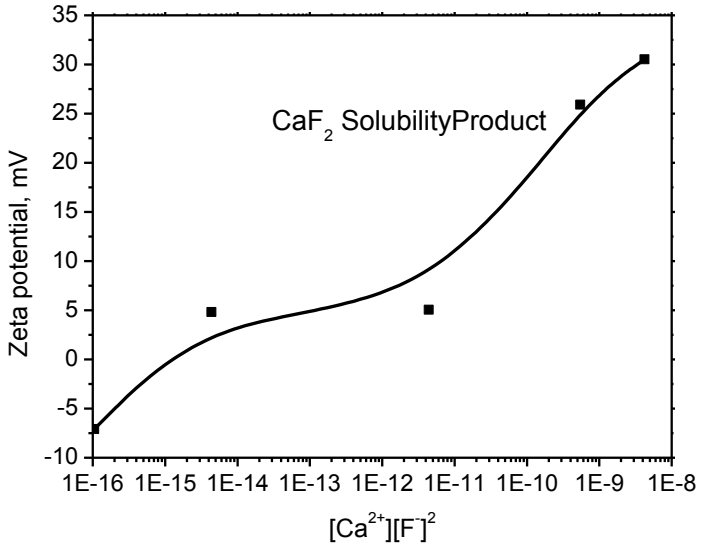

Figure 1.5 – Flat plate zeta potential at the (111) surface of fluorite as a function of concentration product of calcium and fluoride ions at pH 5.50 (Data source: Fa, 2004).

measurements and the effect of cleaning procedure on the surface charge of fluorite will be considered and discussed.

1.2.2 Wetting Characteristics

Interfacial chemistry of the solid-liquid interface plays a key role in many areas of technology. In particular, the structure of interfacial water molecules at solid surfaces is of great interest in a wide range of fields, including lubrication, corrosion, catalysis, chemical separations, oil recovery, waste processing as well as a variety of other biological, chemical and physical processes (Becraft et al., 2004; Gupta et al., 2002; Hopkins et al., 2005; Roy and Hore, 2012; Verreault et al., 2012). In flotation chemistry, which involves the attachment of hydrophobic particles to air bubbles and subsequent separation from an aqueous suspension, understanding of interfacial water structure at mineral water interfaces is a fundamental feature of mineral recovery by flotation.

As discussed by Drzymala (1994b), the wetting characteristics of minerals are explained by the energies of the three interfaces constituting the solid-water-air system. The surface free energies can be described by different bonding characteristics, including dispersion, polar, metallic, hydrogen and other bonding. Flotation is possible only when both thermodynamic and kinetic criteria are satisfied. In this way it is argued that the 100 surface of calcite is completely wetted by water, whereas the barite surface exhibits a definite contact angle of 17 ± 5^{o} and the fluorite surface is reported to have a contact angle of 30^{o} (sessile drop measurements).

Generally, fluorite has been considered to be a hydrophilic mineral, with a zero water contact angle. The fact that fluorite exhibits some natural hydrophobicity was first pointed out by Bakain in 1960. Following that, other researchers have considered the

native floatability of fluorite (Zawala et al., 2007). The results are summarized in Table 1.9.

Zawala et al. (2007) studied the dynamics of bubble attachment and formation of the three phase contact line for a freely ascending bubble contacting a fluorite surface. By investigating bubble collision phenomena they confirmed the formation of the three phase contact line (TPCL) at the fluorite surface with a contact angle of 40^{o}, indicative of its natural hydrophobicity.

Although a lot of studies have been conducted to investigate the wetting characteristics of fluorite, the experimental methods applied have been contact angle measurements or monobubble Hallimond cell flotation tests, giving limited information (Drzymala, 1994 a; Drzymala, 1994 b; Krasowska and Malysa, 2007; Zawala et al., 2007; Zawala et al., 2008). Depending on different experimental methods and sample preparation procedures, different values of the water contact angle for fluorite have been reported, ranging from 15^{o} to 55^{o}. When being treated with high temperature or HF solution, the contact angle is even higher (Zhang et al., 2012). In order to understand the wetting characteristics of fluorite at the molecular level, other experimental methods must be used. In addition, the effect of crystal surface structure on the wetting characteristics as well as on the surface charge of fluorite has not been studied.

1.3 Bastnaesite

As discussed earlier, bastnaesite ((Ce, La) FCO_3), a fluorocarbonate, is one of the principle rare earth semisoluble salt minerals and consists mainly of the cerium subgroup or the lighter rare earths. Most bastnaesite is cerium-bastnaesite, and cerium (Ce) is the most common rare earth element in bastnaesite minerals. Concentration of bastnaesite is

Table 1.9 - Summary of fluorite contact angle measurements reported in the literature.

Reference	Method		Contact Angle
Drzymala et al., 1994b.	Calculated from theory		104^{o}
Drzymala et al., 1994a.	Monobubble Hallimond cell		15^{o}
Zawala et al., 2007	Captive bubble		40^{o}
Szyszka and Stipien in (Zawala et al., 2007)	Sessile drop		55^{o}
Janczuk et al., 1993	Sessile drop, advancing contact angle		
	Dry fluorite at 50^{o}C for 30 min		82.2^{o}
	Dry fluorite at 110^{o}C for 2h		100.6^{o}
	Immerse fluorite in HF (0.1M) for 10 min	Dry fluorite at 50^{o}C for 30 min	0^{o}
		Dry fluorite at 110^{o}C for 2h	98.6^{o}
	Immerse fluorite in $Ca(OH)_2$ (0.1M) for 10 min	Dry fluorite at 50^{o}C for 30 min	53.1^{o}
		Dry fluorite at 110^{o}C for 2h	88^{o}

mainly achieved through flotation (Yörükoğlu et al., 2003; Pradip and Fuerstenau, 1991), which again involves the surface chemistry aspects of solid liquid interface. Thus, the electrokinetics behavior, wetting characteristics as well as collector adsorption features are important in the understanding of flotation fundamentals as well as the advancement and improvement in flotation technology and recovery.

1.3.1 Electrokinetic Measurements

As mentioned earlier, the interfacial features of the mineral/water interface greatly affect flotation separation and recovery. For rare-earth semisoluble salt minerals, the surface charge is also pH dependant and is influenced by lattice ions dissolution. Thus, the electrokinetic behavior of rare-earth minerals has a significant effect on the wetting characteristics as well as collector adsorption. Investigation of properties such as the zeta potential, contact angle and the interaction between interfacial water and crystal surfaces will definitely help us to have a better understanding of the surface chemistry of these minerals. In addition, examination of collector adsorption at REE mineral surface will undoubtedly be attractive for fundamental understanding of flotation response as well as the underlying mechanism. In this regard, it is expected that important contributions can be made to help improve flotation technology for the recovery of bastnaesite.

Electrokinetic behavior is of considerable importance in understanding the surface properties of rare-earth minerals. Being a semisoluble salt mineral, the lattice ions are expected to be the potential determining ions for both monazite and bastnaesite. For bastnaesite, only H^+, OH^+ and CO_3^{2-} were found to determine the surface potential, the F^- ion was not found to be a potential determining ion (Pradip, 1981; Houot, 1991). Similar to the results found for fluorite (Free and Miller, 1996), as was discussed earlier, the

flotation recovery of rare-earth minerals is dependent on solution pH. Consequently, the surface charge is an important property for consideration. The points of zero charge for rare-earth minerals as reported in the literature are summarized in Table 1.10. It can be seen that the PZC values in the literature have considerable variation. The reason for this may be due to the compositional differences of the minerals used in the electrokinetic measurements. For example, the rare earth content of a mineral sample depends on its origin. Also, as the zeta potential of the mineral is determined by lattice ions, crystal structure variations may also give rise to different surface charges values. Impurities in the minerals might be another possibility for the variances in PZC. Differences in preparation procedures can account for variation in the electrokinetic properties of the sample.

1.3.2 Wetting Characteristics

No references were found on the wetting characteristics of bastnaesite surfaces. Water contact angle measurements at a bastnaesite surface (Zagi Mountain, Pakistan) were made using both the sessile drop and captive bubble methods during research at the University of Utah. To understand the interaction of a water drop with the bastnaesite surface at the molecular level, molecular dynamics simulation (MDS) will be used in this dissertation research including the simulation of a water drop at a cerium-bastnaesite surface. The details will be discussed in Chapter 3.

1.3.3 Collector Adsorption

As mentioned earlier, the chelating hydroxamate collectors appear to be effective collectors for the flotation of bastnaesite. Hydroxamic acid forms metal complexes

Table 1.10 - Bastnaesite (Ce, La) FCO_3-summary of points of zero (PZC) charge.

Source of bastnaesite	PZC (pH)	Technique	Reference
Mountain Pass	9.5		(Pradip, 1981)
Mountain Pass	5.3		(Houot et al., 1991)
Mountain Pass	6.8		(Houot et al., 1991)
Mountain Pass	7.2		(Houot et al., 1991)
Mountain Pass	4.6		(Smith and Shonnard, 1986)
Bayan Obo	7.0		(Xiangyong, 1984)
	4.9		(Pavez et al., 1996)
	7.8		(Ren et al., 2000)
	8.0	Microelectrophoresis	(Ren et al., 1997)

through the hydroxyamide functional group. The stability constants (Table 1.11) for the complexes formed between hydroxamic acids and metal cations depend on the metal cation position in the periodic table. The complexes formed with alkaline earth metal cations, such as Ca^{2+}, Ba^{2+}, etc., have the weakest strength, while complexes formed with rare-earth elements are much stronger. See Table 1.11. Thus, hydroxamate collectors have a better selectivity for bastnaesite flotation from gangue minerals, such as calcite and barite (Pradip and Fuerstenau, 1983). The nature of hydroxamate adsorption by bastnaesite suggested involving a surface reaction (chemisorption) mechanism. It has been suggested that the cations (La^{3+}, Ce^{3+}) from the mineral surface form hydroxyl complexes in solution, reabsorb at the surface, then interact with the hydroxamate and form stable surface complexes with rare-earth minerals (Pradip and Fuerstenau, 1983). If the monolayer adsorption of hydroxamate collectors at bastnaesite surfaces is an endothermic chemisorption reaction, such as observed for oleate adsorption by fluorite (Lu et al., 1998), then the observation that an increase in temperature tends to increase the selectivity of bastnaesite flotation (Pradip and Fuerstenau, 1985) could be expected. The floatability of rare-earth minerals with hydroxamate collector is pH dependent and maximum floatability of bastnaesite can be obtained at about pH 9 (Fuerstenau and Pradip, 1984).

Defining salt ML_n where M represents the metal ion, and L the hydroxamate anion, the stability constants can be written as:

$$ML_{n-1} + L \rightleftharpoons ML_n$$

$$K_n = \frac{[ML_n]}{[ML_{n-1}][L]}$$

Table 1.11 - Stability constants for metal ethyl hydroxamates at, 20°C (Data source: Fuerstenau and Pradip, 1984).

Metal ion	$\log K_1$	$\log K_2$	$\log \beta_2$	$\log K_3$	$\log \beta_3$
H^+	9.35				
Ca^{2+}	2.4				
Fe^{2+}	4.8	3.7	8.5		
La^{3+}	5.16	4.17	9.33	2.55	11.88
Ce^{3+}	5.45	4.34	9.79	3	12.8
Sm^{3+}	5.96	4.77	10.73	3.68	14.41
Gd^{3+}	6.10	4.76	10.86	3.07	13.93
Dy^{3+}	6.52	5.39	11.91	4.04	15.95
Yb^{3+}	6.61	5.59	12.2	4.29	16.49
Al^{3+}	7.95	7.34	15.29	6.18	21.47
Fe^{3+}	11.42	0.68	21.1	7.23	28.33

and $M + nL \rightleftharpoons ML_n$

$$\beta_n = \frac{[ML_n]}{[M][L]^n} = K_L,\ K_2, \ldots \ldots K_n$$

The chelating reaction is accomplished through replacement of the hydrogen atom of the hydroxyamide group by a metal cation and ring closure by the carbonyl oxygen atom (Pradip and Fuerstenau, 1983):

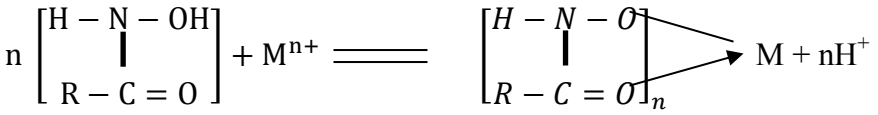

Pradip (1981) measured the equilibrium adsorption density of hydroxamte at bastnaesite, barite and calcite surfaces as a function of the equilibrium concentration of hydroxamate (Figure 1.6). Assuming the hydroxamate group to have a cross sectional area of 20.5 $Å^2$, the monolayer adsorption density would be 8.1×10^{-6} mol/m^2. However, when the concentration of hydroxamate is as low as 5×10^{-4} M, the adsorption density at the bastnaesite surface already exceeds one monolayer in coverage. The results show surface precipitation which suggests that the initial adsorption involves chemisorption. The limiting factor for hydroxamate adsorption below monolayer coverage needs to be considered and defined, then the monolayer adsorption concentration can be determined. Referring to the chelating reaction shown above, it might be possible for one cerium ion (Ce^{3+}) to react with as many as three hydroxamate molecules in the chemisorption process. According to our calculation, the cerium surface site density is 4.74 μmol/m^2. Thus a vertical monolayer hydroxamate adsorption density of about 8.1 μmol/m^2

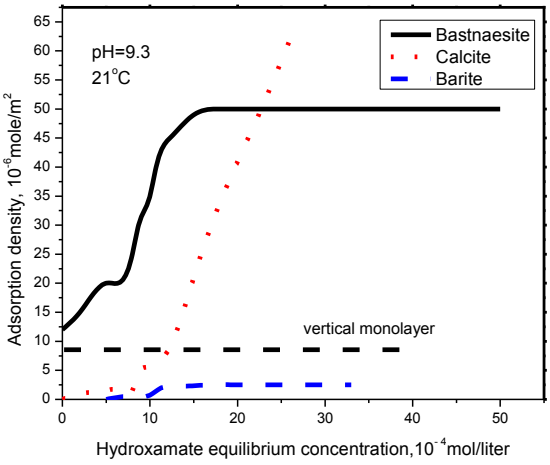

Figure 1.6 - Hydroxamate adsorption isotherms for barite, calcite and bastnaesite at 21°C and pH 9.3 ±0.1(Data source: Pradip, 1981).

corresponds to a ratio of hydroxamate to cerium of approximately 2 : 1. In other words, one cerium ion at the bastnaesite surface might be reacting with two hydroxamate molecules. This is different from the fluorite surface, which has a oleate adsorption density to calcium surface site density ratio of 1 : 2, as is mentioned earlier (Lu et al., 1998). The reason for this difference appears to be due to the difference in cation spacing at the bastnaesite and the fluorite surfaces and the partial charge of the cation. Certainly it is clear that the cerium-cerium spacing at bastnaesite surface is larger than the calcium-calcium spacing at fluorite surface. As the minerals used in the adsorption experiments were not single crystals, there may be some deviation in the actual adsorption density from the calculated value.

However, there might be another possibility that the adsorption of hydroxamate at bastnaesite surface is only limited by the cross area of hydroxamate. This means that hydroxamate might be reacting with surface cerium ions at different ratios with respect to cerium, from 1 : 1 to 3 : 1. The adsorption process is restricted by the free space available at the surface, which means that when the adsorption density reaches 8.1 μ mol/m^2, hydroxamate cross sectional area limitation, the surface is fully covered by a monolayer of hydroxamate and multilayer adsorption begins.

To have a better understanding of these fundamental aspects of adsorption at low concentrations of hydroxamate, adsorption density as well as the hydrophobic surface state must be studied. The adsorption density of hydroxamate at low concentrations will be measured and the corresponding hydrophobic surface state will be considered utilizing both contact angle measurement as well as MD simulations in Chapter 3 of this dissertation. The adsorption isotherm at low concentrations of hydroxamate as well as the

possible adsorption mechanism will also be considered and discussed in combination with reported data from the literature. The adsorption density for low concentrations of hydroxamate will be determined by high sensitivity TOC using solution depletion method and the adsorption isotherm will be determined. Monolayer coverage limiting factor will be defined and monolayer coverage region will be determined. The hydrophobic surface state of bastnaesite at different levels of hydroxamate adsorption below monolayer coverage will be studied using contact angle measurements as well as MD simulations and its relationship with adsorption density will be established. The behavior of interfacial water molecules at bastnaesite surface with hydroxamate adsorbed will be investigated by MD simulations. Conditions for what appears to be the formation of a well-ordered monolayer will be defined based on SFVS spectra. These results provide fundamental understanding and further insights with respect to bastnaesite flotation chemistry including, hydrophobic surface state, nature of the hydroxamate adsorption reaction, collector dosage for selective flotation, etc. The adsorption of hydroxamate on barite and calcite is significantly lower than on bastnaesite, suggesting much weaker interaction of hydroxamate with the surfaces of these two minerals.

Now, with MDS it will be possible to investigate the surface state in more detail, to describe not only collector organization, but also hydration phenomena and eventually, the level of hydrophobicity as defined by contact angle measurements.

1.4 Dissertation Research

1.4.1 Research Objectives

The overall objective of this dissertation is to examine the surface chemistry of semi- soluble salt minerals, including the interfacial wetting characteristics and surface

charge for different fluorite surfaces (111, 100 and 110 surfaces) as well as the rare earth mineral bastnaesite. Of special interest is examination of the effect of crystal surface structure on the wetting characteristics and surface charge at fluorite surfaces. It is expected that surface crystal structures might make a significant difference in wettability as well as the surface charge of the surfaces. In this way, it is intended that the relationship between crystal surface structure and the interfacial chemistry features be established using both molecular dynamics simulation (MDS) and sum frequency vibrational spectroscopy (SFVS) in addition to more traditional techniques. In addition to fluorite, the wetting characteristics of the rare earth mineral bastnaesite are also investigated using molecular dynamics simulation (MDS). Surface hydration state of bastnaesite surface is examined using both contact angle measurements and MD simulations. Finally, the interfacial chemistry of bastnaesite was considered with respect to the adsorption features of octyl hydroxamic acid.

1.4.2 Organization of Dissertation Research

The dissertation research is presented in two parts. Results and discussion of the surface chemistry of fluorite are reported in Chapter 2. Subsequently, the surface chemistry features of bastnaesite are reported in Chapter 3. The dissertation continues with Chapter 4, Summary and Conclusions.

In Chapter 2, three fluorite crystals, having different surfaces (111, 110 and 100) were used for contact angle measurements. These optical grade fluorite crystals with desired crystal surfaces were purchased from Red Optronics. Two hemi-cylindrical shaped fluorite crystals (111 and 100) purchased from Almaz Optics were used for sum frequency vibrational spectroscopy measurements. The surface planes for each of the

crystals were confirmed by X-ray diffraction analysis (XRD).

The interfacial chemistry features, including the surface charge and wettability are considered at three different fluorite surfaces (111, 100 and 110). In order to study the surface charge of different fluorite surfaces (111 and 100), the SurPASS electrokinetic analyzer was used for the determination of the zeta potential at two fluorite flat plate surfaces. The surface charge properties of different crystallographic surfaces of fluorite are discussed with respect of their surface crystal structure. The wetting characteristics of selected fluorite surfaces (111, 110 and 100 crystal surfaces) were examined under both nonequilibrium and equilibrium conditions including water contact angle measurements and interfacial water structure. Of special interest is the examination of the effect of crystal surface structure on the wetting characteristics of interfacial water molecules at fluorite surfaces. Detailed analysis of interfacial water structure was conducted under nonequilibrium conditions in order to understand the wetting characteristics of water molecules at the molecular level using molecular dynamics simulation (MDS) as well as sum frequency vibrational spectroscopy (SFVS). MD simulation of water drops at two fluorite surfaces (111 and 110) were carried out as well.

In Chapter 3, high purity bastnaesite samples from Zagi Mountain, Pakistan were used for contact angle measurement as well as collector adsorption experiments. Analytical techniques including X-ray fluorescence (XRF), electronic microscopy (EM), XRD and atomic force microscopy (AFM) are used to characterize their compositional and morphological properties.

The wetting characteristics of bastnaesite were examined using contact angle measurements and molecular dynamics simulations (MDS). The interfacial water

structure at bastnaesite surface is analyzed and compared in details with MD simulations. As mentioned earlier, the adsorption features as well as the corresponding hydrophobic surface state at low levels of hydroxamate adsorption has not been studied previously. Thus, collector (octyl hydroxamic acid from Cytec) adsorption at low concentrations at bastnaesite surface was studied utilizing contact angle measurements and solution depletion method. Sum frequency vibrational spectroscopy (SFVS) was used to identify conditions for what appears to be the formation of a well-ordered adsorbed state. MD simulations with low levels of hydroxamate coverage at the bastnaesite surface were conducted to investigate the hydrophobicity difference and confirmed experimental results.

CHAPTER 2

SURFACE CHEMISTRY OF FLUORITE

2.1 Wetting Characteristics of Fluorite

2.1.1 Introduction

As discussed in Chapter 1, fluorite is widely used in many industrial applications and the recovery of fluorite is achieved through flotation. The characteristics of the mineral/water interface including surface charge and water wettability are fundamental issues associated with flotation behavior. Thus, investigation on these two aspects of interfacial chemistry of fluorite will have particular significance for understanding the flotation chemistry of the system.

The objective of this section of the dissertation is to examine the wetting characteristics and surface charge of different crystal surfaces of fluorite (111, 100 and 110) using contact angle measurements, molecular dynamics simulations (MDS) and sum frequency vibrational spectroscopy (SFVS) as well as flat plate streaming potential analysis. Electrokinetics and wettability at these three fluorite surfaces are investigated and compared with respect to their surface structure difference. Different degrees of hydration of these fluorite surfaces are expected to be revealed through contact angle measurements. Detailed analysis of interfacial water structure at fluorite surfaces will be conducted utilizing MDS as well as SFVS.

2.1.2 Materials and Methods

2.1.2.1 Sample Preparation

Three flat plate fluorite crystals, having different surfaces (111, 110 and 100) were used for contact angle and streaming potential measurements. These flat plate optical grade fluorite crystals with desired crystal surfaces were purchased from Red Optronics. Two fluorite crystals with 111 and 100 surfaces of hemi-cylindrical shape were used for VSFS measurements. These hemi-cylindrical optical grade fluorite crystals with desired crystal surfaces were purchased from Almaz Optics. The surface planes for each of the crystals were confirmed by X-ray diffraction analysis.

The fluorite samples were cleaned by rinsing with acetone, methanol, and copious amount of deionized water, followed by drying with high-purity nitrogen. The samples were then treated with plasma and again dried with high-purity nitrogen gas. All other glassware were cleaned by rinsing with acetone, methanol, copious amounts of deionized water, and dried by high-purity nitrogen gas. Deionized water was obtained from a Milli-Q system. The resistivity of the water was above 18MΩ in all experiments.

2.1.2.2 Contact Angle Measurements

Contact angles were measured with a Rame-Hart goniometer using the captive bubble technique. The measurement of an intermediate contact angle was accomplished by the release of a bubble from the needle tip after formation with a syringe; the bubble was then caught beneath the fluorite surface, followed by attachment. The equilibrium contact angle was measured for all cases of attachment. In addition, advancing and receding contact angles were also measured. The advancing contact angle, which is the largest possible contact angle, was measured when decreasing the bubble volume while

attached to the surface and the receding contact angle, which is the smallest possible angle, was obtained when expanding the attached bubble to a larger volume. The difference between advancing and receding contact angles is defined as contact angle hysteresis; the reason for the difference between advancing and receding contact angles has been attributed to surface roughness and heterogeneity, metastable surface energy states, etc. (Lam et al., 2001; Lam et al., 2002; Drelich et al., 1996) .

2.1.2.3 Molecular Dynamics Simulation (MDS)

Molecular dynamics simulations (MDS) have been widely used for the exploration of structural and dynamic properties of atoms and molecules, in particular, the interfacial water molecules at solid surfaces. This computation method calculates the time dependent behavior of a molecular system. Molecular mechanical force fields are built to define forces between the atoms or molecules and potential energy. The trajectories of atoms and molecules can be determined by numerically solving Newton's equations of motion for a system of interacting atoms or molecules (Alder and Wainwright, 1959; Rahman, 1964). It has been widely used and can give us significant insights on the physical movements of atoms and molecules of interest and eventually lead us to a better understanding of interactions between molecules and surfaces as occurs in flotation systems.

A MD simulation program, DL_POLY_214 (Smith and Forester, 1996), is used for the analysis of fluorite surfaces. A simple cubic cell (water box) was used. It contained the extended simple point charge (SPC/E) (Berendsen et al., 1987b) water molecules and the fluorite crystal was constructed using lattice parameters provided by American Mineralogist Crystal Structure Database (Gruner, 1934; Perdikatsis and Burzlaff, 1981).

The system is defined with periodic boundary conditions. The number of atoms for the fluorite surfaces used for interfacial water analysis and for water drop contact angle determination are listed in Table 2.1 and 2.2, respectively. The interaction parameters for fluorite are taken from literature with calcium ion having a positive two charge and the fluoride ion having a negative one charge (Lee and Rasaiah, 1996). The intermolecular potential parameters are listed in Table 2.3.

The pair potential force field used in the simulations is given as a combination of the Lennard-Jones and the Coulomb electrostatic interactions, and can be expressed as:

$$U_{pair} = \sum_i \sum_j \left(4\varepsilon \left[\left(\frac{\sigma_{ij}}{r_{ij}} \right)^{12} - \left(\frac{\sigma_{ij}}{r_{ij}} \right)^{6} \right] + \frac{q_i q_i}{r_{ij}} \right) \quad (2\text{-}1)$$

Here ε is the energy parameter, σ is the size parameter, q is the charge, and r is the distance between species i and j. The potential parameters of pairs were calculated by applying the Lorentz-Berthelot mixing rules:

$$\varepsilon_{ij} = \sqrt{\varepsilon_i \varepsilon_j} \quad (2\text{-}2)$$

$$\sigma_{ij} = \frac{\sigma_i + \sigma_j}{2} \quad (2\text{-}3)$$

Initially, the fluorite crystal is simulated in a NPT assemble (moles (N), pressure (P) and temperature (T) are conserved) with the pressure fixed at 0.1 Mpa and the temperature at 300K for 100ps. After adding SPC-E water into the system, the simulation is performed in a NVT assemble (moles (N), volume (V) and temperature (T) are conserved) using Hoover's thermostat (Melchionna, Ciccotti, and Holian, 1993). The leap-frog method with a time step of 1fs is used to integrate the particle motion. The

Table 2.1 – Number of atoms in the fluorite surface for interfacial water analysis.

Surface	Species	Number of atoms
111	Calcium	288
	Fluorine	576
100	Calcium	432
	Fluorine	864
110	Calcium	384
	Fluorine	768

Table 2.2 – Number of atoms in the fluorite surface for water drop contact angle.

Surface	Species	Number of atoms
111	Calcium	2592
	Fluorine	5184
110	Calcium	3456
	Fluorine	6912

Table 2.3 – Potential parameters for fluorite/water interaction.

Species	Charge [e]	ε[Kcal/mol]	σ[Å]	Reference
Calcium	2	0.1	2.8721	(Lee and Rasaiah, 1996)
Fluorine	-1	0.18034	3.1201	(Lee and Rasaiah, 1996)
Water hydrogen	0.4238	0	0	(Berendsen et al., 1987a)
Water oxygen	-0.8476	0.1554	3.1659	(Berendsen et al., 1987a)

Ewald sum is used to account for the electrostatic interactions. A final simulation time of 1ns (nanosecond) ($1x10^6$ steps) after a 500ps (picosecond) equilibration period was performed. The water density profile was analyzed based on the equilibrium condition with 1ns simulation after the equilibration period. The residence time profile was a dynamic analysis of a 200ps simulation after the equilibration period.

2.1.2.4 Sum Frequency Vibrational Spectroscopy (SFVS)

Being first introduce by Shen's group in 1987 (Zhu et al., 1987), SFVS has been proven to be an effective technique for detection of molecules at surfaces and interfaces, including solid/liquid, liquid/liquid, solid/air and liquid/air interfaces (Bain, 1995; Liljeblad and Tyrode, 2012; Hopkins et al., 2005; Wolfrum et al., 1993; Wang et al., 2008). SFVS is a second-order nonlinear optical surface selective technique used to analyze surfaces and interfaces. The principle is that two incident laser beams, a tunable IR (infrared) beam and a visible beam with frequencies ω_{IR} and ω_{vis}, respectively, overlap at a surface of interest. An output beam is generated with a frequency ω_{SF}, which equals to the sum of the two input beams. This process is shown in Figure 2.1. As the infrared beam is tuned through the spectral region of interest and when the photon energy coincides with the energy of the molecular vibrational mode, the SF response is resonantly enhanced. The advantages of SFVS include nondestructive, highly sensitive with good spatial, temporal, and spectral resolution, and applicable to any interfaces accessible by light (Zhuang et al., 1999). Due to the second-order nature of the response, it is forbidden in systems possessing inversion symmetry. While at surfaces and interfaces where the centrosymmety are broken, the SF processes are allowed, which makes it advantageous with surface specificity and sensitivity (Van et al., 2004; Nickolov

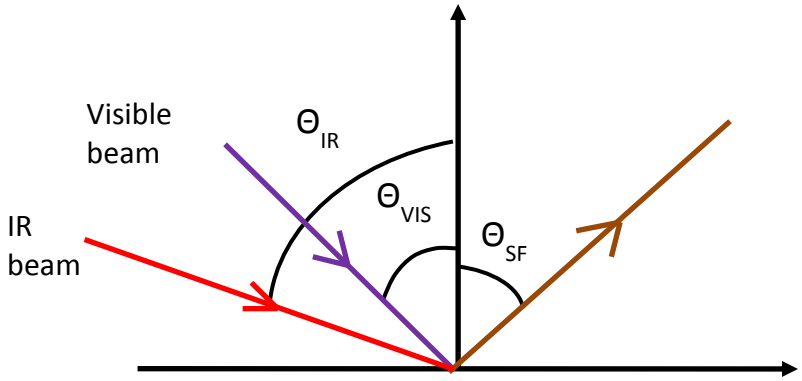

Figure 2.1 - Sum frequency generation at an interface.

Van Loon et al., 2007; Schrödle and Richmond, 2008; Richmond, 2002).

The SFG intensity is proportional to the square of the absolute value of the effective sum frequency susceptibility χ_{eff} as well as the intensities of the two incident laser beams. The effective sum frequency susceptibility contains all the measurable information on the response of the molecular system to the incident optical fields at the sum frequency (Wang et al., 2005; Zhuang et al., 1999):

$$I(\omega) = \frac{8\pi^3\omega^2 sec^2\beta}{c_0^3 n_1(\omega_1) n_1(\omega_2)} \left|\chi_{eff}^{(2)}\right|^2 I(\omega_1) I(\omega_2) \qquad (2\text{-}4)$$

The effective nonlinear susceptibility $\chi_{eff}^{(2)}$ has the following form:

$$\chi_{eff}^{(2)} = [\hat{e}(\omega) \cdot L(\omega)] \cdot \chi_{ijk}^{(2)} : [L(\omega_1) \cdot \hat{e}(\omega_1)][L(\omega_2) \cdot \hat{e}(\omega_2)] \qquad (2\text{-}5)$$

with ω, ω_1 and ω_2 are the frequencies of the SF signal, visible and IR laser beams, respectively; $n_m(\omega_i)$ is the refractive index of the bulk medium m (m=1,2,') at frequency

ω_i (i = 0, 1, 2); β_i is the incident or reflection angle from the interface normal to the beam with frequency ω_i; I (ω_i) is the intensity of the SFG signal or the input laser beams, respectively; $\hat{e}(\omega_i)$ is the unit electric field vector for the light beam at frequency ω_i at the interface; and $L(\omega_i)$ is the Fresnel factor at frequency ω_i.

If we define the xy plane in the laboratory coordinate system as the plane of interface with z axis as the surface normal, then p polarization denotes the optical field in the xz plane, s represents polarization perpendicular to the xz plane (Zhuang et al., 1999; Lu et al., 2005; Wang et al., 2005). The nonlinear susceptibility term $\chi_{ijk}^{(2)}$ has a maximum of 27 components. However, the number of unique contributing or nonzero components is less due to symmetry constraints. For an achiral rotationally isotropic interface with a $C_{\infty v}$ symmetry, there are seven nonzero terms, namely, $\chi_{xxz}^{(2)} = \chi_{yyz}^{(2)}$, $\chi_{xzx}^{(2)} = \chi_{yzy}^{(2)}$, $\chi_{zxx}^{(2)} = \chi_{zyy}^{(2)}$, $\chi_{zzz}^{(2)}$ (Zhuang et al., 1999; Lambert et al., 2005; Fischer and Buckingham, 1998; Lu et al., 2005).

Based on the above definition of the s and p polarizations, the p polarized light may be resolved into x and z components, but s polarized light only has a component in the y direction. Thus, we can selectively probe particular susceptibilities with specific incident polarization combinations (Lambert et al., 2005). The four most commonly used independent experimental polarization combinations in the SFG literature are ssp, sps, pss and ppp in the order of sum frequency (SF), visible and IR. In our experiments in the present study, we only employed ssp polarization combination for surface or interface detections. The equation for ssp polarization combination is shown below (Wang et al., 2005; Zhuang et al., 1999) in equation 2-6. From equation 2-6, it can be seen that the ssp polarization combination can only detect molecular vibrations modes with a component

in the z direction, that is, along the surface normal.

$$\chi^{(2)}_{eff,ssp} = L_{yy}(\omega)L_{yy}(\omega_1)L_{zz}(\omega_2)\sin\beta_2\,\chi_{yyz} \tag{2-6}$$

In the case where the interface is composed of molecules, the macroscopic sum frequency tensors $\chi^{(2)}_{ijk}$ are related to the microscopic hyperpolarizability tensor elements $\alpha^{(2)}_{ijk}$ through the ensemble average, denoted by $\langle\ \rangle$, over all possible molecular orientations (Zhuang et al., 1999; Miranda and Shen, 1999; Wang et al., 2005)

$$\chi^{(2)}_{ijk} = N_s \sum_{i'j'k'} \langle R_{ii'}R_{jj'}R_{kk'}\rangle\, \alpha^{(2)}_{i'j'k'} \tag{2-7}$$

where N_s is the number density of interface molecules, $R_{\lambda\lambda'}$ is an element of the rotational transformation matrix to transform molecular coordination to the laboratory coordination.

From equation 2-7 it can be seen that the SF intensity is proportional to the number density and related to the molecular orientations at the interface detected. In other words, the more molecules are detected at the interfaces, the higher intensity in the SF response. Similarly, the more ordered the interfacial molecules detected, the higher the SF in its intensity. As a result, from the SFVS spectra, the positions of the vibrational peaks as well as the relative intensities of the peaks at the same frequency, we can deduce numerical and orientationl information of interfacial molecules.

In IR-visible SFVS, if the IR frequency (ω_2) is near vibrational resonances to molecular vibrational transitions, $\alpha^{(2)}$ and $\chi^{(2)}$ can be written as (Wang et al., 2005; Zhuang et al., 1999; Miranda and Shen, 1999):

$$\alpha^{(2)}(\omega_{IR}) = \alpha_{NR}^{(2)} + \sum_q \frac{\alpha_q}{\omega_{IR}-\omega_q+i\Gamma_q} \quad (2\text{-}8)$$

$$\chi^{(2)} = \chi_{NR}^{(2)} + \sum_q \frac{\chi_q}{\omega_{IR}-\omega_q+i\Gamma_q} \quad (2\text{-}9)$$

where the subscript *NR* refers to nonresonant contribution, α_q, (χ_q), ω_q , and Γ_q denote the strength, resonant frequency, and damping constant of the qth vibrational mode, respectively.

With SFVS, a wealth of information on the molecular structure at the interface can be obtained from the characteristic frequencies, the position, and the shape of the vibrational modes, such as C-H, O-H, C=O, etc. (Schrödle and Richmond, 2008). Intensive SFVS studies have been done at solid liquid interfaces, among which insoluble oxide surfaces are mostly studied, such as silica, quartz, TiO_2 as well as sapphire (Al_2O_3) (Du et al., 1994a; Yeganeh et al., 1999; Kataoka et al., 2004; Ostroverkhov et al., 2004). However, only a few researchers have examined the interfacial water structure of semisoluble salt mineral surfaces, such as fluorite (CaF_2) (Becraft and Richmond, 2001; Becraft et al., 2003, 2004; Wang et al., 2008).

In our experiments, an EKSPLA, Ltd. sum-frequency generation spectrometer is used. The laser system has been described in a previous publication (Nickolov et al., 2004). The incident angles of the visible and IR beams at the water/fluorite interface were 60^o and 66^o, respectively. The sum-frequency signal is collected in reflection at 65^o. The visible and IR beams pulse energies were 500 and 160 μJ, respectively. Pulsed visible beam and tunable IR beam are overlapped spatially at the fluorite/water interface. The spectra are taken in SSP polarization (S: polarized sum-frequency, S: polarized visible, P:

polarized infrared) and were normalized to the visible and IR energies. Each data point is the average of 40 laser shots and the data were collected at 5cm^{-1} increment.

2.1.3 Results and Discussion for Nonequilibrium State

Nonequilibrium results on the wetting of fluorite surfaces are described in this section considering the surface interaction with water under conditions where chemical equilibrium has not been established. Surfaces are examined by contact angle measurements, MD simulations, and SFVS.

2.1.3.1 Contact Angle Measurements

The results of contact angle measurements for different crystal surfaces are shown in Table 2.4 for DI water at a natural pH=5.7. Since the solution is not saturated with respect to CaF_2, chemical equilibration has not been achieved and this case is designated as the nonequilibrium state.

From the contact angle results in Table 2.4 it can be seen that the contact angle of the 111 crystal surface is about 20^o in DI water, while the contact angles of the 100 and 110 surfaces is zero. These results indicate that attachment occurs only at the 111 crystal surface after bubble contact. In contrast, rupture and bubble attachment at the 100 crystal surface does not occur. In other words, the 111 surface of fluorite has some natural

Table 2.4 - Contact angle at different fluorite crystal surfaces in DI water pH=5.7 (captive bubble) for nonequilibrium state.

Crystal surface	Intermediate contact angle (θ, degrees)	Advancing contact angle (degrees)	Receding contact angle (degrees)
111	20^o	23^o	16^o
100	0^o	0^o	0^o
110	0^o	0^o	0^o

hydrophobicity, while the 100 and 110 surfaces are hydrophilic. The differences between the advancing and receding contact angles (contact angle hysteresis) for the 111, 110 and 100 surfaces are 7^o, 6^o and 6^o respectively. As mentioned earlier, this contact angle hysteresis might be due to surface roughness, heterogeneity or metastable surface energy state (Lam et al., 2001; Lam et al., 2002; Drelich et al., 1996).

For the 111 surface of fluorite, the cleaved surface is composed of fluoride ions, as is shown in Figure 2.2. These contact angle results are rather surprising since the fluoride ion hydration energy is substantial and on this basis, wetting of the surface would be expected. However, the same could be said about the talc basal plane surface in that even though the surface is covered with charged oxygen atoms, due to the lack of stable hydrogen bonding sites, the surface exhibits natural hydrophobicity. A possible reason for hydrophobicity of the 111 surface of fluorite is that the calcium-calcium lattice spacing distance on the 111 surface is not large enough to accommodate a full layer of water molecules and only a 50% partial coverage is favored on the 111 surface (de Leeuw and Cooper, 2003). The adsorption of water at the 111 surface was examined using both the density functional theory (DFT) calculations and atomistic simulation techniques and it was found that the main interaction between the fluorite surface and the interfacial water molecules is the binding of a water molecule's oxygen atom to a surface calcium atom. Thus for the 111 crystal surface, it may be the lack of surface calcium ions that accounts for the modest hydrophobic state ($\theta \approx 20^o$). It should be noted that similar

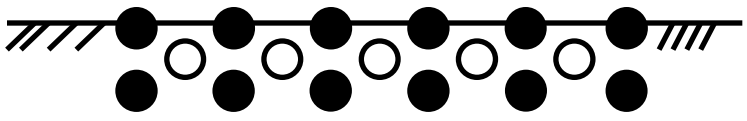

Figure 2.2 - The 111 crystal surface of fluorite (cross-section view, Black-F, White-Ca).

results showing 50% water coverage have also been reported (Fa et al., 2006).

In the case of the 100 surface, which ion dominates at the surface (calcium or fluoride) is dependent on the solution chemistry variables, such as the pH, ions in the solution, concentration of electrolyte, etc. For the 100 surface the calcium ions are expected to be at the surface. See Figure 2.3. The finding of a positive zeta potential of 30 mV (Table 2.7) at the 100 surface is evidence for the exposure of surface calcium ions. Given the contact angle results ($\theta \approx 0^o$), it is expected that these surface calcium ions undergo strong hydration and hence the 100 surface is well wetted by water. The lattice spacing of Ca-Ca is large enough to accommodate a full layer of water molecules and to make the 100 surface hydrophilic.

For the 110 surface, both calcium ions and fluoride ions are at the surface, as shown in Figure 2.4. The hydrophilic state of the 110 surface ($\theta \approx 0^o$) is due to the presence of surface calcium ions and the large interatomic Ca-Ca spacing which allows an easy accommodation of a full layer of water molecules, as suggested in the literature (de

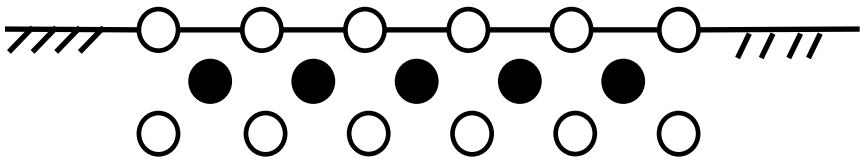

Figure 2.3 - The 100 crystal surface of fluorite (cross-section view, Black-F, White-Ca).

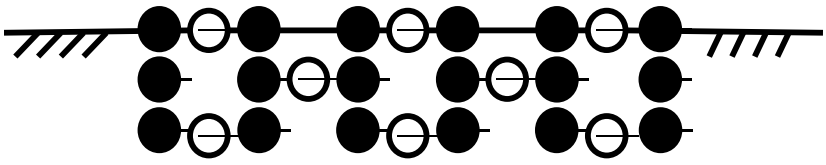

Figure 2.4 -The 110 crystal surface of fluorite (cross-section view, Black-F, White-Ca).

Leeuw and Cooper, 2003). It was also found that there are no significant H-F interactions and that the water molecules are adsorbed in an upright fashion on the 110 surface, in contrast to the 111 surface, where water molecules were found to adsorb in a flat orientation (the dipole moment of water is parallel to the surface).

The results from these contact angle measurements help to clarify the variation in water contact angles for fluorite as reported in the literature (Drzymala, 1994 a, b; Krasowska and Malysa, 2007; Zawala et al., 2007; Zawala et al., 2008; Zhang et al., 2012).

2.1.3.2 Molecular Dynamics Simulation (MDS)

In order to study the wetting characteristics of fluorite from the molecular level, MD simulations for a water drop of 488 water molecules at the 111 and 110 surfaces of fluorite were conducted and the advancing contact angles were found to be ~13^{o} for the 111 surface and 0^{o} for the 110 surface as shown by the results presented in Figure 2.5 and Figure 2.6. These results confirmed the water contact angle experimental results that the 111 surface has some degree of hydrophobicity; while the 110 surface is hydrophilic. See Table 2.4. When increasing the drop size from 488 water molecules to 821 water

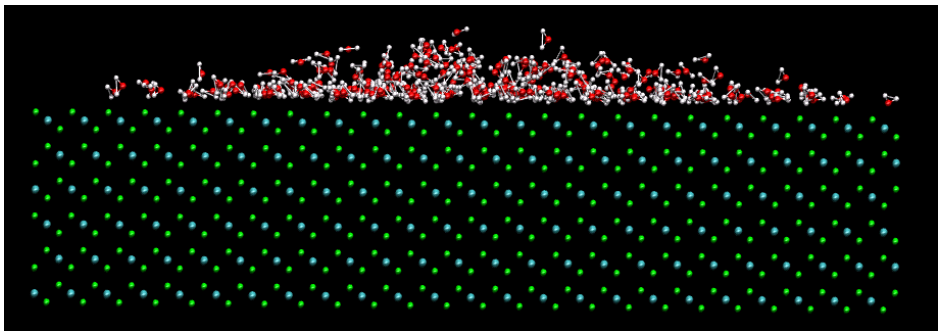

Figure 2.5 - MDS snapshot of water drop after spreading at the CaF_2 (111) surface (Green: fluorine; Cyan-calcium).

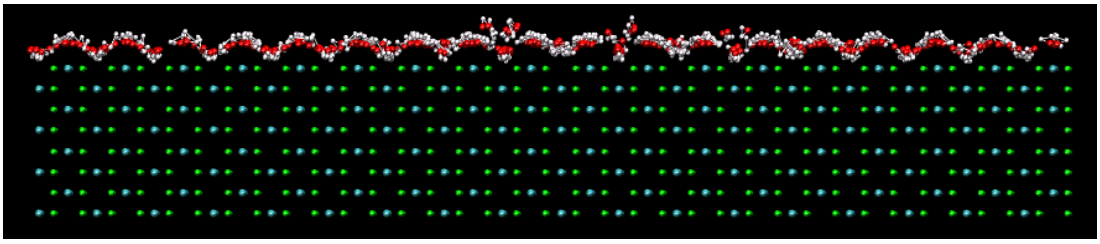

Figure 2.6 - MDS snapshot of water drop after spreading at the CaF_2 (110) surface (Green: fluorine; Cyan-calcium).

molecules, the MD simulation advancing contact angle result did not change.

In order to have a more detailed understanding of the interfacial water characteristics of the 111 and 100 surfaces of fluorite, the interfacial water density distributions along the surface normal were analyzed based on results from MDS. Figure 2.7 shows a snapshot of the equilibrium configuration of interfacial water molecules (Green-F, Cyan-Ca). It can be seen that for the 111 surface, there is a gap between the surface fluoride ions and the interfacial water molecules, which is indicative of the modest hydrophobicity for the 111 surface ($\theta \approx 20^o$). This is consistent with SFVS results to be discussed in the next section. For the 100 surface, there is no gap between the interfacial water and the surface. Instead, the 100 surface is strongly hydrated with water molecules packed closely to the surface. These results indicate that the 100 surface of fluorite is naturally hydrophilic, as was also determined from our contact angle measurements ($\theta \approx 0^o$) and SFVS spectra to be discussed in the next section. Wetting of the 100 surface is due to the strong hydration of calcium surface sites.

The water density distribution profiles for the 111 and 100 surfaces of fluorite are given in Figure 2.8, where it can be seen that the interaction of interfacial water molecules with the 100 surface of fluorite is much stronger than with the 111 surface of

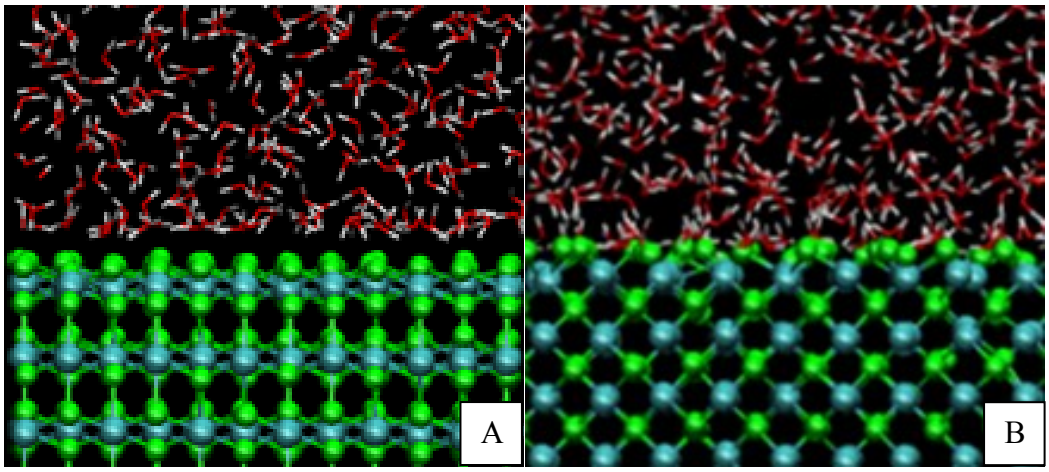

Figure 2.7 - Snapshot of the equilibrium configuration for CaF_2 (111) (A) and CaF_2 (100) (B) MDS (Green-F, Cyan-Ca).

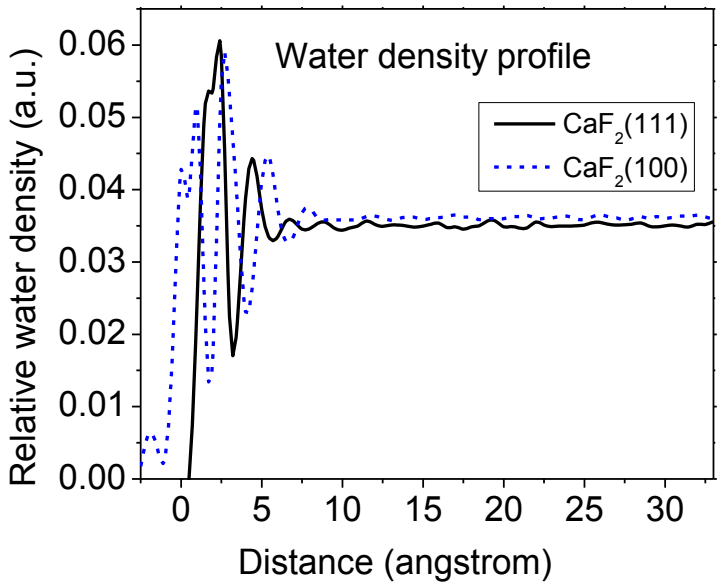

Figure 2.8 - Water density profile of the 111 and 100 surfaces of fluorite (zero distance denotes crystal surface).

fluorite. There appears to be three water layers interacting with the 100 surface of fluorite. While only two water layers are identified to be interacting with the 111 surface of fluorite; the reason for which was discussed previously. For the 111 surface of fluorite, fluoride ions are exposed on the surface with a sublayer calcium ions. As mentioned above, the main interaction between the fluorite surface and the interfacial water molecules is the binding of water molecule's oxygen atoms to surface calcium atoms (de Leeuw and Cooper, 2003). Calcium ions are divalent and have a much stronger interaction with divalent oxygen of interfacial water molecules than that of monovalent fluorides with monovalent hydrogen of interfacial water molecules. Thus, the presence of an outmost layer of fluorides ions of the 111 surface will weaken the interaction between fluorite surface and interfacial water molecules to some degree and impose moderate degree of hydrophobicity for the surface. On the other hand, for the 100 surface of fluorite, calcium ions are exposed on the surface, intense interaction between divalent calcium ions and divalent water oxygen ions exists and as a result, complete hydration occurs on the surface. This gives rise to higher interfacial water density, more interacting water layers and close packing of the primary water layer at the surface, as can be seen from Figure 2.7 (B) and the water density profile (Figure 2.8). A water exclusion zone is evident between the 111 surface and the primary interfacial water layer, which can be seen both from Figure 2.7(A) and the water density profile (Figure 2.8). In contrast, interfacial water molecules are closed packed at the 100 surface of fluorite as is evident from the MDS snapshot presented in Figure 2.7(B). Some water molecules have even been accommodated into the surface as is evident from the corresponding water density profile (Figure 2.8). All of these results confirm that the 100 surface of fluorite is

completely hydrophilic; the 111 surface of fluorite is less so and exhibits a moderate degree of hydrophobicity with a contact angle of 20^{o}.

To further understand the interfacial water structure at the 111 and 100 surfaces of fluorite, the residence times for interfacial water molecules were also analyzed. The residence time (τ) for interfacial water molecules describes the average time for a water molecule to reside in a particular water layer and is calculated as a function of distance along the fluorite surface normal. The residence time τ is defined by:

$$\tau = \int_0^{\infty} \langle R(t) \rangle dt \qquad (2\text{-}10)$$

and is obtained by numerical integration of R(t), where R(t) is the residence time distribution function:

$$R(t) = \frac{1}{N_h} \sum_{i=1}^{N_h} [\theta_i(0)\theta_i(t)] \qquad (2\text{-}11)$$

where $\theta_i(t)$ is the Heaviside unit step function. If a water molecule is in the hydration shell at time t, $\theta_i(t)$ equals 1. Otherwise, $\theta_i(t)$ equals 0. N_h is the hydration number (Berendsen et al., 1987b; Koneshan et al., 1998).

The residence time is a dynamic property of interfacial water molecules and it describes the tendency of the interfacial water molecules to stay at the fluorite surfaces. Thus, the longer the residence time, the stronger the interaction between the fluorite surface and the water molecules, and the more hydrophilic the fluorite surface is. Figure 2.9 shows the residence time profiles of the 111 surface and 100 surface of fluorite. It can be noted that the residence time of the interfacial water molecules at the 100 surface of fluorite is much larger than that at the 111 surface of fluorite. Some water molecules

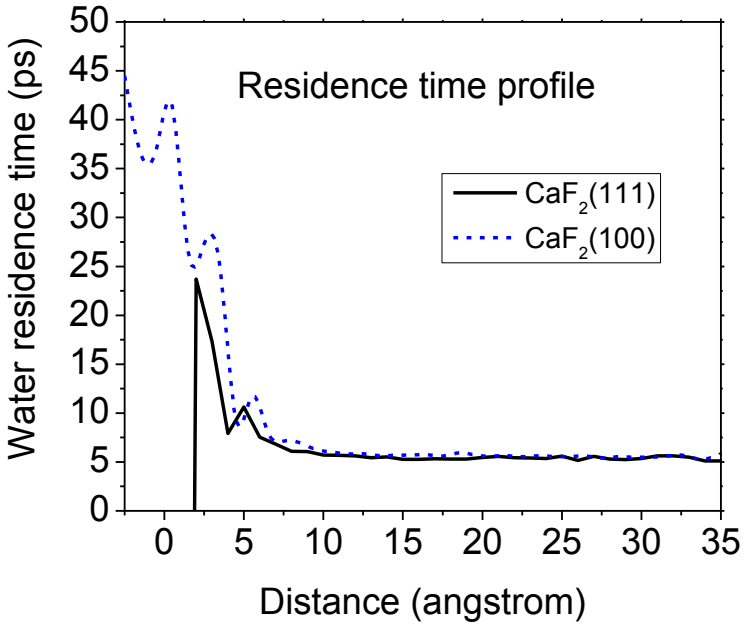

Figure 2.9 - Water residence time profile of the 111 and 100 surfaces of fluorite (zero distance denotes crystal surface).

at the 100 surface even stay at the surface as long as ~35-45 ps. However, for the 111 surface, the water residence time at the surface is zero since the primary interfacial water layer is 2 angstroms away from the surface. These results are consistent with the water density distribution profiles in Figure 2.8 and again demonstrate that the 100 surface is hydrophilic, while the 111 surface of fluorite has some modest degree of hydrophobicity.

In order to have a more detailed understanding of the interfacial water characteristics of different fluorite crystals, the interfacial water dipole orientation was analyzed. Two critical angles are used to describe the water orientation characteristic. As is shown in Figure 2.10, the angle α is defined as the angle between water dipole moment and surface normal. Angle β is the angle of the two hydrogen atoms position with respect to the surface normal. The surface atoms exposed at the surface play a key role in the

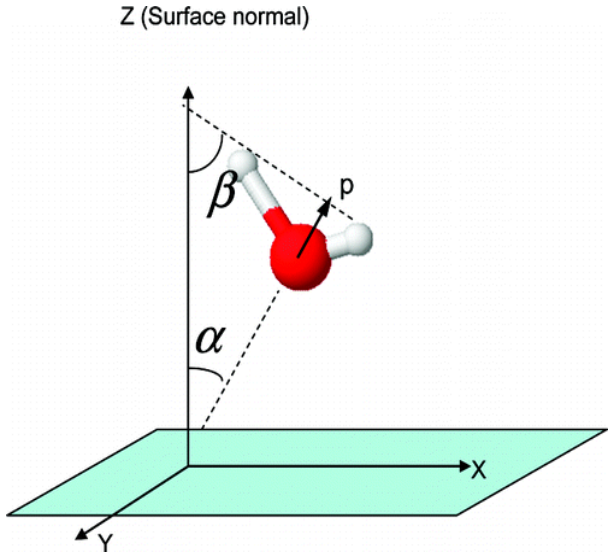

Figure 2.10 – Angles to describe water dipole orientation.

interaction between interfacial water molecules and mineral surfaces. Thus it is expected that the dipole moment as well as the hydrogen atoms position will be different for different crystallographic surfaces.

The interfacial water dipole orientation distribution contour and hydrogen atoms positions for the 111, 100 and 110 surfaces of fluorite are shown in Figure 2.11, Figure 2.12 and Figure 2.13, respectively. The results for Figure 2.11, 2.12 and 2.13 are also summarized in Table 2.5.

From Figure 2.11, it can be noticed that for the 111 surface of fluorite, the dipole moment orientation as well as the hydrogen atoms positions cover a wide range of angle distributions. The dipole moment orientation (angle α) of interfacial water molecules at the 111 surface of fluorite ranges from 15^{o} to 85^{o} and 130^{o} to 150^{o} with the highest dipole moment density occurring from 15^{o} to 30^{o} centering at 18^{o}. The hydrogen position orientation (angle β) ranges from 15^{o} to 90^{o}. The reason for the wide distribution might

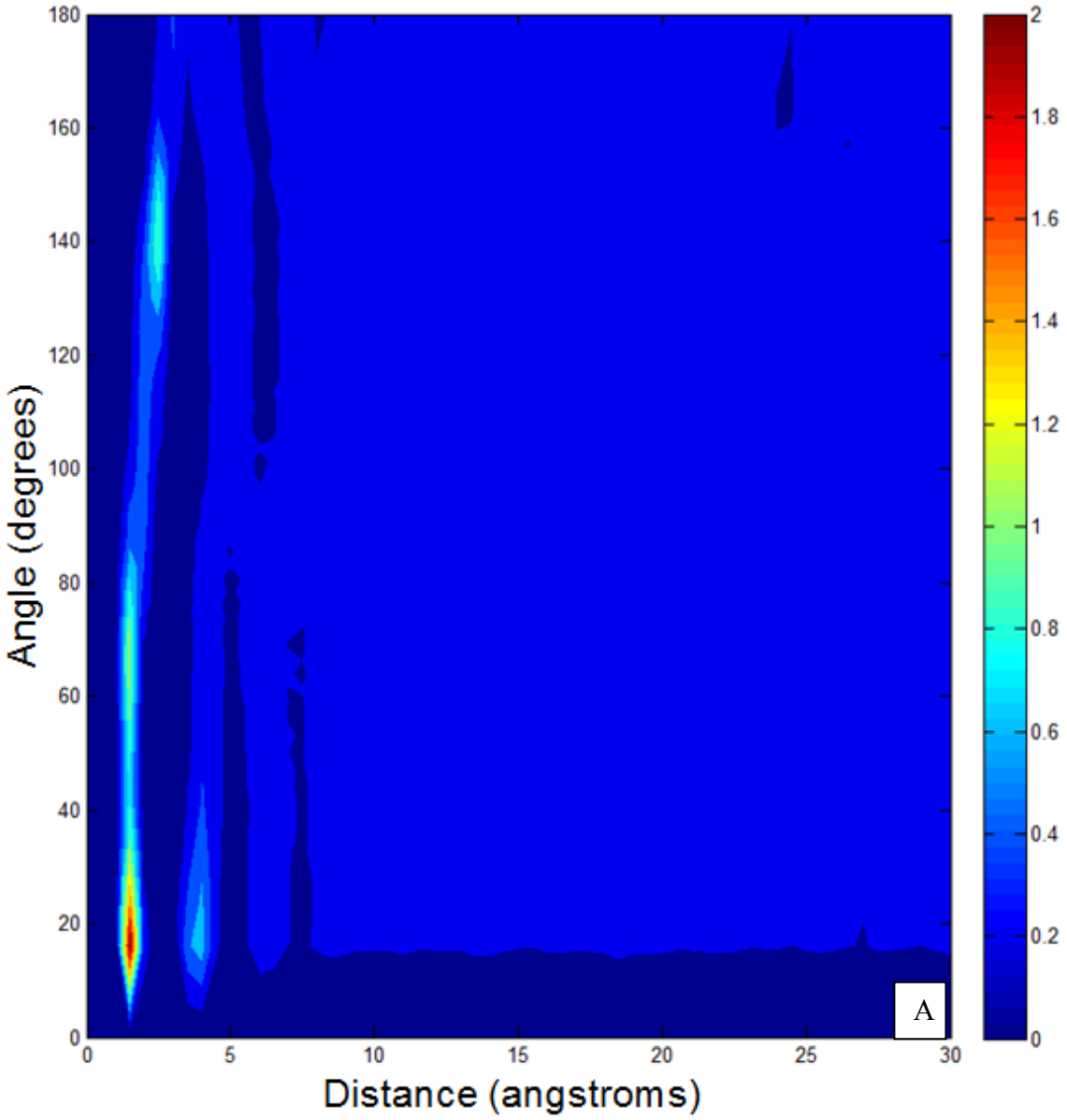

Figure 2.11 - Water dipole moment density distribution contour (A) and hydrogen atoms position density distribution (B) of CaF_2 (111).

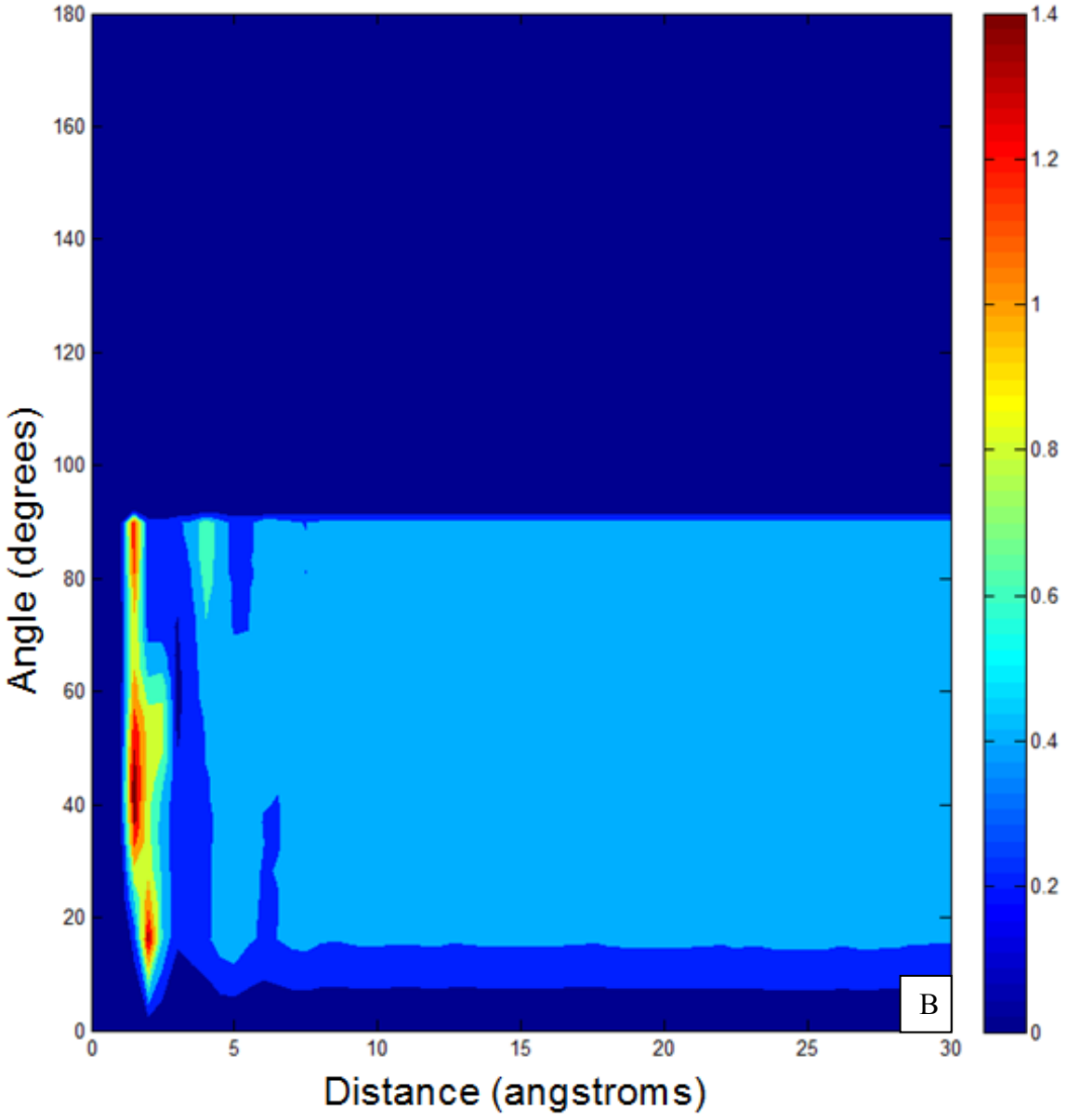

Figure 2.11 - Continued.

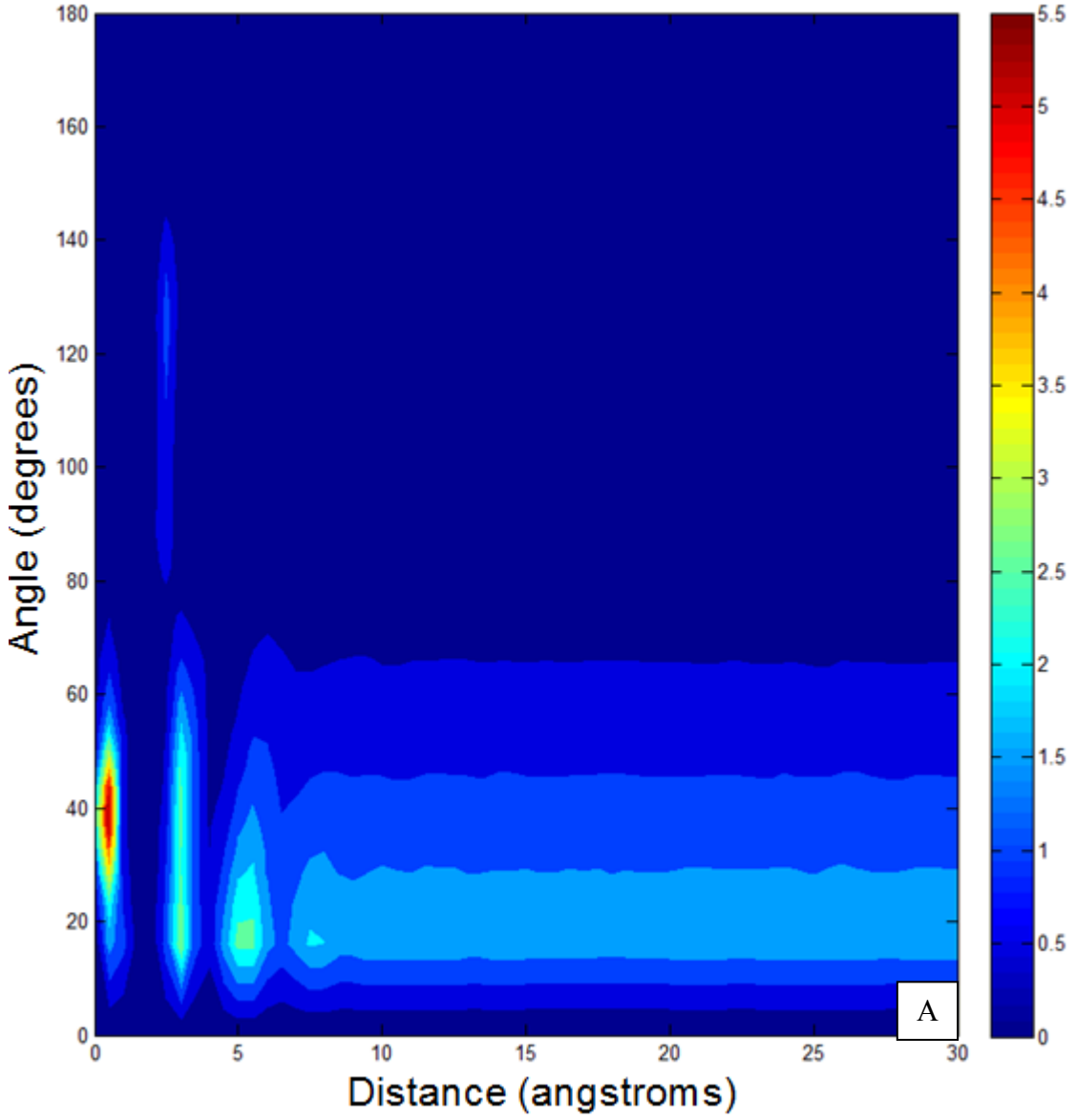

Figure 2.12 - Water dipole moment density distribution contour (A) and hydrogen atoms position density distribution (B) of CaF_2 (100).

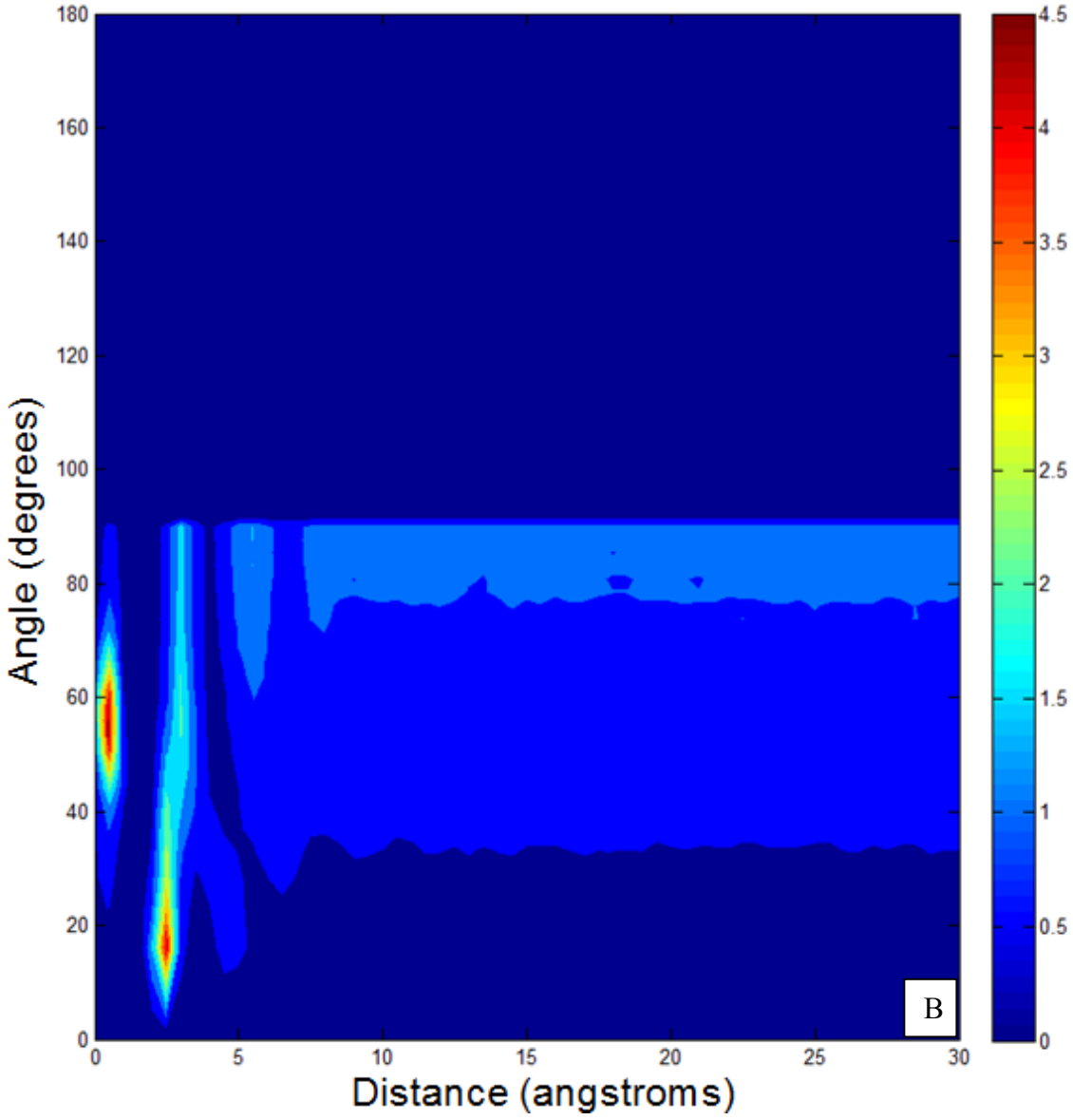

Figure 2.12 – Continued.

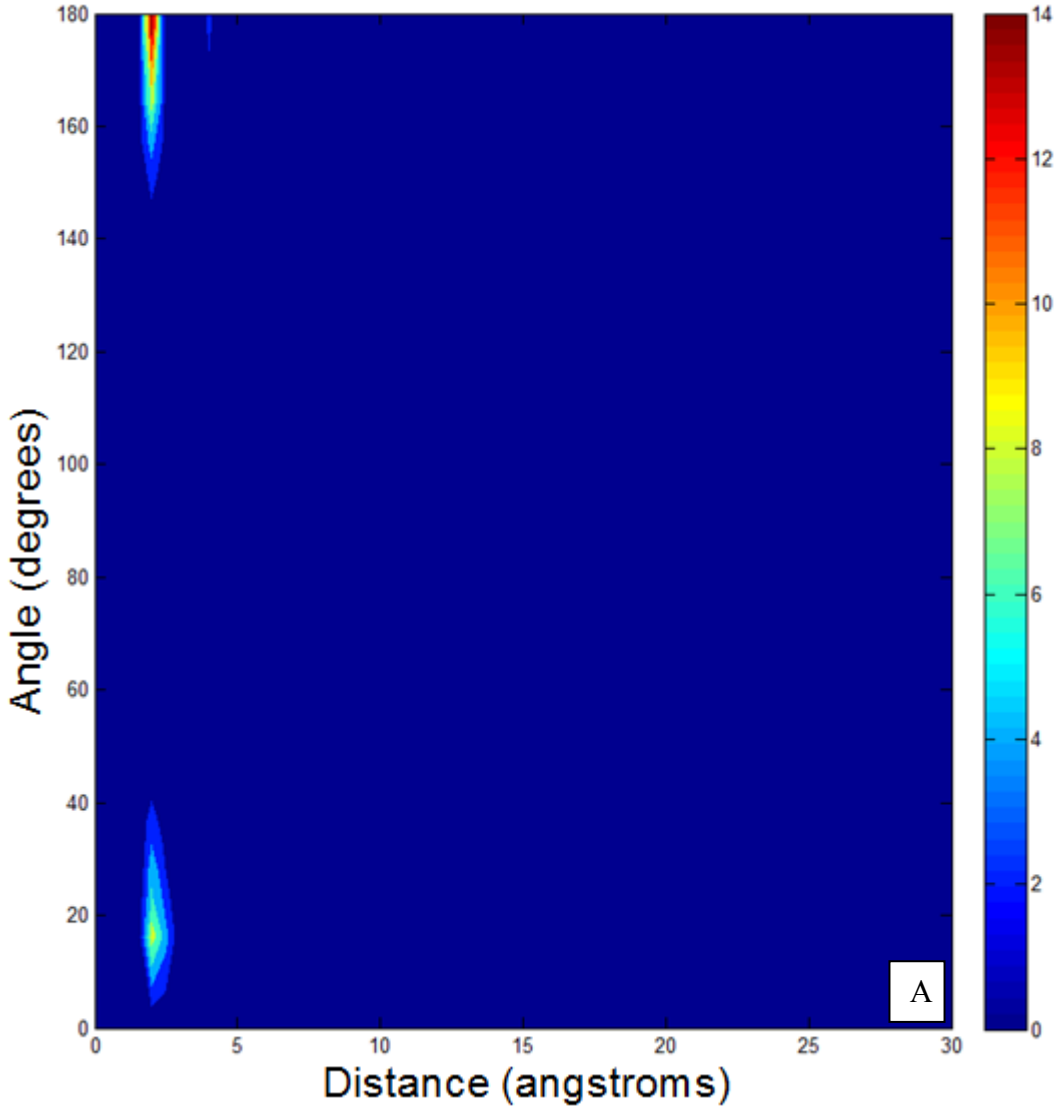

Figure 2.13 - Water dipole moment density distribution contour (A) and hydrogen atoms position density distribution (B) of CaF_2 (110).

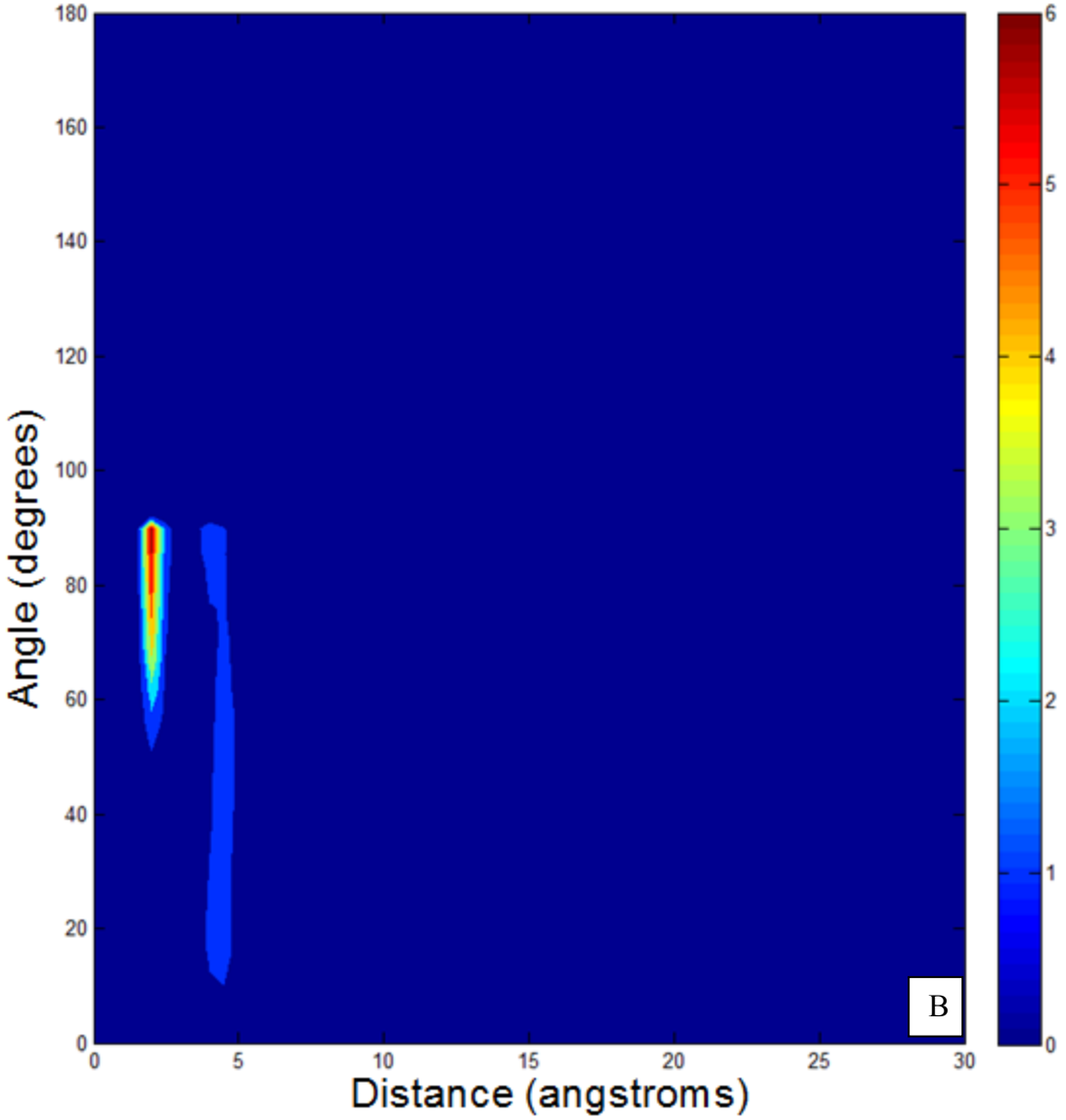

Figure 2.13 – Continued.

Table 2.5 - Interfacial water orientation at fluorite surfaces.

Surface	Dipole orientation	Hydrogen-hydrogen line orientation
	θ	β
$CaF_2(111)$	15^o-30^o, 30^o-85^o, 140^o	15^o-90^o
$CaF_2(100)$	30^o -50^o	45^o - 65^o, 10^o-30^o
$CaF_2(110)$	10^o-30^o, 155^o -180^o	60^o- 90^o

be due to crystal structure arrangement along the 111 cryptographic surface. As is shown in Figure 2.2, the 111 surface is organized in a F^--Ca^{2+}-F^- triple layers stacking sequence, with fluoride ions exposed to the top layer and calcium ions in the sublayer. Thus, both fluoride ions at the topmost layer and calcium ions at the sublayer will interact with the interfacial water molecules. As a result, the dipole moments of interfacial water molecules are distributed widely. From the definition of electrical dipole moment and Figure 2.10, it can be seen that when the dipole moment orientation is smaller than 90^o, oxygen of interfacial water molecules are oriented towards the surface by surface calcium ions. Only a weak peak appears at around 140^o for the dipole moment orientation, which indicates that although fluoride ions play a role in orienting the water hydrogen towards the surface, they are not as powerful as divalent calcium ions. The finding that highest density of dipole moment distribution happens at about 18^o may be due to the stronger interaction between divalent oxygen of interfacial water molecules with divalent calcium than that of univalent fluoride ions with univalent water hydrogen. Based on this observation, it can also be suggested that the sublayer calcium ions at the 111 surface of fluorite may also contribute to the surface charge to a significant degree. Although it has been previously found that the 111 surface exhibits a negative surface charge, our streaming potential measurements for this dissertation research found that the 111 surface is actually positively charged when cleaned with plasma. The cleaning methods effect on surface charge will be discussed in the next section.

Figure 2.12 shows the dipole moment density and hydrogen atoms position for the 100 surface of fluorite. It can be seen that the dipole moment orientation of interfacial water ranges from 30^o to 50^o with a sharp center ~40^o. The hydrogen atoms' position

orientation have two distinct distribution peaks corresponding to the primary and secondary water layer, respectively; one ranges from 45^o to 65^o centering at 55^o and the other ranges from about 10^o to 30^o with a center around 18^o. These results imply that almost all oxygen of the primary layer interfacial water molecules are oriented towards the 100 surface of fluorite; while for the second layer of interfacial water, the dipole moment orientation is more evenly distributed, although the dipole moment is almost all below 90^o. This may be attributed to the exposed surface calcium ions, which are positively charged and can attract the negatively charged divalent oxygen of interfacial water molecules. Consequently, the dipole moments of interfacial water molecule at the 100 surface of fluorite all are about 40^o. This is also consistent with the streaming potential measurement that the 100 surface is positively charged, which will be discussed in the next section. Besides, the orientation of hydrogen atoms for the primary water layer is larger compared to the second water layer, which means that for the second water layer, further from the surface, water hydrogen atoms are oriented to the surface to a much greater degree.

For the 110 surface, both calcium ions and fluoride ions are at the surface, as shown in Figure 2.4. The dipole moment density distribution of the 110 surface of fluorite shown in Figure 2.13 exhibits two distinct distribution peaks centering at about 18^o and 175^o, respectively. The reason for this is rather straightforward. The presence of both fluoride ions and calcium ions at the surface gives rise to these two different water dipole moment distributions. The hydrogen atoms position orientation ranges from 60^o- 90^o with a sharp peak close to 90^o. This suggests that the direction of hydrogen atoms of interfacial water is preferentially perpendicular to the 110 surface of fluorite.

2.1.3.3 Sum Frequency Vibrational Spectroscopy (SFVS)

In this dissertation research, the OH stretching bands of interfacial water molecules have been examined. Previous SFVS studies (Freysz et al., 1994; Kim et al., 2001; Ye et al., 2001; Ostroverkhov et al., 2004) of solid/water interfaces have described the interfacial water by three main peaks: ~3200 cm^{-1}, ~3450 $cm^{-1}$and ~3700 cm^{-1}. These peaks represent broad spectral features and have been assigned based on the extent of intermolecular hydrogen bonding. The 3200 cm^{-1} peak represents the OH stretching from water molecules with strong hydrogen bonded OH stretching. The 3450 cm^{-1} peak arises from asymmetrically bonded water molecules with either asymmetric or bifurcated hydrogen bonds. The sharper 3700 cm^{-1} peak has been assigned to the stretching mode for a free OH vibration, which is the weakly coupled or uncoupled OH stretching mode of straddling interfacial water molecules, which have nonhydrogen bonded OH groups oriented toward the surface.

Previous SFVS study of the fluorite/ water interface examined the effect of pH on the SFVS spectra and a strong pH dependence was found (Becraft and Richmond, 2001). However, it should be noted that surface carbonation of fluorite will happen at pH > 8 (Miller and Hiskey, 1972). In this regard, the SFVS spectra might not be reflecting the actual characteristics of a fluorite surface at pH > 8, but rather that of a carbonated surface.

The present study was conducted in the absence of surfactant at near-neutral pH conditions (pH=5.7). The objective is to compare the SFVS response for two different fluorite surfaces: the 111 surface and the 100 surface. Based on the previous results from contact angle measurements, it was concluded that the 100 surface of fluorite is

completely hydrophilic, while the 111 surface of fluorite exhibits moderate hydrophobicity (Zhang et al., 2012). This wettability difference has been attributed to the difference in surface structure. The exposed layer of the 100 surface of fluorite, as shown in Figure 2.3, consists of divalent calcium ions, while the exposed layer of the 111 surface (Figure 2.2) consists of fluoride ions. It is expected that the interaction of water with divalent calcium ions of the 100 surface of fluorite will be stronger than the interaction of water with the univalent fluoride ions of the 111 surface. Consequently, the 100 surface of fluorite is more easily hydrated by interfacial water molecules and is completely hydrophilic. In contrast, it is expected that water interaction at the 111 surface of fluorite is weaker. Thus the 111 surface will be of lower polarity and somewhat hydrophobic.

Sum-frequency vibrational spectroscopy (SFVS) studies on the 111 and 100 surfaces of fluorite confirm this difference in wettability. The 3200 cm^{-1}, 3450 $cm^{-1}$and 3700 cm^{-1} peaks represent OH stretching mode from strongly hydrogen bonded water molecules, asymmetrically bonded water molecules with either asymmetric or bifurcated hydrogen bonds, and free OH vibrations mode of straddling interfacial water molecules, respectively (Becraft and Richmond, 2001; Du et al., 1994b; Tyrode and Liljeblad, 2012). Other explanations have been offered in the literature (Nihonyanagi et al., 2011; Tyrode and Liljeblad, 2012). See Figure 2.14. The 111 surface exhibits two main peaks at 3200 cm^{-1} and 3450 cm^{-1}. At 3700 cm^{-1}, only a small peak is found. For the 100 surface, the 3200 cm^{-1} peak is much stronger than the 111 surface, with a small shoulder at 3500 cm^{-1}. No free OH peak was found for the 100 surface. The much higher intensity of the ~3200 cm^{-1} peak and the much lower intensity of the ~3500 cm^{-1} peak of the 100 surface

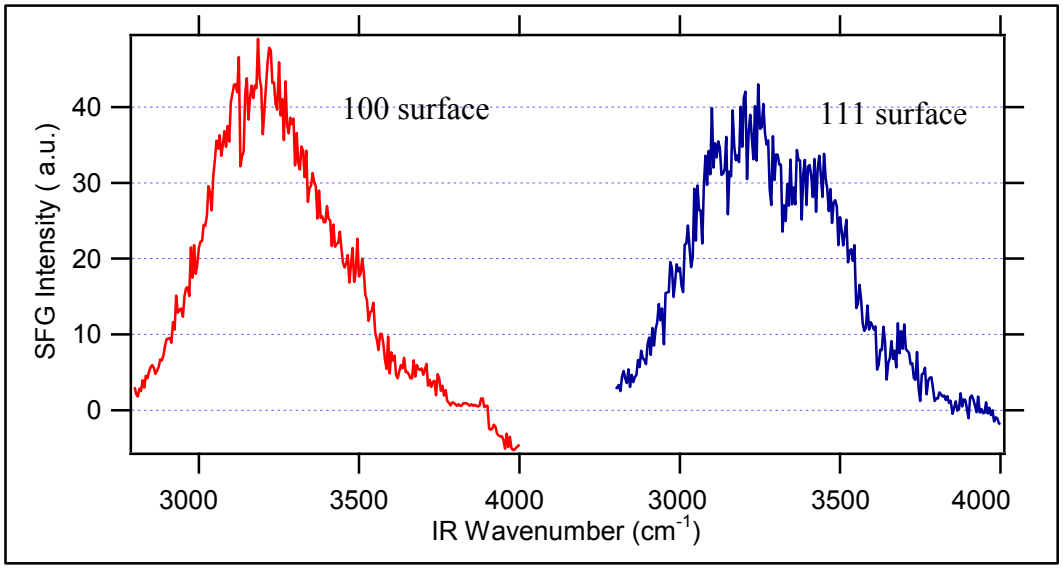

Figure 2.14 - SFVS spectra (SSP) of the 111 (right) and 100 (left) surfaces of fluorite\water interface (spectra normalized to lasers energy, natural pH=5.7, ionic strength is not controlled).

suggests that interfacial water molecules are more ordered at the 100 surface than at the 111 surface of fluorite. The presence of the small ~3700 cm^{-1} at the 111 surface of fluorite indicates moderate hydrophobicity of the surface. These results suggest that the 100 surface is more strongly hydrated by interfacial water molecules and that interfacial water molecules are more ordered than at the 111 surface of fluorite. Discussions on SFVS spectra of hydrophobic and hydrophilic surfaces have been given by many other researchers (Du et al., 1994a; Du et al., 1994b; Ye et al., 2001). Ye et al. studied interfacial water structure on a fused quartz modified by octadecyltrichlorosilane (OTS) and obtained the SFVS spectra with low coverage of OTS. The results show that although there is a decreased level of hydrophobicity at low coverage of OTS, compared to full monolayer coverage of OTS, the presence of a small peak at ~3700 cm^{-1} describes its modest hydrophobicity (Ye et al., 2001), which spectrum resembles the spectrum of the

111 surface of fluorite as shown in Figure 2.14 (right). These results are consistent with the conclusion that the 111 surface exhibits modest hydrophobicity. Du et al. (Du et al., 1994) studied the SFVS spectra of quartz ice interface, the dominating peak in the OH vibrational region was found to be ~3200 cm^{-1}, with a small shoulder at ~3400 cm^{-1}. No free OH peak (~3700 cm^{-1}) was detected. The results are similar to the SFVS spectrum of the CaF_2(100)\water interface as shown in Figure 2.14 (left), which confirms the conclusion that the 100 surface of fluorite is hydrophilic. As discussed above, the interaction with divalent oxygen of interfacial water, caused by divalent calcium ions at the 100 surface of fluorite, is stronger and as a result, the interfacial water molecules are more ordered. In contrast, the interaction between univalent fluoride ions of the 111 surface of fluorite with univalent hydrogen of water is weaker, resulting in a reduced level of hydration. The appearance of the weak free OH peak for the 111 surface suggests that there is an exclusion zone between the 111 surface and the interfacial water molecules. These spectral differences are consistent with contact angle and MDS results. The 100 surface of fluorite is completely hydrophilic; while the 111 surface exhibits moderate hydrophobicity. The findings in Figure 2.14 indicate that surface structure plays an important role for the wetting characteristics of mineral surfaces. Study of the wettability of different crystal surfaces provides fundamental understanding for the interaction of water with mineral surfaces.

2.1.4 Results for Equilibrium State (in saturated CaF_2 solution)

Results presented in the previous section for contact angle, molecular dynamics simulations (MDS), and sum-frequency vibrational spectroscopy (SFVS) are for the nonequilibrium state in that the fluorite surfaces examined had not reached chemical

equilibrium with the aqueous phase, the aqueous phase was not saturated with respect to calcium fluoride.

In this section, contact angle measurements are reported for a saturated CaF_2 solution.

Chemical equilibration for these optical windows of fluorite with the aqueous phase is very slow, taking many days to reach saturation. Further, it should be noted that recrystallization to the 111 surface occurs during such equilibration (Puchin et al., 2001; Schick et al., 2004). When the aqueous phase is prepared as a saturated calcium fluoride solution, the surface properties change. For example, all the surfaces appear to recrystallize as the 111 surface and exhibit contact angles of ~20^o. See Table 2.6.

Further evidence of the effect of equilibration on the surface characteristics is that the sign of the surface charge of the 111 fluorite surface changes from a negatively charged surface in water to a positively charged surface in saturated calcium fluoride solution as preferential hydration of lattice fluoride ions results in a surface excess of calcium ions (Miller et al., 2004).

2.1.5 Summary

The wetting characteristics of different fluorite surfaces (111, 100 and 110) were investigated using contact angle measurements, molecular dynamics simulation (MDS) and sum frequency vibrational spectroscopy (SFVS). Nonequilibrium contact angle results indicate that the 111 surface of fluorite exhibit modest hydrophobicity, with a contact angle of ~20^o, while the 100 and 110 surfaces are completely hydrophilic indicated by their 0^o contact angles. MD simulations for a water drop at the 111 and 110 surfaces of fluorite were also conducted and the advancing contact angles were found to

Table 2.6 - Intermediate contact angle at different fluorite crystal surfaces.

Crystal surface	Nonequilibrium state DI water	Equilibrium state Saturated CaF_2 solution
111	20^o	28^o
110	0^o	14^o
100	0^o	26^o

be ~13^o for the 111 surface and 0^o for the 110 surface. This is consistent with the water contact angle result that the 111 surface has some degree of hydrophobicity; while the 110 surface is hydrophilic.

The interfacial water structure at different fluorite surfaces was further analyzed by molecular dynamics simulation (MDS). Fluorite surfaces of different crystallographic orientations were created and a water box containing the surface was built for the 111 and 100 surfaces, respectively. Results from MDS show that interfacial water molecules were closely packed at the 100 surface of fluorite, while for the 111 surface, a water exclusion zone was present. The water density distribution profiles for the 111 and 100 surfaces were also studied. The results suggest that the interaction of interfacial water molecules with the 100 surface of fluorite is much stronger than with the 111 surface of fluorite. There are three water layers interacting with the 100 surface of fluorite. While only two water layers are identified to be interacting with the 111 surface of fluorite. Residence time analysis indicate that interfacial water molecules tends to stay at the 100 surface of fluorite much longer than at the 111 surface of fluorite, which is consistent with the water density results. Again, this confirms the conclusion that the 111 surface has a modest degree of hydrophobicity, while the 100 surface of fluorite is hydrophilic. MD simulations for a water drop at the 111 and 110 surfaces of fluorite were also conducted

and the advancing contact angles were found to be ~13^{o} for the 111 surface and 0^{o} for the 110 surface. This further confirmed the water contact angle result that the 111 surface has some degree of hydrophobicity; while the 110 surface is hydrophilic.

The reason for this variation in wetting characteristics of different fluorite surfaces has been attributed to difference in the surface structure. For the 111 surface, fluoride ions are exposed to the surface. Density functional theory (DFT) calculations and atomistic simulations have shown that the main interaction between the fluorite surface and the interfacial water molecules is the binding of water molecule's oxygen atoms to surface calcium atoms (de Leeuw and Cooper, 2003). Calcium ions are divalent and have a much stronger interaction with divalent oxygen of interfacial water molecules than that of monovalent fluorides with monovalent hydrogen. Thus, the presence of fluoride ions at the 111 surface of fluorite will weaken the interaction between fluorite surface and interfacial water molecules to some degree and impose a moderate degree of hydrophobicity for the surface. While for the 100 surface of fluorite, calcium ions are exposed on the surface, intense interaction between divalent calcium ions and divalent water oxygen exists and as a result, complete hydration occurs on the surface, giving rise to higher interfacial water density, more interacting water layers and close packing of the primary water layer at the surface.

Detailed analysis of hydration states at different fluorite surfaces (111 and 100) were conducted through SFVS experiments. Results from SFVS confirmed contact angle measurements and MD simulations that the 111 surface is moderately hydrophobic, indicated by the presence of the free OH peak located at 3700 cm^{-1}. This peak represents the weakly coupled or uncoupled OH stretching mode of straddling interfacial water

molecules and have nonhydrogen bonded OH groups oriented toward the surface. The 100 surface is confirmed to be completely hydrophilic due to the absence of the free OH peak and the strong intensity of the 3200 cm^{-1} peak, representing the OH stretching from water molecules with strong hydrogen bonded OH stretching.

2.2 Surface Charge Characteristics of Fluorite Surfaces

2.2.1 Introduction

The objective of this section is to characterize the surface charge of different fluorite surfaces (111, 100 and 110). Streaming potential measurements have been made at three different flat plate fluorite surfaces using the clamping cell with polypropylene as the reference material. The effect of surface structure/composition on the charge exhibited will be discussed including the significance of the sample preparation procedure.

2.2.2 Materials and Methods

2.2.2.1 Sample Preparation

Three fluorite crystals, having different surfaces (111, 100 and 110) were used for streaming potential measurements. These optical grade fluorite crystals, with the desired crystal surfaces, were purchased from Almaz Optics. The surface planes for each of the crystals were confirmed by X-ray diffraction analysis.

The fluorite samples were cleaned with three different methods: 1. cleaning with only DI water; 2. cleaning with acetone, ethyl alcohol, and copious amounts of deionized water followed by drying with high-purity nitrogen; 3. following method 2, the samples were then treated with plasma and again dried with high-purity nitrogen gas. All other glassware and plasticware were cleaned by rinsing with acetone, methanol, copious amounts of deionized water, and dried by high-purity nitrogen gas. Deionized water was

obtained from a Milli-Q system. The resistivity of the water was above 18 MΩ in all experiments.

2.2.2.2 Streaming Potential Measurements

A commercial Electrokinetic Analyzer (SurPASS, Anton Paar) was used to investigate the zeta potential of flat plate surfaces of fluorite based on streaming potential and streaming current measurements. The zeta potential is related to the surface charge at a solid/liquid interface and is an important indicator of the surface chemistry and adsorption processes. The zeta potential is the electric potential in the electrochemical double layer at the location of the shear plane. The plane of shear separates the immobile Stern layer from the mobile or diffuse layer. During the relative movement between the solid and liquid phases, the diffuse layer is sheared off and as a result a potential difference is created. This is defined as the streaming potential, and originates when an electrolyte is driven by a pressure gradient through a channel or porous plug with charged walls.

The SurPASS electrokinetic analyzer in our lab contains a new clamping cell arranged in an asymmetric geometry, in which a reference material surface is used and nondestructive measurement of flat plate crystal samples can be conducted. See Figure 2.15. An aqueous electrolyte solution is driven to flow through the clamping cell with the solid sample by a dual syringe system. A gap is created between the flat solid surfaces and can be adjusted to generate a pressure difference between the inlet and outlet of the clamping cell. A spacer was placed in between the reference and the test sample to (fluorite crystal of specified crystallographic plane) form a rectangular channel. The large width to depth ratio of the spacer makes the contribution from the wall to minimum value.

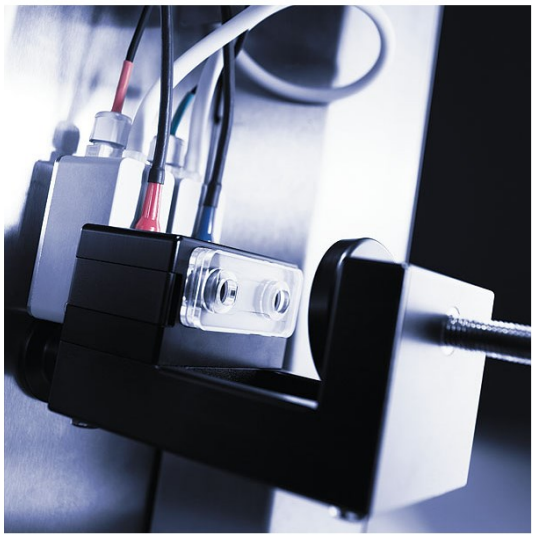

Figure 2.15 – Picture of the clamping cell.

Ag/AgCl electrodes are applied here and inlet and outlet tubes are used for electrolyte circulation. The SurPASS electrokintic Analyzer contains HCl and NaOH syringes and tubing with a pH electrode, which are for pH titration experiments.

The electrolyte flow will also give rise to electrical charge separation in the flow direction along the measuring cell and, as a result, a potential difference (streaming potential, ΔU) or electrical current (streaming current, ΔI) can be generated and the two electrodes used for measuring these values. The measured values of ΔP (pressure difference) and ΔU or ΔI are used for calculating the zeta potential. The SurPASS Monitor of the Visio Lab for SurPASS software serves to control measuring parameters as well as other procedures such as fill, rinse, flow check, empty, etc. Figure 2.15 shows a picture of the clamping cell. Figure 2.16 shows the schematic drawing of the sample stack in the SurPASS clamping cell.

In the clamping cell, the sample and reference surfaces are separated by a spacer

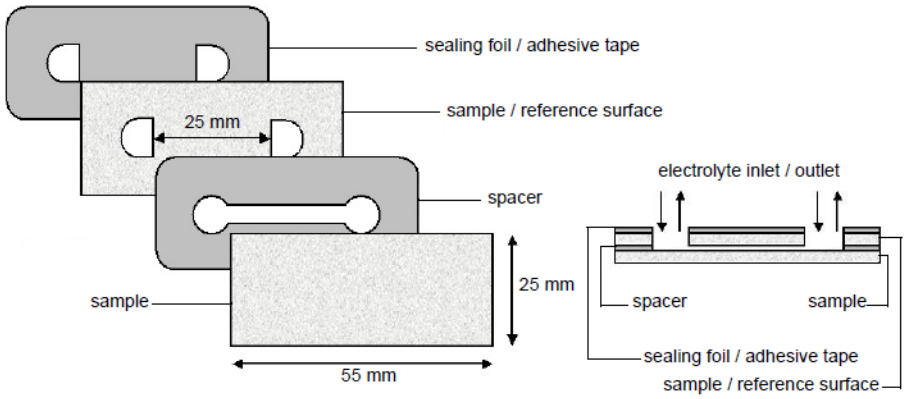

Figure 2.16 – Schematic drawing of the sample stack in the SurPASS clamping cell.

which introduces a well defined gap. As the dimension of this gap is much smaller than the width and length, the total measured zeta potential (ζ_{TOT}) is the average potential of reference and sample surfaces. With:

$$\zeta_{TOT} = \frac{1}{2}\,\zeta_{REF} + \frac{1}{2}\,\zeta_{S} \qquad (2\text{-}10)$$

the zeta potential of the sample surface ζ_S is calculated as

$$\zeta_S = 2\,\zeta_{TOT} - \zeta_{REF} \qquad (2\text{-}11)$$

In order to determine the zeta potential of test samples, the zeta potential of the reference polypropylene surface is measured first, denoted as ζ_{REF}. Then the average potentials for the reference and sample surfaces ζ_{TOT} are measured. Finally, the zeta potential of the test sample surface is calculated from equation 2-11.

The streaming potential measurements were performed in 1 mM KCl background electrolyte. Before each experiment, first, cleaning of the instrument was conducted using

at least 2 liters of 18 MΩMilli-Q water. If contamination was present in the system, ethyl alcohol and large amount of 18 MΩMilli-Q water was used to clean the instrument. Then pH titration experiment with the polypropylene as the test sample (the clamping cell organized with a symmetric geometry) was conducted. The purpose of this is to detect whether the point of zero charge (PZC) of polypropylene will fall between pH 3.8 to 4.2. If yes, asymmetric testing of the unknown surface can be done. Otherwise, there might be some contamination for the instrument and further cleaning may be necessary.

2.2.3 Results and Discussion

2.2.3.1 Flat Plate Streaming Potential Measurements (FPSP)

Three fluorite crystals, having different surfaces (111, 100 and 110) were used for streaming potential measurements. Before each experiment, the pH titration experiment was conducted for the reference polypropylene surface to detect whether the PZC will fall between pH 3.8-4.2. Figure 2.17 shows the pH titration result. From Figure 2.17, it can be concluded that the instrument is in good condition, thus the zeta potential at the 111, 100 and 110 surfaces of fluorite were measured. The results are shown in Table 2.7.

From Table 2.7, it can be seen that the cleaning procedure has a significant effect on the zeta potential of fluorite surfaces. When cleaned with only DI water, the zeta potentials for both the 111 and 100 surfaces of fluorite are -21 and -22 mV, respectively. However, it was observed that the surfaces were not well hydrated by water when cleaned using this method. This indicates that there might be some contamination on the surface, leading to a moderate hydrophobic surface state.

When the surfaces were cleaned without plasma, but by using acetone, ethyl alcohol and DI water, and at the same time, removing any possible contamination by polishing

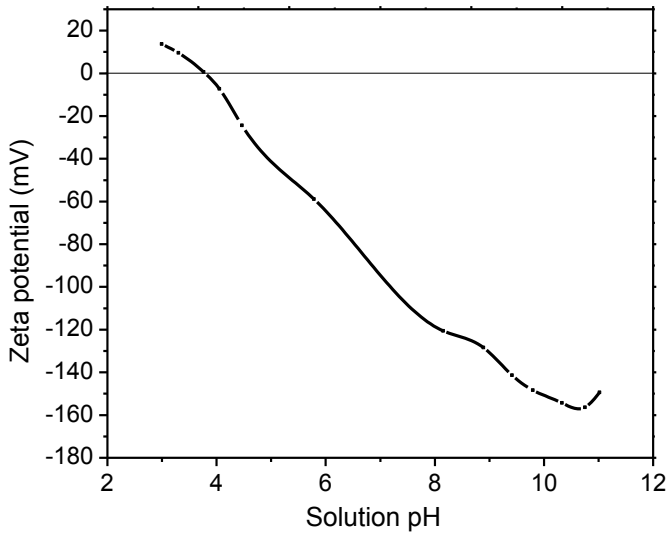

Figure 2.17 - Zeta potential of polypropylene as a function of solution pH (1mM KCl).

Table 2.7 - Zeta potential at different fluorite crystal surface (flat plate streaming potential measurement, 1mM KCl background) pH=5.7 in nonequilibrium state.

Cleaning procedure	CaF_2(111)	CaF_2(100)	CaF_2(110)	Mica
Plasma clean	62	30	66	-97
No plasma (only with DI water) clean	-21	-22		-79
No plasma (acetone, alcohol, DI water)	32	12	30	

the surfaces by hand with gloves, the fluorite surfaces became more hydrophilic and a better hydration of water at the surfaces was observed. The zeta potentials of the three surfaces are all positive.

When the fluorite surfaces were cleaned with plasma, the zeta potentials for these three surfaces became even more positive.

It is rather surprising to find that when cleaning the fluorite surfaces with plasma, the 111 surface of fluorite is positively charged, because for the 111 surface of fluorite, the cleaved surface is composed of fluoride ions, as is shown in Figure 2.2. This low energy surface is created by breakage of fluoride/ fluoride bonds. Besides, a negative surface charge was previously found for the 111 surface of fluorite (Miller et al., 2004). However, the previous measurement was conducted by cleaning the 111 surface of fluorite with only DI water. Based on these discussions, when cleaning fluorite with only DI water, the surface charge of fluorite 111 surface is -21 mV, which is consistent with the previous result. However, this -21 mV zeta potential might not be reflecting the real surface charge characteristics due to surface contamination. When cleaning the surface without plasma, but with acetone, alcohol and DI water to the extent that the surfaces become as hydrophilic as possible; the surface charge becomes positive for both the 111 and 100 surfaces. When cleaning with plasma, all the three surfaces are even more positive. These results seem to contradict the previous discussion that fluoride ions are exposed at the 111 surface. However, recall the dipole moment analysis with MD simulations in section 2.1.3.2. The dipole moment density distribution and hydrogen atoms position data presented in Figure 2.11 suggest that the sublayer calcium ions at the 111 surface of fluorite interact with interfacial water molecules significantly as indicated

from the dipole moment density distribution profile. Thus, it is reasonable to conclude that the sublayer calcium ions may contribute to the surface charge significantly, giving rise to a positive surface charge. It has also been reported that treating fluorite surface with plasma may bring some changes on the surface (Wang and Maier, 2004; Wang et al., 2007), which may also have an effect on the surface charge features of fluorite.

To verify that our experimental measurements are correct, the zeta potential of mica surface was also measured by FPSP with two different cleaning methods: one cleaning was done only with DI water and the other with plasma. The zeta potential result is consistent with reported values in the literature (Zembala and Adamczyk, 1999).

From Table 2.7, it can be seen that for mica, cleaning with plasma does not influence its zeta potential a lot. The reason for this is that mica has a sheet, a trilayer structure. The basic units of mica consist of two polymerized sheets of silica (SiO_4) tetrahedrons. The silica tetrahedral face surfaces of mica are negatively charged due to lattice substitution. Further, since mica has a layered structure, a fresh surface can be created simply by removing a layer and conducting the measurement. Thus, contamination problems are avoided. When cleaned with plasma, the negative surface charge increased by 18 mV. This might be due to an increase in surface roughness of the mica surface, leading to an increase in surface charge density.

Applying different cleaning methods, comparing the zeta potential results of fluorite surfaces and mica, it is then evident that fluorite is more easily contaminated than mica; thus, fluorite is more sensitive to the cleaning procedure. Because the fluorite surface is exposed to the atmosphere, contaminants may adsorb on the surface, while a fresh mica surface can be created for every measurement, making it free from contamination.

In the case of the 100 surface, the surface may be either dominated by calcium ions or fluoride ions and the surface is created by fracture of the ionic bond. The finding of a positive zeta potential of 30 mV (Table 2.7) when cleaned with plasma at the 100 surface is evidence for the exposure of surface calcium ions. The 100 surface with exposed calcium ions at the surface is shown in Figure 2.3 in a cross sectional view.

For the 110 surface of fluorite, there are both calcium and fluoride ions on the surface. Consequently, either a negative surface charge or a positive surface charge can be expected. The finding of a positive surface charge at 110 surface of fluorite by FPSP measurement indicates that calcium ions play a more significant role in the electrokinetic behavior of the surface.

2.2.4 Summary

Flat plate streaming potential measurements were conducted at three different fluorite surfaces (111, 100 and 110). Results show that the cleaning procedure has a significant effect on the surface charge of fluorite for the nonequilibrium state. When cleaning fluorite with only DI water, both the 111 and 100 surfaces show a negative surface charge, while when measuring the contact angle of the two surfaces under this condition, both surfaces show a moderate hydrophobicity as observed during cleaning. This indicates the presence of contamination at the surface. These contaminations might be the reason for the apparent negative surface charge of both surfaces.

Thus, different cleaning methods were applied and their zeta potential as well as corresponding contact angles were measured for the 111, 100 and 110 surfaces. Experimental results show that when the surfaces are free from contamination, a positive zeta potential was obtained for all three surfaces. The result of a positive surface charge

for the 111 surface of fluorite seems to contradict the previous result that the 111 surface is negatively charged (Miller et al., 2004). However, in previous research, the effect of the cleaning procedure was not considered and the surface was cleaned with only DI water. As discussed above and as shown from contact angle results, there appears to be contamination when cleaning with only DI water. As a result, the zeta potential measured under this condition might not be reflecting the real surface charge of fluorite. As the 111 surface of fluorite is exposed with fluoride ions, a negative surface might be expected. However, from our dipole moment distribution analysis from MD simulation presented in section 2.1.3.2 and from Figure 2.11, it can be argued that the sublayer calcium ions are playing a significant role, contributing to the surface charge and giving rise to the positive sign. The finding of a positive surface charge of the 100 surface of fluorite in the absence of contamination suggests that calcium ions are exposed at the surface.

For the 110 surface of fluorite, as both the fluoride and calcium ions are present at the surface, either a negative surface charge or a positive surface charge can be expected. When the surface is free from contamination, the finding of a positive surface charge indicates that calcium ions play a more significant role in the electrokinetic behavior of the surface.

In contrast to the above summary for the nonequilibrium state, considerable difference was found when the equilibrium state (solution saturated with CaF_2) was examined. When the aqueous phase is prepared as a saturated calcium fluoride solution, the surface properties change. All the surfaces appear to recrystallize as the 111 surface and exhibit contact angles of ~20^o. Furthermore, the sign of the surface charge of the 111 fluorite surface changes from a negatively charged surface in water to a positively

charged surface in saturated calcium fluoride solution as preferential hydration of lattice fluoride ions results in a surface excess of calcium ions (Miller et al., 2004).

CHAPTER 3

SURFACE CHEMISTRY OF BASTNAESITE

3.1 Introduction

Rare earth elements are crucial to manufacturing many advanced products and have broad commercial and military applications. They are critical in modern electronic technologies including electronic systems and military applications such as new catalysts for automotive exhaust systems, permanent magnets for computer equipment, hydrogen storage and fueling systems for equipment in confined areas (Fuerstenau, 1988), cellphones, large wind turbines and guided missiles, TVs, fluorescent light bulbs, as well as medical diagnosis equipment and almost all military systems. When the rare-earths are alloyed with other metals, enhanced magnetic properties, strength, use at high temperature and other properties can be achieved. For example, the high-strength magnets widely used in a variety of products including electric motors and hybrid car components are made from neodymium-iron-boron. Bastnaesite ((Ce, La) FCO_3) is a principal mineral resource for rare earth elements and bastnaesite is generally recovered by flotation. In this regard, investigation on the surface chemistry features including electrokinetic behavior, wetting characteristic and collector adsorption by bastnaesite is an important topic for research.

As mentioned earlier, the interfacial features of the mineral/water interface greatly affect flotation separation and recovery. For rare-earth semisoluble salt minerals, the

surface charge is also pH dependent and is influenced by lattice ion hydration. Thus, the electrokinetic behavior of rare-earth minerals may have a significant effect on the wetting characteristics as well as collector adsorption. Investigation of properties such as the zeta potential, contact angle and the interaction between interfacial water and crystal surfaces will definitely help us to have a better understanding of the surface chemistry of bastnaesite. In this regard, it is expected that fundamental studies will provide a basis for important contributions to be made in flotation technology for the recovery of rare-earth minerals.

In this portion of the dissertation research, the electrokinetic behavior of bastnaesite is studied by electrophoresis. The wetting characteristics of bastnaesite are investigated experimentally and using molecular dynamics simulation (MDS). Particularly, the interfacial chemistry of bastnaesite is considered with respect to collector adsorption features, specifically the collector, octyl hydroxamate.

3.2 Materials and Methods

3.2.1 Sample Preparation

For microelectrophoresis and adsorption measurements, bastnaesite samples from Zagi Mountain, Pakistan were dry ground to -45 μm. Prepared samples were confirmed to be bastnaesite by X-ray diffraction. The surface area of the ground samples was evaluated by the Brunauer-Emmett-Teller (BET) adsorption method utilizing nitrogen gas with a Micromeritics ASAP 2020 analyzer. The surface area was found to be 0.7622 m^2/g. Before electrokinetic measurements, 0.1% particle suspensions were centrifuged for 10 minutes and the supernatant suspension was taken for the experiments.

Research grade octyl hydroxamic acid ($CH_3(CH_2)_6$ CONHOH) of high purity from

Cytec was used to investigate the adsorption density at low concentrations of hydroxamate, the hydrophobic surface state of bastnaesite (contact angle measurements), and to characterize the adsorbed hydroxamate by sum-frequency vibrational spectroscopy (SFVS). Figure 3.1 shows the structure of octyl hydroxamic acid.

For contact angle measurements with and without hydroxamate adsorption, a piece of bastnaesite sample from Zagi Mountain, Pakistan was first polished and the surface roughness was measured using atomic force microscope (AFM). The surface roughness listed here is the root-mean-square roughness R_q, which is the root-mean-square deviation from the mean elevation and was found to be 26.4 nm. The bastnaesite surface was cleaned by rinsing with acetone, methanol, and copious amounts of deionized water, followed by drying with high-purity nitrogen. The samples were then polished with 0.05μm gamma alumina powders on a polishing cloth and again dried with high-purity nitrogen gas.

3.2.2 Electrophoresis Measurements

Zeta potential is the electric potential in the interfacial double layer at the slipping plane and can be affected by pH and solution composition (Schwer and Kenndler, 1991). It is widely used for quantification of the magnitude of the electrical charge. In the present study of this dissertation, bastnaesite samples from Zagi Mountain, Pakistan were dry ground to -45 μm. Prepared samples were confirmed to be bastnaesite by X-ray diffraction. Before measurement, bastnaesite suspensions of 0.1% were prepared and centrifuged for 10 minutes. Zeta potentials of bastnaesite (Zagi Mountain, Pakistan) were measured using ZetaPALS instrument, Brockhaven Instruments Corporation, whose measurements are based on the doppler effect combined with a phase shift of the

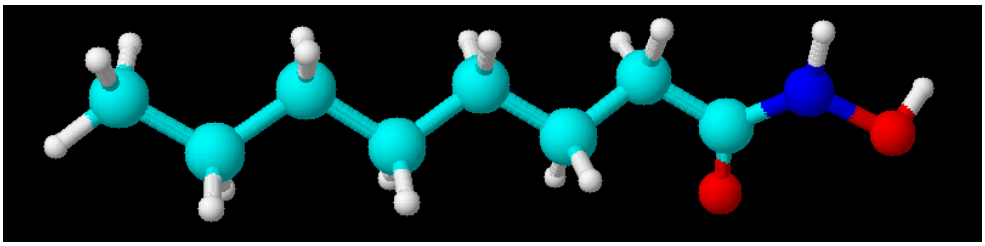

Figure 3.1 – Structure of octyl hydroxamic acid (Red: oxygen; Blue: nitrogen; Light blue: carbon: White: hydrogen).

reflected light. Bastnaesite particles mobilities were measured at varying pH and then converted to zeta-potentials (ξ) using Smoluchowski's model as follows:

$$U = \frac{\varepsilon\zeta}{4\pi\eta} E_{\infty} \tag{3-1}$$

where U is the particle mobility, E_{∞} is the applied electric field, and ε and η are the dielectric constant and viscosity of the solvent.

3.2.3 Adsorption Density Determinations

3.2.3.1 Dynamic Light Scattering Measurements

In order to investigate the solution concentration limitation of octyl hydroxamic acid in DI water, the solubility was measured using the dynamic light scattering (DSL) technique. A Zetasizer Nano ZSP instrument from Malvern Instruments was used for the measurements. Dynamic light scattering, which is also known as photon correlation spectroscopy or quasi-elastic light scattering, is a technique that can be used to determine the size distribution profile of small particles in suspensions (Goldburg, 1999). It is an important tool to characterize the size of nanoparticles in solution. The working principle is that a light or a laser beam hits small particles, the light scatters in all directions, which

is called Rayleigh scattering. The experiment's theory assumes that the particles are in Brownian motion (also mentioned as "random walk") and that the particles are spherical with a diameter as small as the molecular dimensions level. When a laser beam light source, which is monochromatic and coherent, shines onto a solution with spherical particles in Brownian motion, a doppler shift can be caused. This changes the wavelength of the incoming light, which is related to the size of particle. Scattering of light by particles in the solution enables imprinting of information on their motion. By analyzing the fluctuation of the scattered light, information on the particle can be obtained. The Stoke-Einstein relation is applied for calculation of the diffusion coefficient of the particles (D):

$$D = \frac{kT}{6\pi R\eta} \tag{3-2}$$

where k is the Boltzmann constant, T is the temperature in Kelvin degrees and η is the viscosity of the solvent. Thus, the radius (R) of the particles can be calculated from the above equation.

3.2.3.2 Adsorption Density Determinations

Adsorption density determinations were made by the solution depletion method using high sensitivity total organic carbon (TOC) analysis for low concentrations of hydroxamic acid.

A commercial total organic carbon analyzer (model: TOC-$V_{CPH/CPN}$) from SHIMADZU corporation was used for measurements of total organic carbon concentration of hydroxamate solution before and after adsorption (SHIMADZU). Eventually, adsorption density can be calculated from residual hydroxamic acid

concentration and the BET surface area of 0.7622 m^2/g.

Total organic carbon (TOC) is the amount of carbon bound in an organic compound. High sensitivity TOC refers to use of high sensitivity catalyst to measure trace amounts (commonly 0.5 ppm or less) of TOC in samples such as ultra-pure water. A typical analysis for TOC utilizes the TC-IC (total carbon-inorganic carbon) method, which measures both the total carbon present and the so-called "inorganic carbon" (IC). Subtracting the inorganic carbon (IC), which represents the content of dissolved carbon dioxide and carbonic acid salts, from the total carbon yields TOC. Another common variant of TOC analysis involves removing the IC portion first and then measuring the leftover carbon, which involves purging an acidified sample with carbon free air prior to measurement, and so is called non-purgeable organic carbon (NPOC). The NPOC analysis is recommended for TOC concentrations of 100 ppb or less. In this dissertation, high sensitivity TOC with NPOC analysis was used to perform experiments of octyl hydroxamic acid adsorption at the bastnaesite surface and to establish the adsorption isotherm. The surface area of bastnaesite particles was obtained using Brunauer-Emmett-Teller (BET) method and the adsorption density was determined using the solution depletion method.

The adsorption isotherm for octyl hydroxamic acid adsorption at the bastnaesite surface was determined using the solution depletion method. Ultra-pure water was used for the preparation of hydroxamate solutions. Concentration of total organic carbon in the solution before and after adsorption was measured with high sensitivity TOC and adsorption density at bastnaesite surface was calculated. Octyl hydroxamic acid from Cytec was used for all adsorption experiments and the pH was maintained at pH 9.3. At

this pH, maximum flotation recovery was found (Pradip, 1981). Five different concentrations of hydroxamic acid were prepared, 1×10^{-5} M, 2×10^{-5} M, 5×10^{-5} M, 1×10^{-4} and 5×10^{-4} M. Bastnaesite powder samples of (0.5 g, particle size -45 μm) were mixed with 50 ml hydroxmaic acid solution with a solid to liquid ratio of 1 : 100. A blank test was also performed each time using ultra-pure water as the solution. The solutions containing bastnaesite as well as hydroxamate collector were then shaken at 200 rpm simultaneously for 4 hours on a Barnstead-Lab Line Max Q 2000 Orbital Shaker, followed by filtration and measurements of the residual hydroxamate by high sensitivity TOC. The concentration of hydroxamate solution before adsorption was also measured. Then the adsorption density was calculated based on the amount of adsorbed hydroxamate and the surface area of bastnaesite.

3.2.4 Contact Angle Measurements

Contact angles at the bastnaesite surface with and without octyl hydroxamate adsorption was measured with a Rame-Hart goniometer using both the captive bubble and sessile drop methods. The measurement of an intermediate contact angle was accomplished by the release of a bubble or a drop from the needle tip after formation with a syringe; the bubble or drop is then held at the bastnaesite surface, followed by attachment or spreading. The equilibrium contact angle is measured for all cases of attachment. In addition, advancing and receding contact angles were also measured. The advancing contact angle, which is the largest possible contact angle, was measured when decreasing the bubble volume or increasing the drop volume while attached to or spread over the surface. The receding contact angle, which is the smallest possible angle, was obtained when expanding the attached bubble to the maximum volume or reducing the

water drop volume to minimum. Collector adsorption contact angles were measured using both the sessile drop and captive bubble methods. For the sessile drop method, bastnaesite surface was first equilibrated in hydroxamic acid solution (pH=5.2 and pH=9.3) for ~30 minutes, then it was taken out, air dried and ready for contact angle measurement (sessile drop method). For the captive bubble measurement, bastnaesite surface is first equilibrate in hydroxamic acid solution (pH=9.3) for ~30 minutes, then a bubble is released and held at the surface. Eventually, the contact angle is measured.

Four different concentrations of hydroxamic acid solutions were prepared for contact angle measurements, 1×10^{-5} M, 2×10^{-5} M, 5×10^{-5} M, 1×10^{-4} M for both neutral pH and for pH 9.3, at which pH, maximum flotation recovery was found (Pradip, 1981). Then the bastnaesite flat plate sample was soaked in hydroxamate solution for about 30 minutes and the contact angles of bastnaesite surface were measured.

3.2.5 Sum Frequency Vibrational Spectroscopy (SFVS)

As discussed in Chapter 2, SFVS is surface sensitive and can be used to characterize the surface state including adsorbed species. Particularly, SFVS can be used to study surfactant structure and conformation at surfaces or interfaces in the C-H vibrational region (Becraft et al., 2004; Hopkins et al., 2005; Conboy et al., 1996, 1997; Lu et al., 2005). Primary characteristic C-H vibrational bands of the terminal methyl group include CH_3 symmetric stretch (r^+), symmetric CH_3 stretch Fermi resonance (r_{FR}^+), and the asymmetric CH_3 stretch (r^-). For the methylene group, the vibrational bands include CH_2 symmetric stretch (d^+), symmetric CH_2 stretch Fermi resonance (d_{FR}^+), and the asymmetric CH_2 stretch (d^-). The assignments of these C-H vibrational modes in SFVS are achieved by comparison with infrared and Raman spectra of alkanes (MacPhail et al.,

1984; Lambert et al., 2005). Table 3.1 summarizes these assignments. There are some deviations of several wavenumbers in the assignments of these C-H vibration modes in the literature, which is normal considering the difference in resolution and sensitivity of SFVS instruments and the data processing method.

3.2.6 Molecular Dynamics Simulation (MDS)

The MD simulation program DL_POLY_214 (Smith and Forester, 1996) is used for the analysis of bastnaesite surfaces. A simple cubic cell contains the extended simple point charge (SPC/E) for water molecules (Berendsen et al., 1987b) and the rare earth crystals, which was constructed using lattice parameters provided by American Mineralogist Crystal Structure Database (Gruner, 1934; Perdikatsis and Burzlaff, 1981). The system is defined with periodic boundary conditions. The numbers of atoms for the bastnaesite surface with/without chemisorbed hydroxamate for interfacial water analysis and water drop contact angle measurements from MDS are listed in Table 3.2 and Table 3.3, respectively. The intermolecular potential parameters and charge parameters for the hydroxamate collector are listed in Table 3.4 and Table 3.5. The charges for hydroxamate molecules as well as bastnaesite carbon and bastnaesite oxygen were calculated using the Gaussian program. For a water drop interacting with the bastnaesite surface having chemisorbed hydroxamate molecules, three levels of hydroxamate coverage were investigated, 8.3%, 25% and 50%, respectively, with both surfaces of bastnaesite having adsorbed hydroxamate.

The pair potential force field used in the simulations is given as a combination of the Lennard-Jones and the Coulomb electrostatic interactions, and can be expressed as:

Table 3.1 – C-H stretching modes resonant assignments and wavenumbers in SFVS (Data source: Lambert et al., 2005; Conboy et al., 1997; Wang et al., 2008).

Mode	Description	Wavenumber (cm^{-1})	
		In air	In water
r^+	symmetric CH_3 stretch	~2878	~2874
r_{FR}^+	symmetric CH_3 stretch (Fermi resonance)	~2942	~2933
r^-	asymmetric CH_3 stretch	~2966	~2962
d^+	symmetric CH_2 stretch	~2854	~2846
d_{FR}^+	symmetric CH_2 stretch (Fermi resonance)	~2890-2930	~2890-2930
d^-	asymmetric CH_2 stretch	~2915	~2916

Table 3.2 – Number of atoms in the bastnaesite surface for interfacial water analysis with/without hydroxamate adsorption.

Species	Number of atoms
Cerium	384
Fluorine	384
Carbon	384
Oxygen	1152
Hydroxamate (50% coverage)	16

Table 3.3 – Number of atoms in the bastnaesite surface for water drop contact angle with/without hydroxamate adsorption.

Species	Number of atoms
Cerium	1296
Fluorine	1296
Carbon	1296
Oxygen	3888
8.3% hydroxamate coverage	18
25% hydroxamate coverage	54
50% hydroxamate coverage	108

Table 3.4 – Potential parameters for water interactions at bastnaesite surface with adsorbed hydroxamate.

Species	Charge [e]	ε [Kcal/mol]	σ [Å]	Reference
Cerium	3	0.007	3.9618	Assigned
Fluorine	-1	0.1793	3.117	(Lee and Rasaiah, 1996)
Bastnaesite carbon	0.883, calculated from Gaussian	0.0403	3.1074	(Austen et al., 2005; Rohl et al., 2003)
Bastnaesite oxygen	-0.961, calculated from Gaussian	0.1554	3.1659	(Berendsen et al., 1987a)
Hydroxamate carbon		1171342	667.5166	(Mayo et al., 1990)
Hydroxamate oxygen		232116	298.084	(Mayo et al., 1990)
Hydroxamate nitrogen		450301.5	373.381	(Mayo et al., 1990)
Hydroxamate hydrogen		0	0	(Mayo et al., 1990)
Water oxygen		0.1554	3.1659	(Berendsen et al., 1987a)
Water hydrogen		0	0	(Berendsen et al., 1987a)

Table 3.5 – Charge parameters for hydroxamate.

Species	Charge
C	-0.45043
C	-0.2981
C	-0.28879
C	-0.2943
C	-0.29497
C	-0.30028
C	-0.29584
C	-0.40249
C	0.755029
O	-0.65833
N	-0.50826
O	-0.54483
H	0.149759
H	0.152198
H	0.149315
H	0.148249
H	0.148795
H	0.148491
H	0.147458
H	0.146901
H	0.148162
H	0.15521
H	0.151744
H	0.147755
H	0.152157
H	0.204966
H	0.169449
H	0.179634
H	0.212635
H	0.397863
H	0.470816

$$U_{pair} = \sum_i \sum_j \left(4\varepsilon \left[\left(\frac{\sigma_{ij}}{r_{ij}} \right)^{12} - \left(\frac{\sigma_{ij}}{r_{ij}} \right)^{6} \right] + \frac{q_i q_i}{r_{ij}} \right) \quad (3\text{-}3)$$

Here ε is the energy parameter, σ is the size parameter, q is the charge, and r is the distance between species i and j. The potential parameters of pairs were calculated by applying the Lorentz-Berthelot mixing rules:

$$\varepsilon_{ij} = \sqrt{\varepsilon_i \varepsilon_j} \quad (3\text{-}4)$$

$$\sigma_{ij} = \frac{\sigma_i + \sigma_j}{2} \quad (3\text{-}5)$$

Initially, the bastnaesite crystal is simulated in a NPT (moles (N), pressure (P) and temperature (T) are conserved) assemble with the pressure fixed at 0.1 Mpa and the temperature at 300K for 100ps. After adding SPC-E water into the system, the simulation is performed in a NVT (moles (N), volume (V) and temperature (T) are conserved) assemble using Hoover's thermostat (Melchionna et al., 1993). The leap-frog method with a time step of 1fs is used to integrate the particle motion. The Ewald sum is used to account for the electrostatic interactions. A final simulation time of 1ns (nanosecond) ($1x10^6$ steps) after a 500ps (picosecond) equilibration period was performed. The water density profile was analyzed based on the equilibrium condition with 1ns simulation after the equilibration period. The residence time profile was a dynamic analysis of a 200ps simulation after the equilibration period.

3.3 Results and Discussion

As discussed earlier, bastnaesite is one of the principle resources for rare earth elements. Thus, investigation on the surface chemistry features including the solution

chemistry and stability diagram of bastnaesite, wetting characteristics as well as collector adsorption at bastnaesite surface is important.

3.3.1 Solution Chemistry Solubility and Stability Diagrams

As mentioned in the Introduction, bastnaesite, a rare earth fluorocarbonate, is a semisoluble salt mineral, with the formula of (Ce, La)FCO_3. The recovery of bastnaesite has traditionally been achieved by flotation (Herrera-Urbina et al. 2013). The main gangue minerals in the Mountain Pass, CA (California) bastnaesite ore are calcite, barite, celestite, etc (Herrera-Urbina et al., 2013; Fuerstenau et al., 1992; Pradip, 1981), which belong to the alkaline earth semisoluble salt minerals. Review of the electrokinetic behavior of bastnaesite in Chapter 1 (Table 1.10) reveals that the reported point of zero charge for bastnaesite has some deviation due to different samples, experimental procedure, etc. As expected, these electrophoretic mobility studies of bastnaesite in aqueous solutions also reveal that pH plays a significant role in the electrokinetic behavior of bastnaesite. The zeta potential of bastnaesite particles become more positive at low pH, while the zeta potential is more negative when the pH increases in alkaline solution. Little information is known about the surface chemistry of bastnaesite in aqueous solution including the solution chemistry and stability of bastnaesite.

Herrera-Urbina et al. performed theoretical computations of mineral-solution equilibria based on mass balance equations for different conditions and obtained the solubility diagram of the different solid phases as well as the speciation distribution diagram for bastnaesite in aqueous solution from pH 3 to 12 in a closed system (Herrera-Urbina et al., 2013). It was found that for a 0.05%wt bastnaesite suspension, bastnaesite is the only solid phase in the pH range from 5.75 to 8.55. Bastnaeiste coexists with

CeF_3(s) from pH 5.22 to pH 5.74 and with $Ce(OH)_3$(s) from pH 8.56 to pH 10.12. Cerium fluoride and cerium hydroxide are the only solid phases below pH 5.2 and above pH 10.2, respectively. Besides pH, other factors including mineral solubility, carbonate hydrolysis, rare earth metal ions hydrolysis and complex formation as well as precipitation of new solid phases will also affect the electrokinetics of bastnaesite particles. Except for the bastnaesite crystal lattice ions, Ce^{3+}, F^- and CO_3^{2-}, which are generally assumed to be the potential determining ions, other ions including $CeOH_2^+$, $Ce(OH)_2^+$, $CeCO_3^+$, HCO_3^- also seem to influence the electrophoretic mobility of bastnaesite, due to their predominance in solution (Herrera-Urbina et al., 2013).

Pradip (1981) also studied the electrophoretic mobility of bastnaesite and found that it behaves more like carbonate minerals. The effect of F^- and CO_3^{2-} on the electrophoretic mobility of bastnaesite was studied and it was found that CO_3^{2-} is a potential determining ion, while F^- does not have a very significant effect on the sign of the zeta potential of bastnaesite. The finding that the electrophoretic mobility of bastnaesite is strongly affected by pH seems to suggest that both the hydrogen and the hydroxide ions may also be the potential determining ions (Herrera-Urbina et al., 2013). However, some other researchers (Siffert and Fimbel, 1984; Moulin and Roques, 2003; Eriksson et al., 2007; Sondi et al., 2009) have claimed that H^+ and OH^- are not the potential-determining ions, and have no direct influence on the electrical surface properties. They are of secondary importance and influence bastnaesite surface charge through regulation of the carbonate ion in solution (Siffert and Fimbel, 1984; Moulin and Roques, 2003; Eriksson et al., 2007; Sondi et al., 2009). The bastnaesite crystal lattice cerium ion can form hydroxyl complexes through hydrolysis, as well as fluoride and carbonate complexes in the

aqueous phase or even precipitate as cerium fluoride and cerium hydroxide depending on pH. Fluoride and carbonate ions can also undergo hydrolysis and form complexes (Herrera-Urbina et al., 2013). All the above mentioned results suggest that a better understanding of the surface chemistry of bastnaesite and the solution chemistry of the aqueous phase must be achieved.

Although Herrera-Urbina et al. studied the speciation and solubility diagrams of bastnaesite – H_2O system, the effect of CO_2 pressure has not been considered. In this section of the dissertation, the effect of CO_2 pressure on the solution chemistry of bastnaesite – H_2O system is considered and investigated. The solubility as well as the speciation distribution diagrams were obtained using Stabcal software (W32-STABCAL). The Gibbs free energies for each species in the system were calculated based on the equilibrium constants for the mass balance equations reported by Herrera-Urbina et al. (2013). The thermodynamic data applied during Stabcal calculation are shown in Table 3.6. The data written in italics mean dG (Gibbs free energy) of master species are taken from the LLnL database in Stabcal software in order to convert from logK (K is the equilibrium constant for the equation) to dGs for the rest of the species.

Figures 3.2 to 3.7 (y axis shows total dissolved cerium) show bastnaesite (0.1% wt)-H_2O system stability diagram as a function of pH closed to the atmosphere and open with different CO_2 pressures. In a closed system (Figure 3.2), the solubility diagram is similar to that reported in the literature (Herrera-Urbina et al., 2013). Bastnaesite is the only phase in the pH range from pH 5.7 to pH 8.5. For pH ranges of pH 5 to 5.7 and pH 8.5 to 10.4, bastnaesite coexists with cerium fluoride and cerium hydroxide, respectively. For pH values below pH 5, cerium fluoride is the only solid phase and when the pH value is

Table 3.6 – Thermodynamic data applied for Stabcal calculation (A-aqueous, S-solid, L-liquid) (Data source: Herrera-Urbina et al., 2013).

Species	dG(kcal)
Ce^{3+} (A)	*-160.612*
$CeOH^{2+}$ (A)	-206.237
$Ce(OH)_2^{+}$ (A)	-251.725
$Ce(OH)_3$ (A)	-295.167
$Ce(OH)_4^{-}$ (A)	-335.471
$Ce_3(OH)_5^{4+}$ (A)	-720.464
CeF^{2+} (A)	-232.510
CeF_2^{+}	-303.835
$CeCO_3^{+}$	-297.076
$Ce(CO_3)_2^{-}$ (A)	-429.542
$CeHCO_3^{2+}$ (A)	-304.183
$CeFCO_3$ (S)	-375.222
$Ce(OH)_3$ (S)	-303.216
CeF_3 0 (S)	-381.104
CO_3^{2-} (A)	*-126.150*
HCO_3^{-} (A)	-140.270
H_2CO_3 (A)	-148.933
CO_2 (G)	-94.250
F^{-} (A)	*-66.632*
HF (A)	-70.965
HF_2^{-} (A)	-138.403
H^{+} (A)	*0*
H_2O (L)	*-56.675*
OH^{-} (A)	*-37.582*

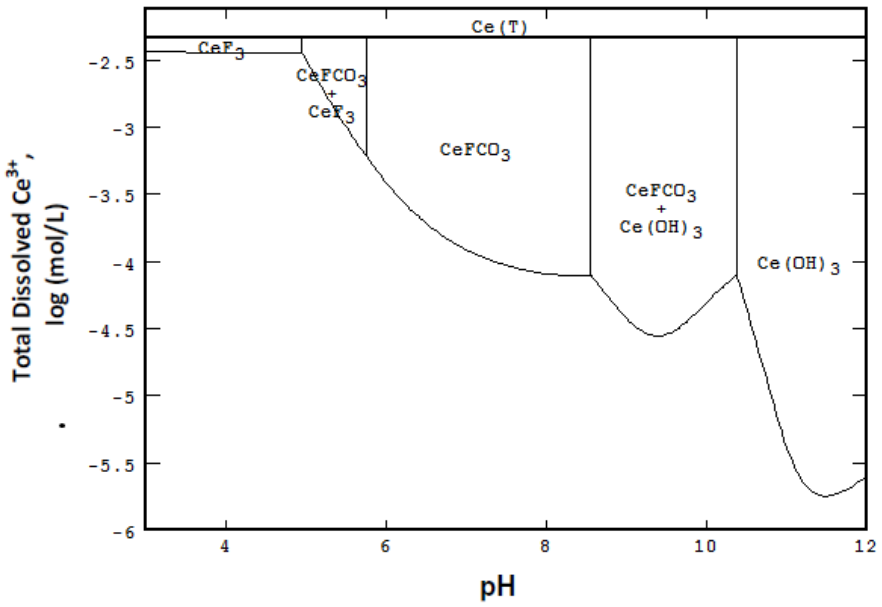

Figure 3.2 – Bastnaesite stability diagram as a function of pH (closed system).

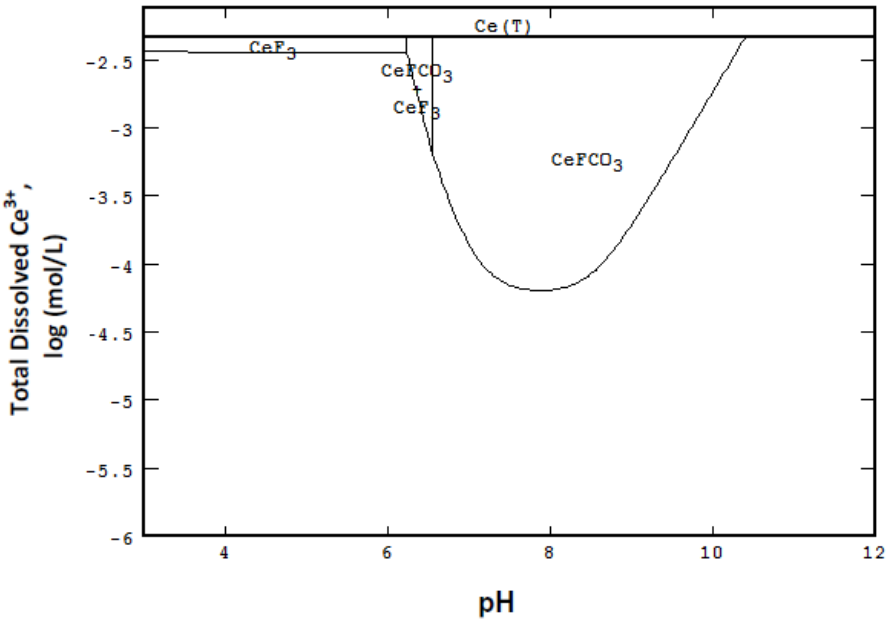

Figure 3.3 – Bastnaesite stability diagram as a function of pH with $10^{-3.5}$ atm CO_2 gas.

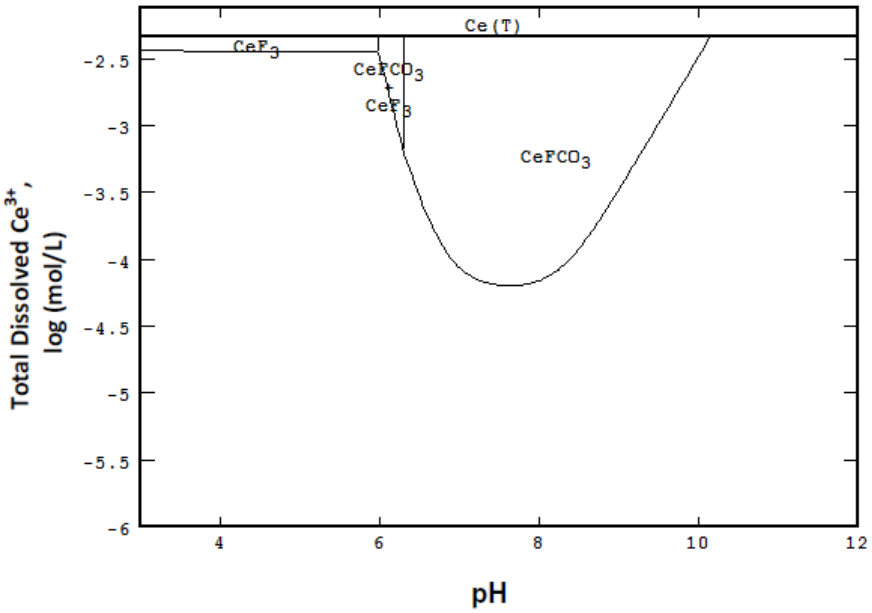

Figure 3.4 – Bastnaesite stability diagram as a function of pH with 0.001 atm CO_2 gas.

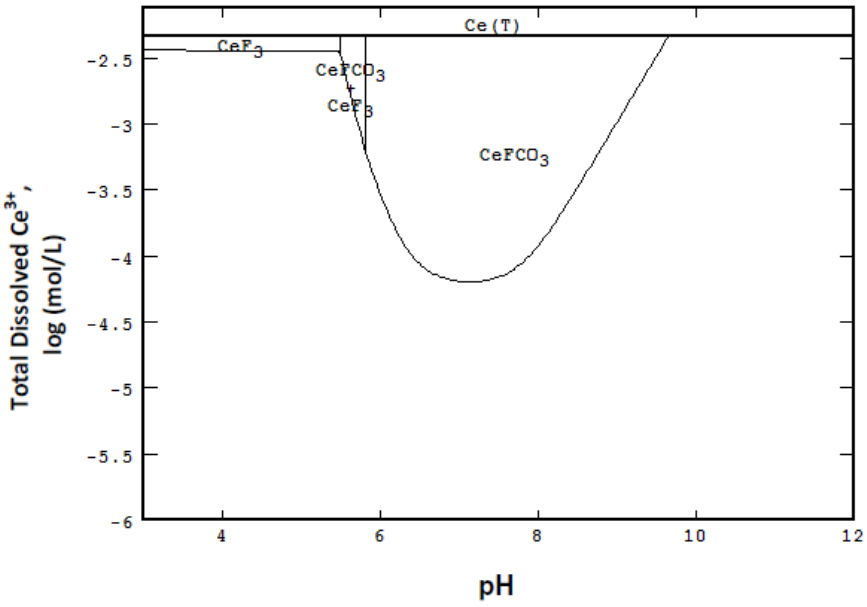

Figure 3.5 - Bastnaesite stability diagram as a function of pH with 0.01 atm CO_2 gas.

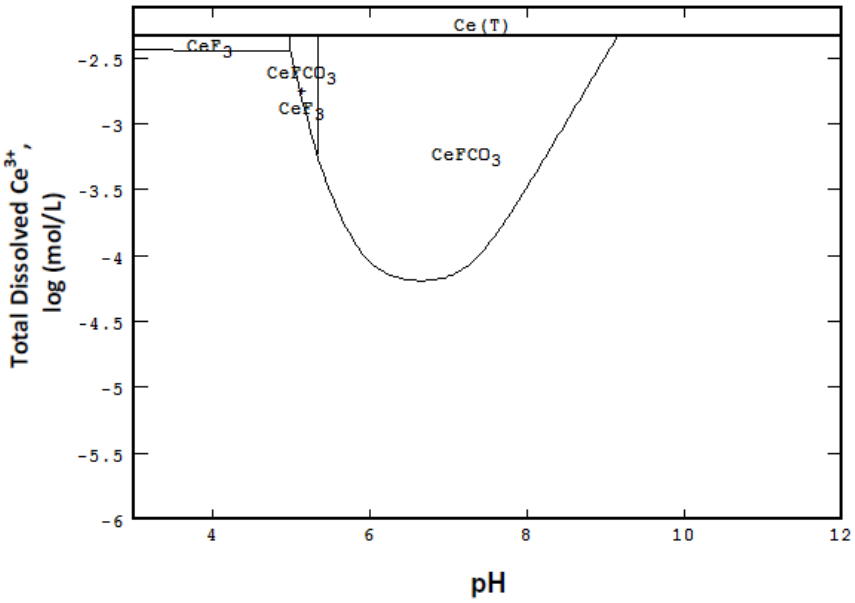

Figure 3.6 – Bastnaesite stability diagram as a function of pH with 0.1 atm CO_2 gas.

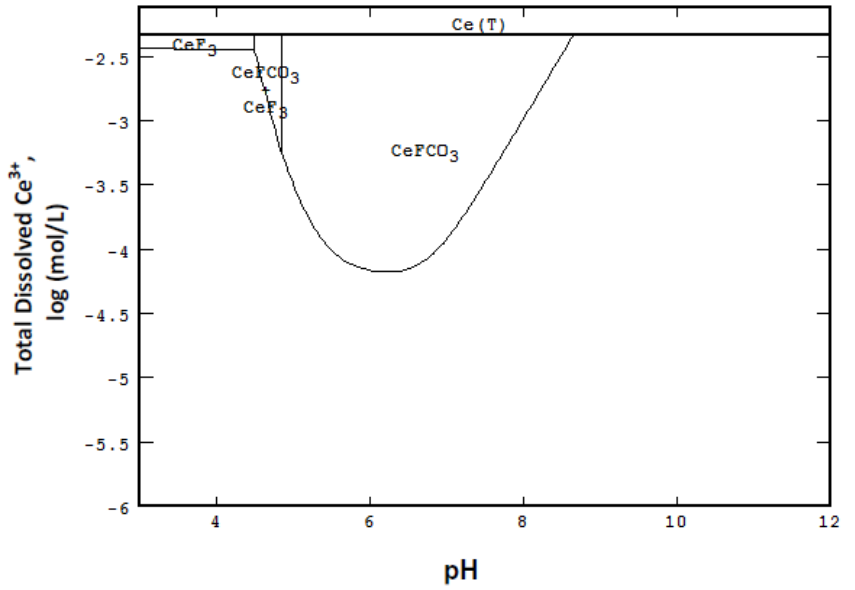

Figure 3.7 – Bastnaesite stability diagram as a function of pH with 1 atm CO_2.

above pH 10.4, cerium hydroxide is the only solid phase in the system. The reason for the transformation of bastnaesite to cerium fluoride at low pH values (acidic pH) and to cerium hydroxide to high pH values (basic pH) can be represented by the following reactions shown in equations 3-6 and 3-7:

$$3CeFCO_3 + 3H^+ \longleftrightarrow CeF_3 + 2Ce^{3+} + 3HCO_3^- \quad (3\text{-}6)$$

$$CeFCO_3 + 3OH^- \longleftrightarrow Ce(OH)_3 + F^- + CO_3^{2-} \quad (3\text{-}7)$$

However, when CO_2 is present in the system the solubility diagrams are quite different (Figures 3.3 to 3.7). Cerium hydroxide stability disappears for all CO_2 pressures and bastnaesite becomes the only stable phase at high pH values. The cerium hydroxide reacts with CO_2 and dissolves forming carbonate anions as shown in equation 3-8.

$$2Ce(OH)_3 + 2CO_2 + OH^- \longleftrightarrow Ce(CO_3)_2^- + 2H_2O \quad (3\text{-}8)$$

It can also be noted that when CO_2 pressure increases, Figure 3.3 to 3.7, the stability field for bastnaesite shifts to the left side of the stability diagram, that is, the more acidic pH side, the bastnaesite becomes more stable at low pH. The pH range of the cerium fluoride field is compressed simultaneously. This can be explained from equations 3-6 and 3-7 together with equations 3-9 and 3-10. When CO_2 is present in the system, the following reactions occur producing HCO_3^- and CO_3^{2-} species.

$$2CO_2 + H_2O \longleftrightarrow H_2CO_3 \quad (3\text{-}9)$$

$$H_2CO_3 \longleftrightarrow HCO_3^- + H^+ \quad (3\text{-}10)$$

$$HCO_3^- \longleftrightarrow CO_3^{2-} + H^+ \qquad (3\text{-}11)$$

When the CO_2 pressure increases, the concentration of HCO_3^- will be increased and equations 3-6 and 3-7 will be favored for CeF_3 species. At low pH values, the transformation reaction from bastnaesite to cerium fluoride can be expressed by equation 3-6, from which it can be seen that an increase in HCO_3^- concentration will push the reaction to the bastnaesite species. Consequently, the pH range of stable cerium fluoride is compressed. When the pH value is lower, below about pH 5, the concentration of H^+ is high. As a result, bastnaesite can be transformed to cerium fluoride as described by equation 3-6. At high pH values, increasing CO_2 pressure favors equation 3-8 to aqueous $Ce(CO_3)_2^-$ species. Thus more bastnaesite will be dissolved into the solution and the corresponding stability field is shifted to the low pH side of the stability diagram.

Figures 3.8 and 3.9 show cerium and fluoride species speciation-distribution diagrams for the bastnaesite (0.1% wt)-H_2O system with $10^{-3.5}$ atm CO_2. It can be seen that cerium ions form complexes with fluoride and carbonate ions, which is consistent with the equations shown above. These ions may play a role in the surface chemistry of bastnaesite including the surface charge of bastnaesite, which will be discussed in section 3.3.2.

3.3.2 Zeta Potential of Bastnaesite Measured by Microelectrophoresis

The zeta potential of bastnaesite particles is presented in Figure 3.10 as a function of pH. The red line shows the microelectrophoresis result for this dissertation and the black line is the result from the study conducted by Li et al. (1967). It can be noted that the PZC of bastnaesite was found to be about pH= 8.1 in both cases. These results agree with

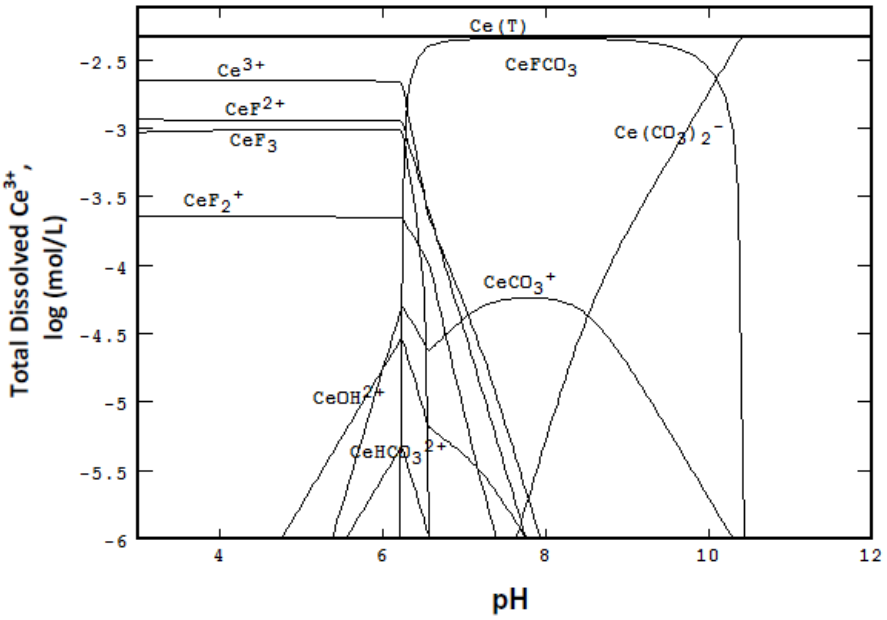

Figure 3.8 – Aqueous concentrations of cerium species for bastnaesite with $10^{-3.5}$ atm CO_2 gas.

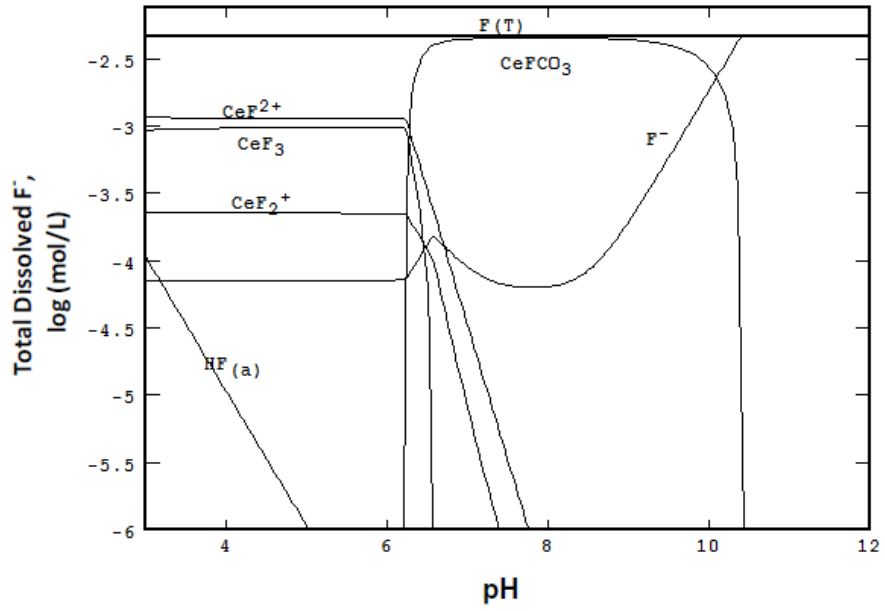

Figure 3.9 – Aqueous concentrations of fluoride species for bastnaesite with $10^{-3.5}$ atm CO_2 gas.

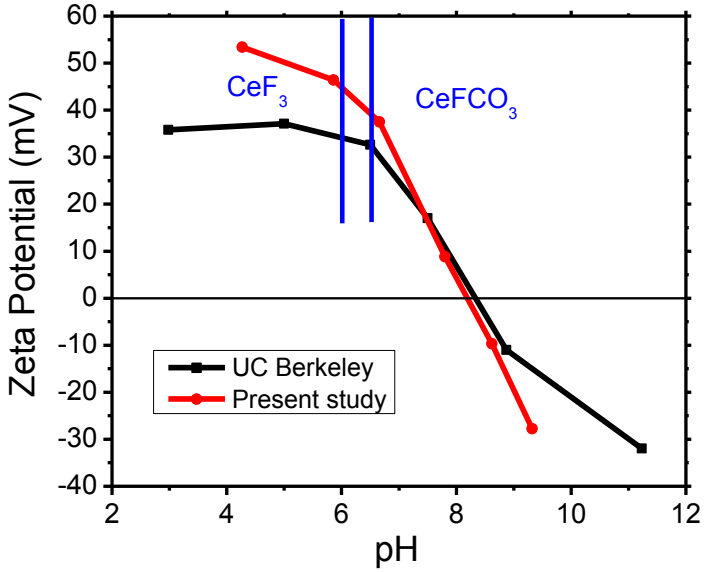

Figure 3.10 - Zeta potential of bastnaesite (Zagi Mountain, Pakistan) obtained by microelectrophoresis (ionic strength was not controlled).

the results of Ren et al. (1997; 2000). There is some deviation between these two data sets at low and high pH values, which might be due to different bastnaesite samples, experimental procedures, etc. In this dissertation research, the bastnaesite sample is from Zagi Mountain, Pakistan, while in the Li et al. research, they used synthetic bastnaesite, which may account for different zeta potentials at certain pH values.

Based on the previous discussion of the bastnaesite solution chemistry for systems open to the atmosphere (Figure 3.3), it can be seen that below pH 6, cerium fluoride is the only stable solid phase and above pH 6.6, bastnaesite is the only solid phase in the system. There is a small intersection area between pH 6 to pH 6.6, where both cerium fluoride and bastnaesite are stable. Thus, below pH 6, the electrokinetic characteristics shown in Figure 3.10 might represent the surface charge of cerium fluoride and above pH 6.6, it might represent the surface charge features of the bastnaesite. Between pH 6 to 6.6, the zeta potential results might represent a transition state that would include both surfaces.

From Figure 3.10, it can be seen that bastnaesite is positively charged below about pH 8.1, which is the point of zero charge (PZC), and negatively charged above the PZC. From Figures 3.8 and 3.9, it can be seen that below pH 8, the dominating aqueous species in the solution are almost all cations, including Ce^{3+}, CeF^{2+}, CeF_2^{+}, $CeOH^{2+}$, $CeHCO_3^{2+}$, $CeOH^{2+}$, $CeCO_3^{+}$. Fluoride ion (F^-) is the only anion. These cations might adsorb onto the surface of the mineral below the PZC and give rise to a positive surface charge. When pH is above the PZC, anions including F^- and $Ce(CO_3)_2^-$ might act as the potential determining ions and result in a negative charge on the surface. The finding that the zeta potential of bastnaesite surface is affected by pH suggests that hydrogen and hydroxide ions may also determine the electrokinetics of bastnaesite. As discussed earlier, some

researchers consider that H^+ influences the bastnaesite surface charge through regulation of the carbonate ion in solution (Siffert and Fimbel, 1984; Moulin and Roques, 2003; Eriksson, Merta et al., 2007; Sondi et al., 2009).

3.3.3 Hydroxamate Adsorption Isotherm for Bastnaesite

3.3.3.1 Solubility and Solution Chemistry Considerations of Octyl Hydroxamic Acid

The pKa of hydroxamic acids has been reported to be about pH 9 (Pradip, 1981). Since most of the dissertation research is done at pH 9.3, it is expected that about 33% of hydroxamic acid will be presented in the acid form and about 67% will be presented as the hydroxamic anion.

Equations 3-12 and 3-13 show the equilibrium of octyl hydroxamic acid dissociation in solution and the acid dissociation constant. OHA can dissociate into anion and H^+ when it is in aqueous phase. However, when the solubility limit is exceeded, OHA colloids are also present in the solution and cannot dissociate. Consequently it is important to determine the solubility of hydroxamate.

$$CH_3(CH_2)_6\,CONHOH \rightleftharpoons CH_3(CH_2)_6\,CONHO^- + H^+ \qquad (3\text{-}12)$$

$$K_a = \frac{[CH_3(CH_2)_6CONHO^-][H^+]}{CH_3(CH_2)_6CONHOH} \qquad (3\text{-}13)$$

In this dissertation research, DSL measurements were conducted to examine whether there are particles present in the solution at certain concentrations of octyl hydroxamic acid (OHA). Two different concentrations of octyl hydroxamic acid (OHA) solutions and DI water, which acts as the reference, were measured using DSL technique at pH 9.3. Results show that there are particles with a size ranging from about 0 to 700

nm existing for both OHA solutions with concentrations of 1.89×10^{-3} M and 3.77×10^{-3} M, which suggests that both solutions are saturated with respect to hydroxamate at such concentrations. Thus, it can be concluded that for the OHA concentrations examined, there are particles present in the solution. This indicates that at these two concentrations the solubility of OHA has already been exceeded. Further study needs to be conducted to detect the exact solubility in the future.

Adsorption experiments in this dissertation research were done at concentrations below 1×10^{-3} M OHA. Previous research at UC Berkeley (Pradip, 1981) considered concentrations above 1×10^{-3} M OHA, where surface precipitation occurs.

3.3.3.2 Hydroxamate Adsorption Isotherm Determination

Hydroxamate adsorption at high concentrations ($>10^{-4}$ M) has been studied by Pradip (1981) and multilayer adsorption was obtained at such concentrations. In this dissertation research, low concentrations of hydroxamate adsorption at the bastnaesite surface are investigated and the nature of the adsorbed state examined. The adsorption density of octyl hydroxamate at a bastnaesite suface was measured at low concentrations using high sensitivity TOC analysis (total organic carbon analysis).

Figure 3.11 shows the adsorption isotherm of octyl hydroxamic acid (OHA) at bastnaesite surface including both low (present study) and high concentrations of hydroxamate (Pradip, 1981). The hydroxamate group was calculated to have a cross sectional area of 20.5 $Å^2$, and the monolayer adsorption density is calculated to be 8.1×10^{-6} mol/m^2. The blue horizontal line indicates vertical monolayer coverage limited by the OHA cross sectional area. From Figure 3.11 it can be seen that the adsorption

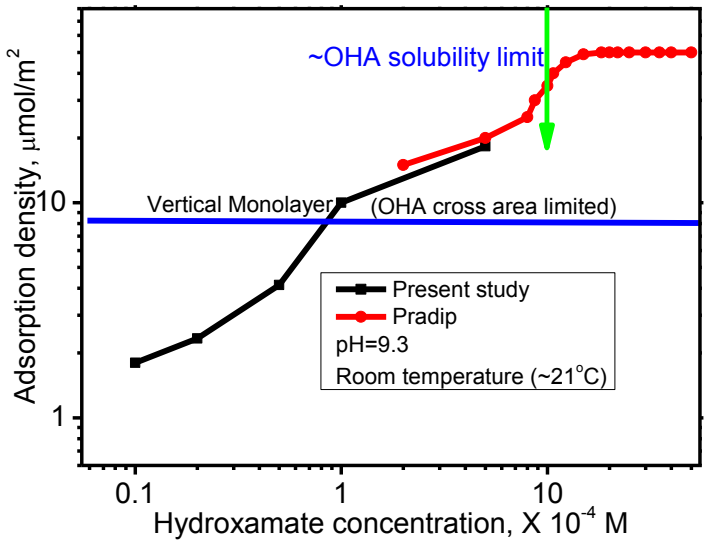

Figure 3.11 – Hydroxamate adsorption isotherm at bastnaesite surface (pH=9.3).

isotherm at low concentrations indicates an increase in adsorption density when the hydroxamate concentration increases, which is consistent with contact angle measurements to be presented in the next section. Monolayer adsorption occurs at about 1 × 10^{-4} M considering hydroxamate cross sectional area limitation. Below this concentration, only submonolayer coverage is achieved and the adsorption is expected to be a chemisorption process. In other words, the bastnaesite surface is not fully covered by hydroxamate molecules and as a result, a portion of the surface is still exposed to the aqueous solution, and such surface regions can interact with water molecules. Bastnaesite is naturally hydrophilic as discussed in the next section. When bastnaesite surface is not fully covered by hydroxamate, the surface only exhibits a moderate hydrophobicity and the exposed mineral surface accounts for such a characteristic and the contact angle is expected to increase with increasing hydroxamate adsorption at least up to monolayer

coverage at an equilibrium concentration of 1×10^{-4} M OHA.

Below monolayer coverage, the adsorption of hydroxamate at the bastnaesite surface is expected to be a chemisorption process. The hydroxamate collector can react with the surface as well as with RE cations from lattice sites (Pradip and Fuerstenau, 1983). As discussed in Chapter 1, the reaction is a chelating reaction, which is accomplished through replacement of the hydrogen atom of the hydroxyamide group by a metal cation and ring closure by the carbonyl oxygen atom (Pradip and Fuerstenau, 1983), as shown in equation 3-14. The adsorption stability below monolayer coverage has been examined by washing with acetone, alcohol and DI water, and the bastnaesite surface still maintained its hydrophobic state. Direct evidence for chemisorption has not been established.

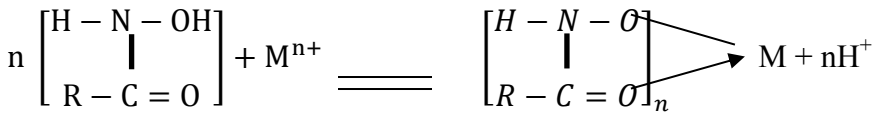

(3-14)

According to equation 3-14, one cerium (or other rare earth cation, e.g. La^{3+}) ion can interact with as many as three hydroxamate molecules. However, as the adsorption is limited by hydroxamate cross area, not every cerium atom at the surface can accommodate three hydroxamate molecules. As discussed in Chapter 1, the cerium surface site density is calculated to be 4.74 μmol/m^2. Thus a vertical monolayer hydroxamate adsorption density of about 8.1 μ mol/m^2 corresponds to a ratio of hydroxamate to cerium of approximately 2 : 1 (1.7 :1) . Based on this calculation, it is possible that each cerium at the surface can react with two hydroxamate molecules. Still, it might also be possible that some cerium atoms react with three hydroxamate molecules, and some others react with one or two hydroxamate molecules until full monolayer

adsorption is achieved.

Possible reactions in solution below monolayer coverage are discussed. pH 9.3 is close to the reported pKa value of hydroxamate (Pradip, 1981). At such pH, it is expected that both anionic and neutral hydroxamate species are present in the solution. As a result, the rare earth cations can react with both hydroxamate species. See equation 3-15. Reaction with hydroxamate anions (does not release H^+) and with other rare earth elements can be written in similar fashion.

From equation 3-15, it can be seen that cerium species reacting with neutral hydroxamate molecules release hydrogen ions in the solution and consequently, a pH decrease might be expected due to adsorption. This is verified in our adsorption experiments: a pH decrease was observed after adsorption, confirming the role of undissociated hydroxamate species in the adsorption process. Such pH decrease has also been observed by other researchers. Pradip (1981) observed a notable pH decrease at higher temperatures during adsorption for the bastnaesite\hydroxamate system. Raghavan and Fuerstenau (1975) also observed a pH decrease for the hematite/hydroxamate system after adsorption.

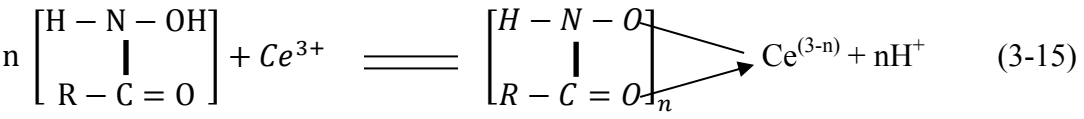

(3-15)

Above monolayer coverage, multilayer adsorption commences, which is a physisorption process. The green arrow indicates estimated hydroxamate solubility limitation at about 1×10^{-3} M. Above the monolayer coverage, multilayer physisorption of hydroxamate at the bastnaesite surface may happen through hydrophobic interaction of hydrocarbon chains or hydrogen bonding, as shown in equations 3-16 and 3-17 (Pradip

and Fuerstenau, 1983). This acts as the driving force for this stage of adsorption. Besides, at pH 9.3, which is close to the mostly reported pKa values of hydroxamate (Pradip, 1981), both dissociated hydroxamate anions as well as neutral hydroxamate molecules exist in the system. From bastnaesite speciation distribution diagrams (Figures 3.8 and 3.9), aqueous $Ce(CO_3)_2^-$ and $CeCO_3^+$ are available in the system at pH 9.3. At high OHA concentrations, an excess of hydroxamate is present in the solution. Thus, hydroxamate (anions or neutral molecules) may react with aqueous $Ce(CO_3)_2^-$ and $CeCO_3^+$ ions through equations 3-18 and 3-19 and form cerium (or other RE cations) hydroxamate complexes. Consequently, surface precipitation anionic and neutral hydroxamate species as well as cerium hydroxamate complexes may happen. When the concentration of hydroxamate solution exceeds its solubility limit, the adsorption might include the insoluble OHA collector colloid.

(3-16)

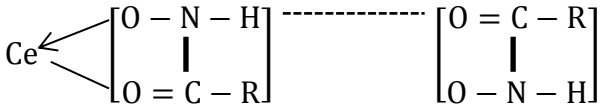

(3-17)

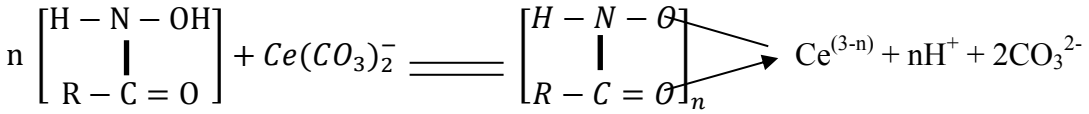

(3-18)

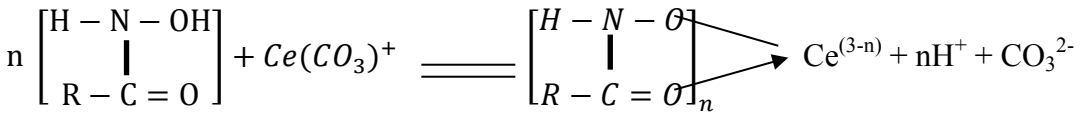

(3-19)

When adsorption of hydroxamate at the bastnaesite surface exceeds monolayer coverage, at relatively high concentrations of hydroxamate, particle aggregation also occurs due to an excess concentration of the hydroxamate collector. Figure 3.12 shows the aggregation structure of bastnaesite obtained from optical microscopy (STEMI SV8 microscope, 10X) at 5 $\times 10^{-4}$ M hydroxamate (OHA) concentration. From Figure 3.12, it can be seen that sheet like structures are formed due to an excess amount of hydroxamate in the solution. Hydroxamate species can interact with each other through hydrocarbon chains by hydrophobic interaction to promote aggregation.

3.3.4 Contact Angle of Bastnaesite at Low Levels of Hydroxamate Adsorption

In order to investigate the hydrophobic surface state of bastnaesite surface with and without hydroxamate adsorption, the wetting characteristics of bastnaesite were evaluated by both contact angle measurement and MD simulations in the absence of collector. Water contact angle measurements at the bastnaesite surface (Zagi Mountain, Pakistan) were made using both sessile drop and captive bubble methods. First, the bastnaesite sample was polished and the surface roughness was measured using atomic force microscope (AFM). The surface roughness listed here is the root-mean-square roughness R_q, which is the root-mean-square deviation from the mean elevation and was found to be 26.4 nm. The bastnaesite surface was cleaned by rinsing with acetone, methanol, and copious amounts of deionized water, followed by drying with high-purity nitrogen. The samples were then polished with 0.05μm gamma alumina powders on a polishing cloth and again dried with high-purity nitrogen gas. The equilibrium contact angle for bastnaesite without collector adsorption is close to zero as shown in Table 3.7. In addition,

Figure 3.12 – Aggregation of bastnaesite particles at 5 $\times 10^{-4}$ M hydroxamate (initial particle size -45μm).

Table 3.7 – Contact angle results of bastnaesite surface by experiments and MD simulations.

Surface	Method	Contact angle
Bastnaesite (100)	MDS	0^o
Bastnaesite (Zagi Mountain, Pakistan),pH=5.2	Captive bubble	0^o
	Sessile drop	9^o

the advancing and receding contact angles at the bastnaesite surface were also measured using the captive bubble method and both were found to be zero.

To understand the interaction of a water drop with the bastnaesite surface at the molecular level, our research group also did the MDS for a water drop at a cerium-bastnaesite surface. The water drop was found to spread and completely wet the bastnaesite surface, as shown in Figure 3.13. The simulation results generally agree with the experimental measurements presented in Table 3.7 and confirm the hydrophilic characteristic of the bastnaesite surface. More discussions of MDS results are given in section 3.3.7.

Contact angle measurements were then conducted for the bastnaesite surface with adsorbed hydroxamate at low levels (below monolayer coverage) by sessile drop and captive bubble methods. The equilibrium contact angle (intermediate contact angle) was measured for all cases of attachment. In addition, advancing and receding contact angles were also measured. The results are shown in Tables 3.8 to 3.10. Figure 3.14 summarizes the intermediate contact angle results for different experimental conditions using both sessile drop and captive bubble methods. From Figure 3.14, it can be noticed that the contact angle increases with an increase in hydroxamate concentration and corresponding adsorption density, which indicates an increase in the hydrophobicity of bastnaesite surface. Comparing the contact angle results of pH ~5.2 (neutral pH) (blue curve) and pH 9.3 (green curve), a moderate increase was observed, suggesting increased hydrophobicity of bastnaesite surface at higher pH, which is consistent with the observation of maximum recovery in flotation tests (Pradip, 1981). Investigation of the effect of ionic strength on contact angle suggests that the addition of 10mM KCl

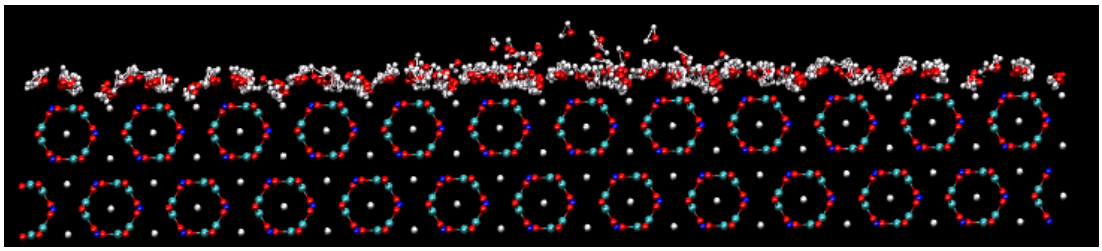

Figure 3.13 - MDS snapshot of a water drop that has spread at the cerium-bastnaesite (100) surface. Red: oxygen; Blue: cerium; Cyan: carbon; White: Fluorine.

Table 3.8 - Contact angle of bastnaesite as a function of hydroxamic acid concentration and pH (sessile drop).

Hydroxamic acid concentration (mol/L)	Intermediate contact angle (θ, degrees)		Advancing contact angle (degrees)		Receding contact angle (degrees)		Hysteresis	
pH	~5.2	~9.3	~5.2	~9.3	~5.2	~9.3	~5.2	~9.3
1×10^{-5}	20°	28°	30°	41°	14°	16°	16°	25°
2×10^{-5}	35.5°	58°	39°	73°	12°	27°	27°	46°
5×10^{-5}	56°	71°	73°	82°	30°	37°	43°	45°
1×10^{-4}	74°	80°	80°	85°	34°	40°	46°	45°

Table 3.9 - Contact angle of bastnaesite as a function of hydroxamic acid concentration (captive bubble, pH=9.3).

Hydroxamic acid concentration (mol/L)	Intermediate contact angle (θ, degrees)	Advancing contact angle (degrees)	Receding contact angle (degrees)	Hysteresis
1×10^{-5}	20°	54	14°	40°
2×10^{-5}	40°	80	38	42°
5×10^{-5}	68°	108°	67	41°
1×10^{-4}	71°	95°	65	30°

Table 3.10 - Contact angle of bastnaesite as a function of hydroxamic acid concentration (captive bubble, 10mM KCl background, pH=9.3).

Hydroxamic acid concentration (mol/L)	Intermediate contact angle (θ, degrees)	Advancing contact angle (degrees)	Receding contact angle (degrees)	Hysteresis
1×10^{-5}	13	33	10°	23°
2×10^{-5}	32.5	55°	26°	29°
5×10^{-5}	67	86°	65°	21°
1×10^{-4}	74.5	95°	66°	29°

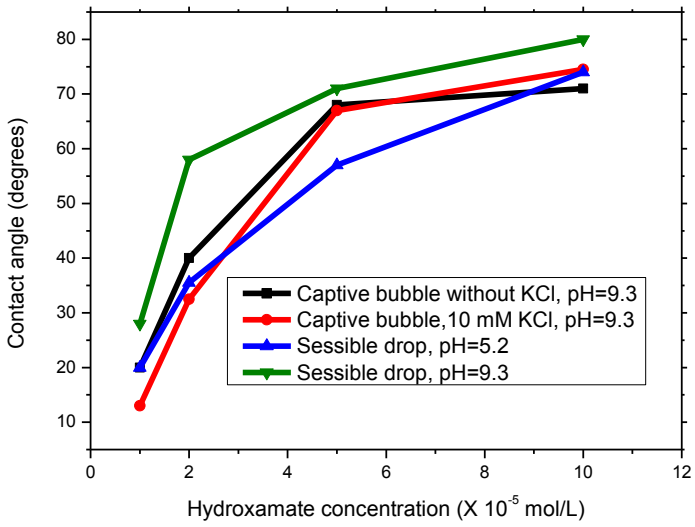

Figure 3.14 - Contact angle of bastnaesite as a function of hydroxamic acid concentration at different pH with/without background solution.

background electrolyte for hydroxamate solution does not influence bastnaesite hydrophobicity significantly.

As mentioned earlier, the difference between advancing and receding contact angles observation of maximum recovery in flotation tests (Pradip, 1981). Investigation of the effect of ionic strength on contact angle suggests that the addition of 10mM KCl background electrolyte for hydroxamate solution does not influence bastnaesite hydrophobicity significantly.

As mentioned earlier, the difference between advancing and receding contact angles is defined as contact angle hysteresis, the reason for the difference between advancing and receding contact angles has been attributed to surface roughness and heterogeneity, metastable surface energy states, etc. (Lam et al., 2001; Lam et al., 2002; Drelich et al., 1996). The contact angle hysteresis results calculated and shown in Table 3.8 to 3.10 are about 20^o to 40^o, which is relatively large. The reason might be due to incomplete coverage and a heterogeneous surface state leading to a relatively larger contact angle hysteresis. Differences in experimental methods and conditions may lead to some deviations in the contact angle hysteresis as indicated in Tables 3.8 to 3.10.

Figure 3.15 combines the adsorption isotherm at low concentrations of hydroxamate with the contact angle results. It can be noted that the contact angle increases with an increase in the adsorption density as expected. For both the contact angle and adsorption density results, it appears that full monolayer coverage has been achieved (contact angle = $70\text{-}80^o$, apparent adsorption density for monolayer coverage =8.1 $\mu mol/m^2$). Above this point multilayer adsorption begins.

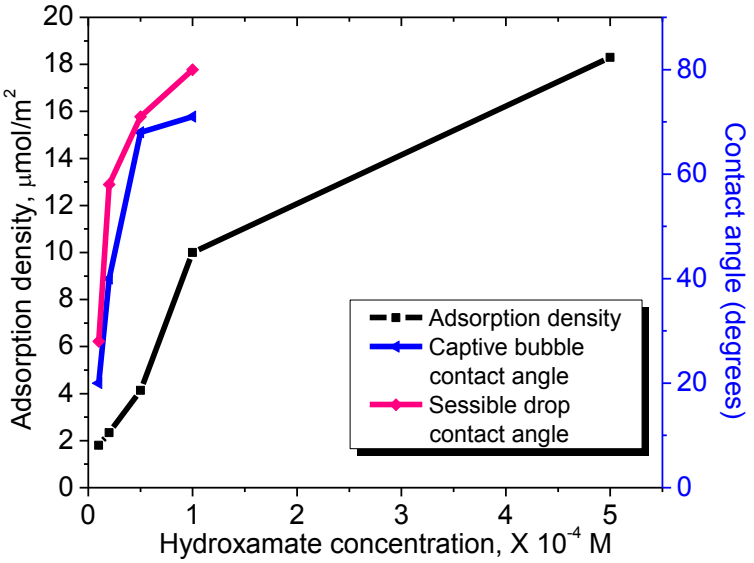

Figure 3.15 – Adsorption isotherm and contact angle results at low concentrations of hydroxamate for bastnaesite surface.

3.3.5 Characterization of Chemisorption at Low Hydroxamate Concentrations by SFVS

In order further investigate hydroxamate adsorption at low concentrations and identify conditions for what appears to be the formation of a well-ordered monolayer, SFVS was used to analyze the structure and conformation of hydroxamate at the bastnaesite surface.

As discussed in Chapter 2, SFVS can be applied in a variety of fields. Particularly, SFVS can be used to study surfactants structure and conformation information at surfaces or interfaces in the C-H vibrational region (Becraft et al., 2004; Hopkins et al., 2005; Conboy et al., 1996, 1997; Lu et al., 2005). For the ssp polarization combination, as it only contains the χ_{yyz} component (see equation 2.5), it can only detect vibrational modes with transition dipole moments with components perpendicular to the surface, or in other words, parallel to the surface normal.

Figure 3.16 shows the SFVS spectra of three different concentrations of octyl hydroxamic acid (OHA) adsorbed at bastnaesite surface. From Figure 3.16, it can be seen that the sum frequency vibrational spectra are similar for the three concentrations of OHA with a difference only in the relative peak intensities. Only two peaks appear in the spectra located at 2885-2890 cm^{-1} and 2945-2950 cm^{-1}, which are assigned to the symmetric stretching vibration (r^+) and the symmetric stretching Fermi resonance (r_{FR}^+) with a bending overtone of the CH_3 group, respectively (Conboy et al., 1997; Wang et al., 2008). In order to understand the spectra shown in Figure 3.16 more thoroughly, consideration of the local symmetry of the CH_2 hydrocarbon backbone is necessary. For an all-trans hydrocarbon chain, which is locally centrosymmetric regarding the methylene groups, little contribution from the methylene resonances will be observed due to this

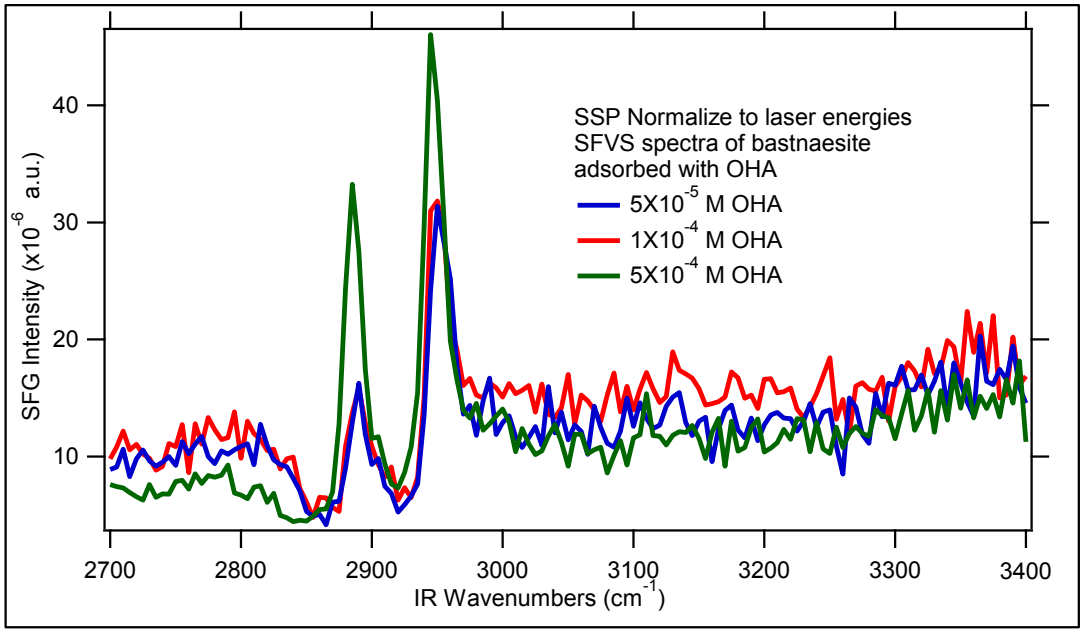

Figure 3.16 – Sum frequency vibrational spectra of C-H stretching region of octyl hydroxamic acid adsorbed at bastnaesite surface for different concentrations. The spectra were taken using s-polarized output, s-polarized visible and p-polarized infrared. The intensities of the SF were normalized to visible and IR beams intensities.

centrosymmety. As a result, the absence of CH_2-vibrational modes in Figure 3.16 is an indication that the hydroxamate molecules are in an all-trans conformation. If there are any gauche effects in the hydrocarbon backbone, we will be able to see the CH_2 vibrational bands in the SFVS spectra (Conboy et al., 1997). From further comparison of these three spectra, it can be noted that the intensities of the SFVS spectra for the 5×10^{-5} M and 1×10^{-4} M OHA are almost the same, while the SFVS intensity for 5×10^{-4} M OHA adsorption at bastnaesite surface is much larger than the former two. The reason for this might be due to a surface excess and multilayer formation. As the SF intensity is proportional to the number density detected, the intensity will be larger. On the other hand, as the surface density increases, the degree of conformational mobility within the hydrocarbon chains decreases, resulting in a more ordered chain (Conboy et al., 1997). These results suggest that even at a 50% monolayer coverage, hydroxamate molecules are in a well-ordered configuration at bastnaesite surface.

3.3.6 Wetting Characteristics of Bastnaesite with/without Hydroxamate Adsorption Using MDS

3.3.6.1 Interfacial Water Structure of Bastnaesite without Hydroxamate Adsorption

In order to understand the interaction between interfacial water and rare-earth mineral surfaces, MDS experiments were conducted at cerium-bastnaesite surface. Figure 3.17 is a snapshot and the zoom-in image of cerium-bastnaesite/water MDS. It can be noted that water molecules have two orientations. In one orientation hydrogen atoms coordinate with surface. In the other case, water molecules coordinate with surface cerium atoms through water oxygen atoms as expected. This is due to the interaction between the negatively charged surface fluoride ions with water hydrogen atoms as well

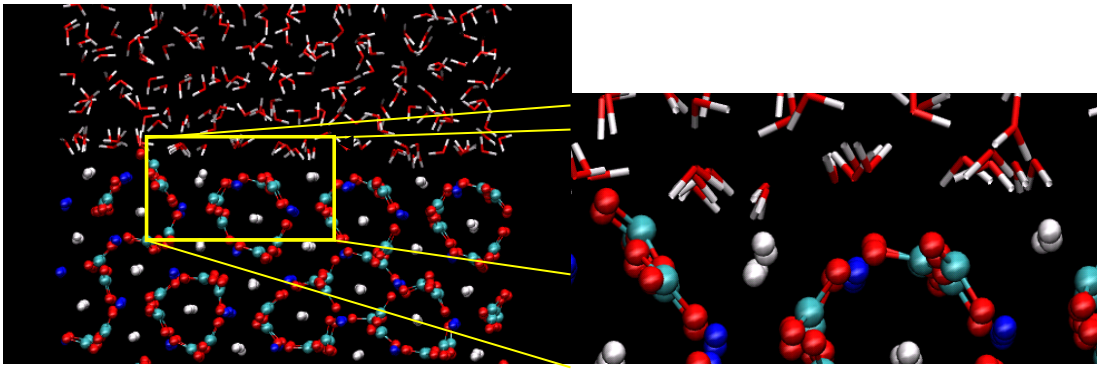

Figure 3.17 - MDS snapshot of cerium-bastnaesite/water zoom-in image (Red: oxygen; Blue: cerium; Cyan: carbon; White: fluorine).

as the interaction between the positively charged surface cerium ions with water oxygen atoms.

Figure 3.18 shows the water density distribution profiles along the crystal surface normal for Ce-bastnaesite. The zero distance represents the crystal surface. From the water distribution profile at Ce-bastnaesite, it can be found that although the bastnaesite surface is hydrophilic as discussed earlier, there is a gap, which is usually referred to as "water exclusion zone," between the crystal surface and the primary water layer. The gap distance is ~1.5 angstrom. The reason for the appearance of such a water exclusion zone at a hydrophilic surface is not clear. One possible reason might be related to the spacing of surface atoms. For Ce-bastnaesite, it has a relatively large Ce-Ce and F-F spacing at the surface, 6.993 and 7.019 angstrom, respectively. Thus, the surface site density of trivalent cerium atoms is relatively low (4.74 μmol/m^2) and as a result, the interfacial water molecules are not closed packed onto the surface. This also suggests that the presence of a "water exclusion zone" does not necessarily indicate a hydrophobic surface. Looking at the number of interacting interfacial water layers with the crystal surfaces, it can be seen that there are three water layers interacting with the surface, which implies

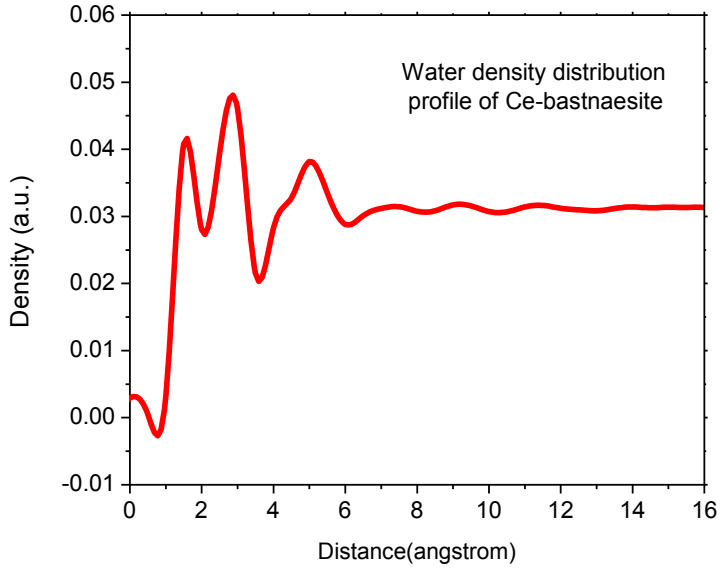

Figure 3.18 - Water density distribution profile along the surface normal at Ce-bastnaesite surface.

strong interaction of bastnaesite with interfacial water molecules.

To further understand the interfacial water structure at Ce-bastnaesite surface, the residence times for interfacial water molecules were also analyzed. As discussed in Chapter 2, the residence time is a dynamic property of interfacial water molecules and it describes the tendency of the interfacial water molecules to stay at the surface. Thus, the longer the residence time, the stronger the interaction between the surface and the water molecules, and the more hydrophilic the surface. Other details about residence time analysis have been discussed in Chapter 2 and will not be described here.

Figure 3.19 shows the residence time profile for Ce-bastnaesite. It can be seen that the residence time profile for Ce-bastnaesite has two major peaks, with the primary peak having a residence time of about 42 ps and the second peak about 17 ps. In order to have a better understanding of these residence time data and how it explains the hydrophilic

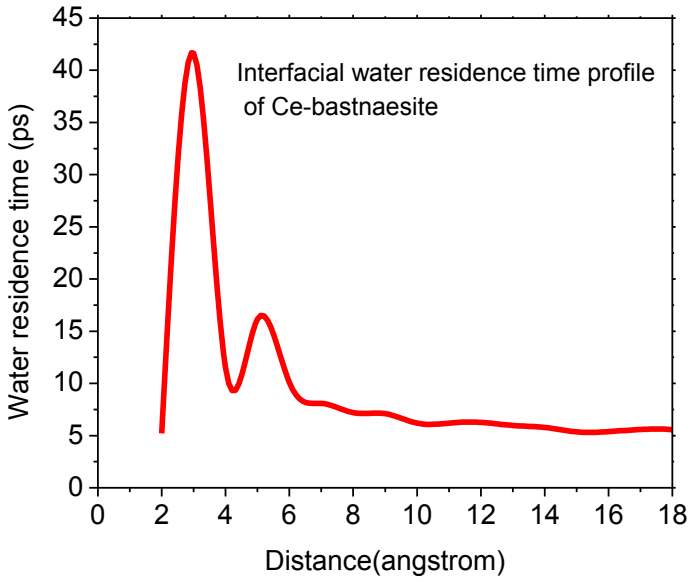

Figure 3.19 - Water residence time profile of Ce-bastnaesite.

characteristics of bastnaesite surface, the residence times of other crystal surfaces are summarized and compared with that of bastnaesite. See Table 3.11. From Table 3.11, it can be seen that for hydrophilic surfaces, including Ce-bastnaesite, halite and the alumina face of kaolinite, the residence time is much larger than at hydrophobic surfaces such as pyrophyllite and silica face of kaolinite. The fact that the residence time of the primary water layer at Ce-bastnaesite surface is ~42 ps confirms its hydrophilicity. Even for the second water layer, the residence time is 17 ps. This again indicates the strong hydrophilic feature of bastnaesite surface.

In order to have a more detailed understanding of the interfacial water characteristics of the surface, the interfacial water dipole orientation and hydrogen atoms position were analyzed, respectively. As discussed in Chapter 2, two critical angles were used to describe the water orientation characteristic. As is shown in Figure 2.10 in section 2.1.3.2, the angle α is defined as the angle between water dipole moment and surface normal and angle β is the angle of the two hydrogen atoms position with respect to the surface normal.

Figure 3.20 shows the interfacial water dipole orientation distribution contour of Ce-bastnaesite surface. From Figure 3.20, it can be seen the water dipole moment density (A) has two ranges; one is from about 5^o to 30^o, with a sharp peak at about 18^o. The other range is from 165^o to 180^o, centered at 175^o. This indicates that the water molecules have two different dipole moment orientations, one pointing toward the crystal surface and the other pointing to the opposite of the surface, which is consistent with the observation shown in Figure 3.18. The reason for this is as discussed is that there are both positively charged cerium ions and negatively charge fluorine ions. Thus, water oxygen atoms can be attracted by cerium ions and water hydrogen ions can be attracted by fluorine ions in

Table 3.11 - Comparison of interfacial water residence times at different surfaces.

Mineral		Primary water layer residence time, ps	Reference
Bastnaesite ($CeFCO_3$)		41.6 (hydrophilic)	Present study
Halite (NaCl)		32.5 (hydrophilic)	(Du, 2008)
Pyrophyllite ($Al_2Si_4O_{10}(OH)_2$)		17 (hydrophobic)	(Yin, 2012)
Kaolinite	Alumina face	29.3 (hydrophilic)	
	Silica face	21.4(hydrophobic)	

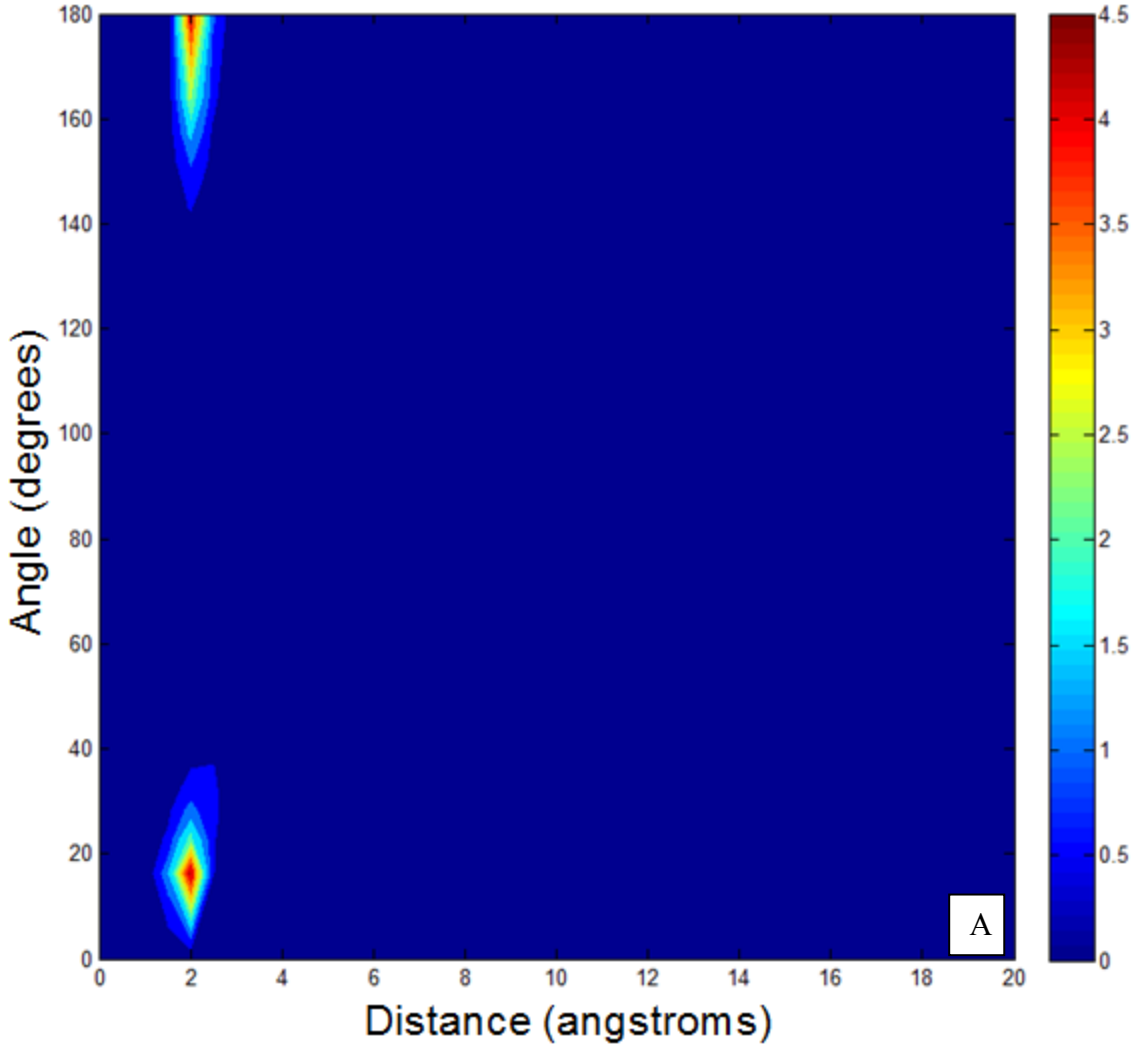

Figure 3.20 - Water dipole moment density distribution contour (A) and hydrogen atoms position density distribution (B) of Ce-bastnaesite.

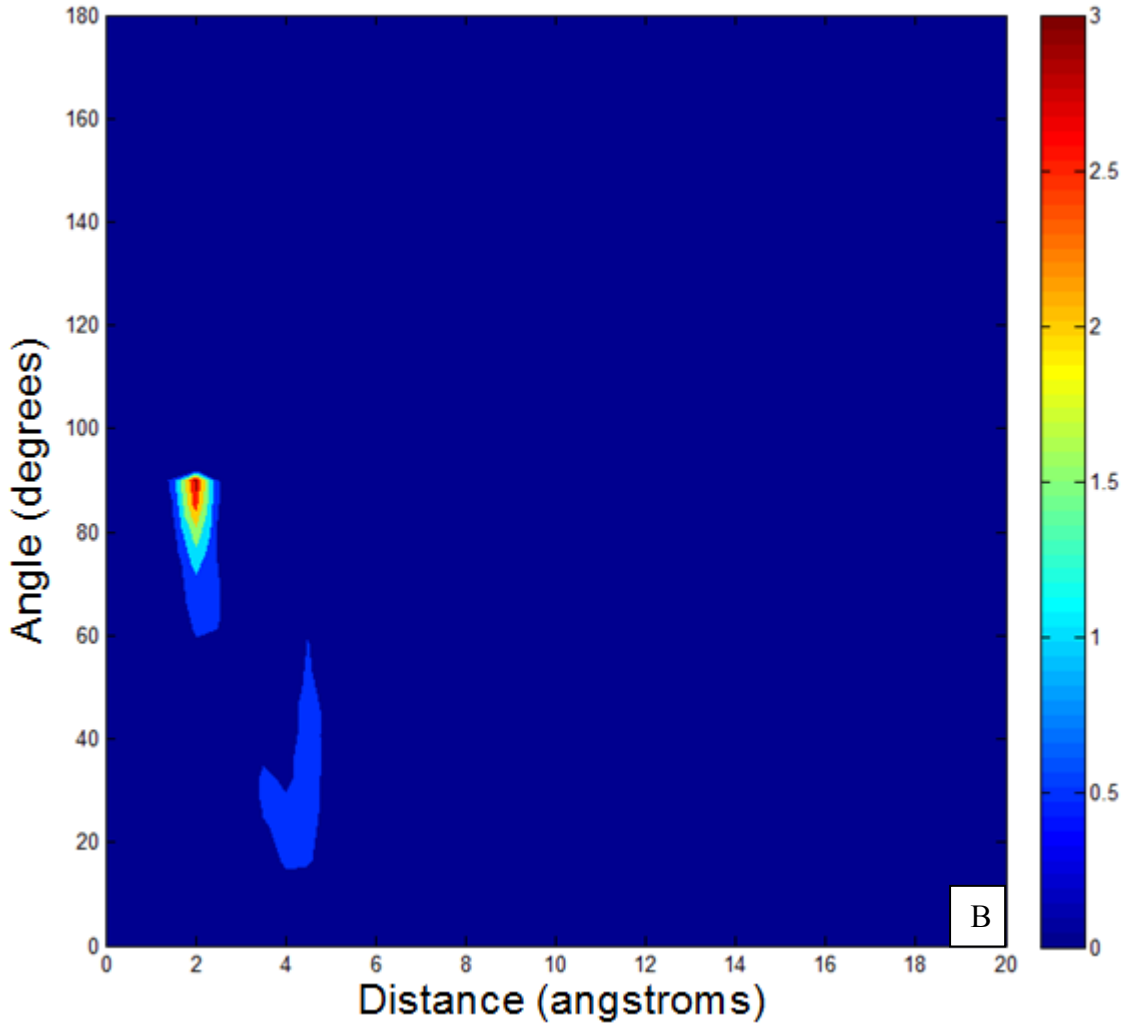

Figure 3.20 - Continued.

the surface, giving rise to two distinct dipole moment density distributions. When looking at the hydrogen atoms position density distribution (B), the angle ranges from 60^{o} to 90^{o}, with a sharp peak at around 90^{o}. This suggests that the hydrogen atoms favor a perpendicular position with respect to the surface normal.

3.3.6.2 Wetting Characteristics of Bastnaesite with Hydroxamate Adsorption

The wetting characteristics of bastnaesite surface adsorbed with different levels of hydroxamate have been investigated and discussed using contact angle measurements. It was found that below monolayer coverage, the contact angle increases with increasing adsorption density at the surface. It is expected that below monolayer coverage, interfacial water molecules can interact with bastnaesite surface, giving rise to some degree of hydrophilicity. However, the interfacial water molecules behavior below monolayer coverage as well as the hydrophobic surface state of bastnaesite with different levels of hydroxamate adsorption has not been described from the molecular level. Thus, in this section of the dissertation, first, the interfacial water molecules behavior with hydroxamate molecules adsorbed at Ce-bastnaesite surface below monolayer coverage is discussed. Then, the hydrophobic surface state of bastnaesite with different levels of hydroxamate adsorption (8.3%, 25% and 50%, calculation based on assumption of hydroxamate to cerium ratio being 1 : 1) was investigated using MDS contact angle method.

Figure 3.21 shows a MDS snapshot of Ce-bastnaesite surface for 50% monolayer coverage of chemisorbed hydroxamate. It can be seen that there are interfacial water molecules interacting with bastnaesite surface between spaces of adsorbed hydroxmate

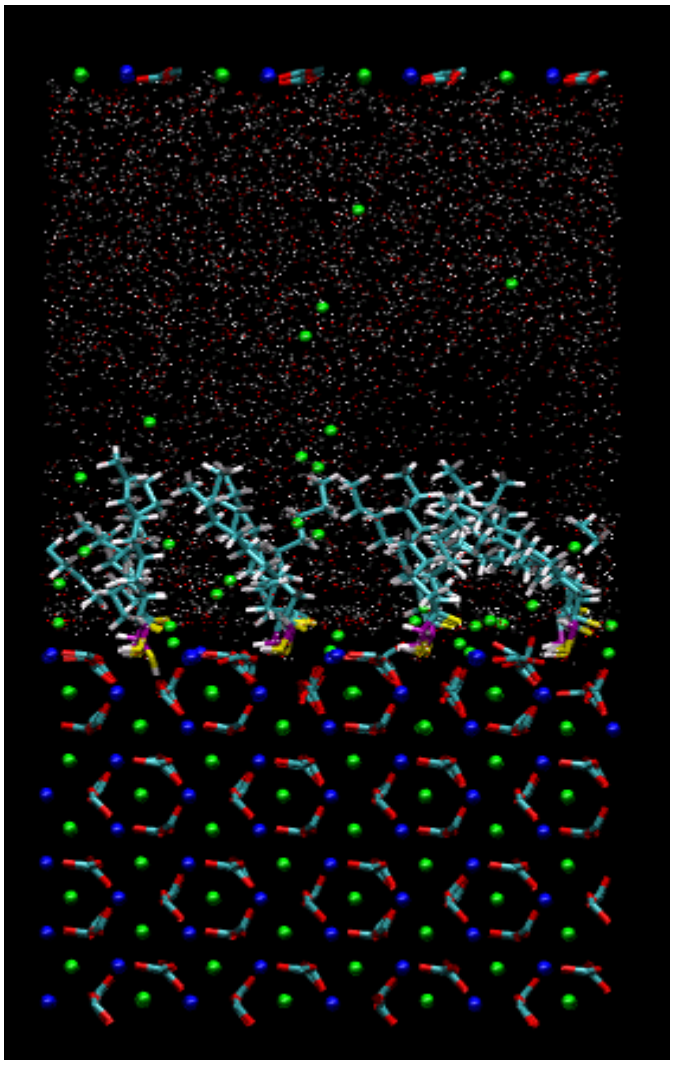

Figure 3.21 - MDS snapshot of Ce-bastnaesite surface for 50% monolayer coverage of chemisorbed hydroxamate (Red: oxygen; Blue: cerium; Green: fluorine; Cyan: carbon; White: hydrogen, Yellow: hydroxamte oxygen; Purple: nitrogen).

due to incomplete coverage by hydroxamate molecules, which accounts for the partial degree of hydrophilicity of the surface. Thus, it is expected that different levels of hydroxamate coverage at bastnaesite surface result in different wetting characteristics and consequently different contact angles from MD simulations. The force field used for this MDS is then used for contact angle MD simulation at bastnaesite surface with different levels of hydroxamate coverage to investigate the effect of different hydroxamate coverage on the hydrophobic surface state of bastnaesite.

The effect of different levels of hydroxamate coverage at bastnaesite surface was studied using MD simulations. Three levles of hydroxamte coverage at bastnaesite surface, 8.3%, 25%, 50%, were employed for the contact angle MD simulations. A water drop was placed on top of the bastnaesite surface with different levels of hydroxamte coverage. The simulations were first carried out for 500 ps in order to equilibrate the systems and then continued for 1 ns. Two-dimensional water density distribution maps were constructed from the x-z plane based on the simulation results during the last 1 ns. Figure 3.22 is the top view of different levels of hydroxamate adsorption at bastnaesite surface.

Figure 3.23 shows the MDS snapshot of the initial configuration and the configuration after 40 ps for a droplet at Ce-bastnaesite surface with different levels of hydroxamate coverage. It can be seen that after 40 ps MD simulation, the water drop at the bastnaesite surface with only 8.3% hydroxamate coverage has already spread over the surface. In other words, the surface is close to complete wetting by the water droplet, indicating hydrophilic characteristics of the surface. When hydroxamate coverage at bastnaesite surface increases to 25%, increased hydrophobicity is observed as shown in

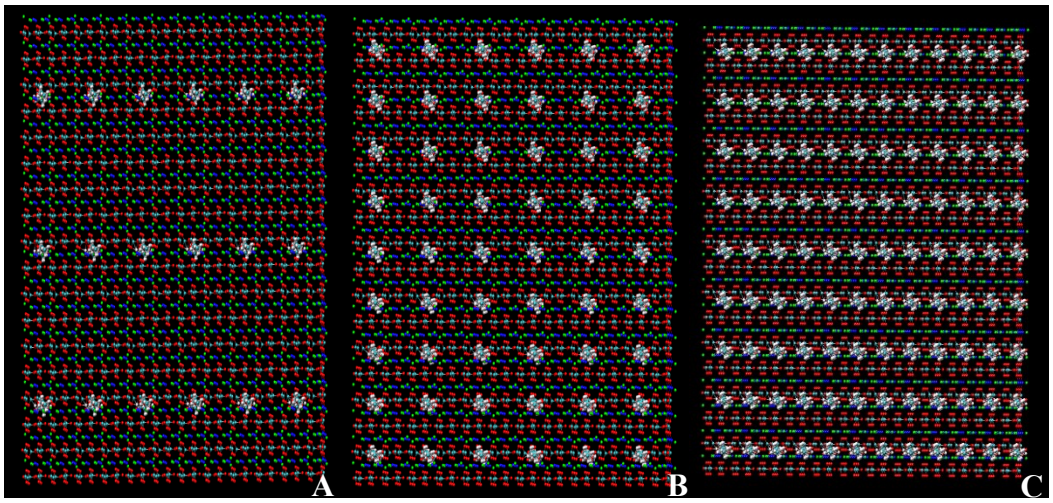

Figure 3.22 - Different levels of hydroxamate adsorption at bastnaesite surface (top view: A: 8.3% hydroxamte coverage, B: 25% hydroxamate coverage, C: 50% hydroxamte coverage).

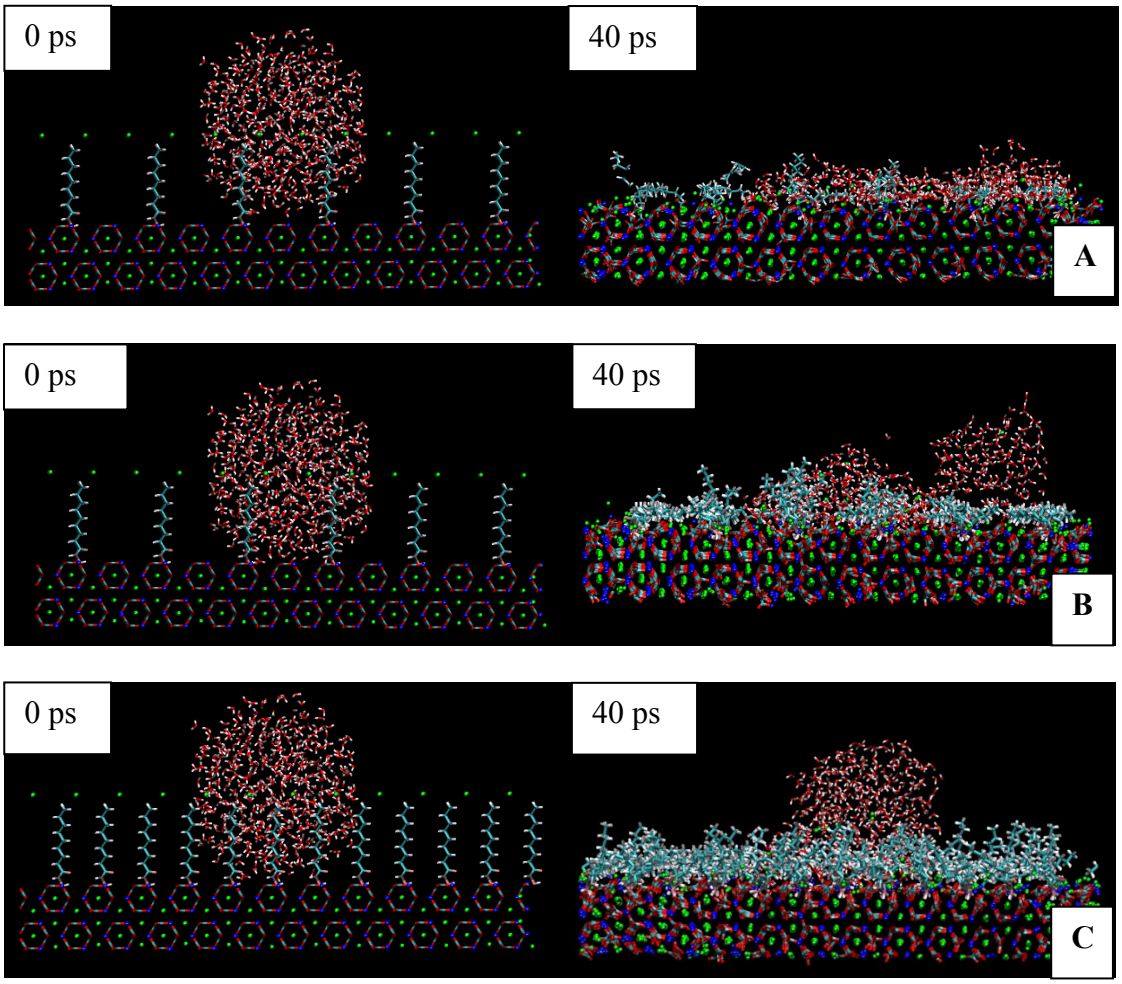

Figure 3.23 - MDS snapshot of the initial configuration and the configuration after 40 ps for a droplet at Ce-bastnaesite surface with different levels of hydroxamate coverage, (A): 8.3% hydroxamate coverage, (B): 25% hydroxamate coverage, (C): 50% hydroxamate coverage (Red: oxygen; Blue: cerium; Green: fluorine; Cyan: carbon; White: hydrogen; Pink: hydroxamte oxygen; Gray: nitrogen).

Figure 3.23 (B). It is also interesting to note that a part of the water drop is repelled and separated from the initial drop due to higher hydroxamate adsorption density and consequently, an elevated degree of hydrophobicity at the surface. For 50% hydroxamate coverage at bastnaesite surface, the water drop does not spread over the surface. Rather it keeps a round shape and exhibits a large contact angle due to the high adsorption density of hydroxamate at the surface and as a result, high hydrophobicity of the surface.

The differences in wetting characteristics of the water drop at bastnaesite surface with different levels of hydroxamate coverage after the same simulation time also indicate different wetting rate of the water drop at these three surfaces. Based on Figure 3.23 and the discussions herein, it can be concluded that bastnaesite surface with 8.3% hydroxamate coverage has the largest wetting rate, followed by 25% hydroxamate coverage, and 50% hydroxamate coverage exhibits the slowest wetting rate. The configuration change compared to the initial configuration is due to crystal relaxation during MD simulations.

Figure 3.24 presents the visualization of the two-dimensional water density distribution maps at the bastnaesite surface with different levels of hydroxmate coverage. It should be noted that in order avoid density fluctions at the solid-liquid interface, points below 8 angstroms frrom bastnaesite surface were not taken into account (Werder et al., 2003). Besides, as there are hydroxamate collectors adsorbed at the surface, especially in the case of 50% coverage, there is a distinct hydroxamate layer on the surface; the points within the hydroxamate layer were not considered. Based on these assumptions, the contact angles at these three surface were determined. See Figure 3.24. θ is used to describe the contact angles as shown in Figure 3.24. For bastnaesite surface with 8.3%

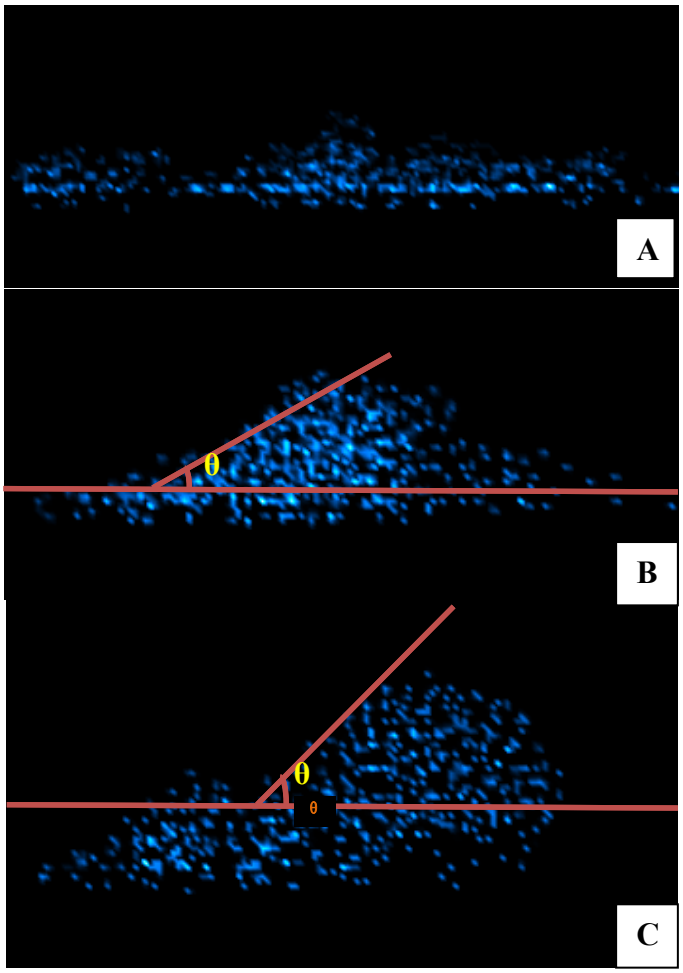

Figure 3.24 - Visualization of the two-dimensional water density analysis for a water droplet at the bastnaesite surface with different levels of hydroxamate coverage: (A): 8.3% hydroxamate coverage, (B): 25% hydroxamate coverage, (C): 50% hydroxamate coverage.

hydroxamate coverage, the contact angle was determined to be ~0^{o}. For 25% hydroxamate coverage, the contact angle of bastnaesite surface is about 30^{o}. When hydroxamate coverage increased to 50% coverage, the contact angle is about 45^{o}.

The contact angle results from MD simulations are summerized in Table 3.12 and compared with experimental results. NA in Table 3.12 means contact angle results at that specific adsorption density were not measured by the experimental method. From Table 3.12, it can be seen that the contact angle result from MD simulation for 50% hydroxamate coverage, which corresponds to an adsorption density of 2.4 μmol/m^{2}, is in good agreement with the experimental value. The fact that when hydroxamate coverage at bastnaesite surface increases, which corresponds to an increase in hydroxamate adsorption density, the contact angle result from MD simulations also increases is consistent with the observation from experimental contact angle measurements discussed in section 3.3.5. It has to be noticed that for the contact angle measurements using MDS, the hydroxamate molecules were chemisorbed at the surface by electrostatic interactions with cerium ions by removing some fluoride ions from the surface, which may account for some of the difference with experiental measurements.

It can be noticed that for 50% hydroxamate coverage, the two-denmensional water density contour shown in Figure 3.24 is not symetric as usually observed. No water density distribution is observed on the right side of the water map shown in Figure 3.24 (C). This is due to the presence of high density hydroxamate molecules adsorbed at the surface which inhibits the spreading of the water droplet over the surface. Consenquently, the water droplet retains its round shape and forms a relatively larger contact angle above the hydroxamate adsorption layer. Figure 3.25 shows a MDS snapshot zoom-in image of

Table 3.12 - Comparison of contact angle results from experiment with MD simulations.

Surface coverage (%)	Adsorption density (μmol/m^2)	Contact angle	
		Experiment	MDS (θ)
8.3	0.4	NA	~0^o
25	1.2	NA	~30^o
50	2.4	~42^o	~45^o

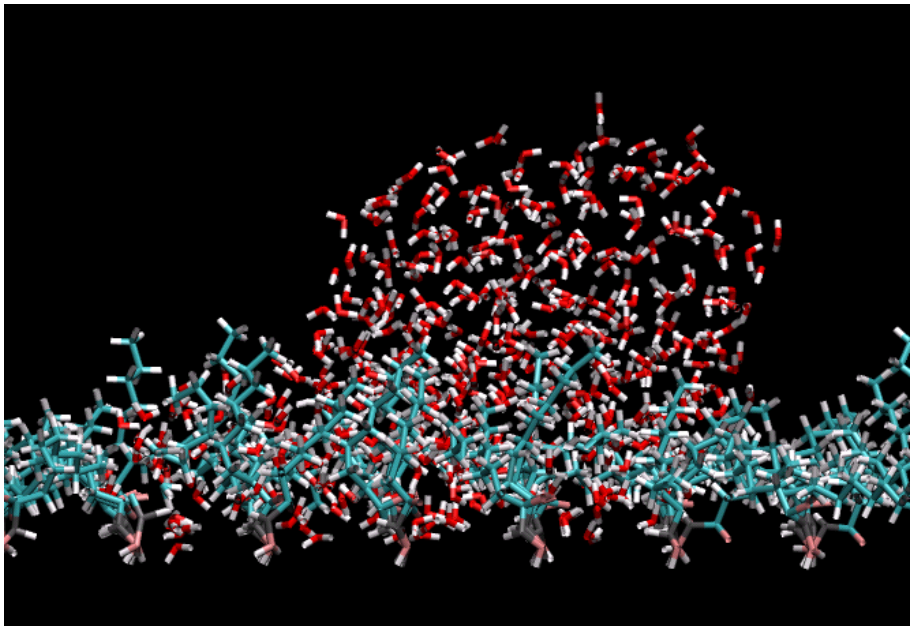

Figure 3.25 - MDS snapshot zoom-in image of the configuration after ~400 ps for a droplet at Ce-bastnaesite surface with 50% hydroxamate coverage (only hydroxamate adsorption layer and the water droplet are shown), (Red: oxygen; Cyan: carbon; White: hydrogen; Pink: hydroxamate oxygen; Gray: nitrogen).

the configuration after 400 ps simulation run for a droplet at Ce-bastnaesite surface with the hydroxamate adsorption layer. Figure 3.25 shows a MDS snapshot zoom-in image of the configuration after 400 ps simulation run for a droplet at Ce-bastnaesite surface with 50% hydroxamate coverage (only hydroxamate adsorption layer and the water droplet are shown in Figure 3.25). From Figure 3.25 it can be seen that the water droplet tends to spread towards the right side of the surface. As there is a distinct hydroxamate layer, the spreading is inhibited and kept in a round shape above the hydroxamate layer.

3.4 Summary

The surface chemistry aspects of bastnaesite were examined based on solution chemistry calculations and stability diagrams. In this way, surface charge characteristics and collector adsorption features were examined, including the corresponding hydrophobic surface state at low concentrations of hydroxamate using both experimental and MD simulation methods.

The effect of CO_2 pressure on the solution chemistry of bastnaesite – H_2O system was considered and investigated. The stability as well as the speciation distribution diagrams were obtained using Stabcal software (W32-STABCAL). Stability domains were identified with respect to pH and CO_2 pressures.

In a closed system, transformations of bastnaesite to cerium fluoride occur at low pH values (acidic pH) and to cerium hydroxide at high pH. For an open system when CO_2 is present, the stability diagrams are quite different. The cerium hydroxide stability field disappears for CO_2 pressures considered and bastnaesite becomes the only stable phase at high pH values due to reactions with CO_2 and formation of carbonate anions. Besides, when the CO_2 pressure increases, the stability field for bastnaesite shifts to the left side of

the stability diagram, the more acidic pH side, and the pH range for the cerium fluoride stability field is compressed simultaneously. Speciation-distribution diagrams for the bastnaesite-H_2O system with $10^{-3.5}$ atm CO_2 show that cerium ions form complexes with fluoride and carbonate ions. These ions may play a role in the surface charge characteristics of bastnaesite.

Microelectrophoresis measurements found that the PZC of bastnaesite is about pH 8.1, which is consistent with reported data from the literature (Li, 1967; Ren et al., 1997; Ren et al., 2000). The stability diagram with $10^{-3.5}$ atmosphere CO_2 was then used to explain the electrophoresis results for bastnaesite and correlation of surface charge and the stability diagram was established. At different pH values, it is expected that the zeta potential measured actually represents the surface charge associated with different species stable at the surface. CeF_3 is stable at low pH values and the surface is positively charged from electrophoresis results. CeF_3 is transformed to $CeFCO_3$ stability field at higher pH and the surface becomes negatively charged.

In order to investigate the solution concentration limitation of octyl hydroxamic acid in DI water, dynamic light scattering (DSL) measurements were conducted at certain concentrations of OHA and it was found that at the concentrations examined (above 1×10^{-3} M), at pH 9.3, there are particles present in the solution. Thus it was estimated that the solubility limitation for OHA is about 1×10^{-3} M at pH 9.3. Further studies need to be conducted for exact OHA solubility determination. Adsorption experiments in this dissertation research were done at concentrations below 1×10^{-3} M OHA.

Adsorption density measurements at low concentrations of hydroxamate were made by the solution depletion method using high sensitivity TOC analysis. The results show

that the adsorption density increases with increasing hydroxamate concentration. Monolayer adsorption occurs at about 1×10^{-4} M, considering the hydroxamate cross sectional area to define the monolayer condition. Below this concentration, only submonolayer coverage is achieved. Below monolayer coverage, the adsorption of hydroxamate at the bastnaesite surface is expected to be a surface reaction (chemisorption) process. The hydroxamate collector can react with the surface as well as with RE cations from lattice sites through a chelating reaction (Pradip and Fuerstenau, 1983). Possible reactions are discussed based on aqueous species available in the system from the speciation distribution diagrams.

Wetting characteristics by contact angle measurements and MD simulations both indicate that the bastnaesite surface is hydrophilic in the absence of hydroxamate adsorption. Contact angle measurements were then conducted for the bastnaesite surface with adsorbed hydroxamate at low levels of adsorption density (below monolayer coverage) by sessile drop and captive bubble methods. Results show that the contact angle increases with an increase in hydroxamate concentration and an increase in the corresponding adsorption density. These results indicate an increase in the hydrophobicity of the bastnaesite surface. It appears that full monolayer coverage has been achieved (contact angle = 70 – 80^{o}, for apparent adsorption density for monolayer = 8.1 μmol/m^{2}).

The sum frequency vibrational spectroscopy (SFVS) technique was used to identify conditions for what appears to be the formation of a well-ordered adsorbed state. The results suggest that even at a 50% monolayer coverage, hydroxamate molecules are in a well-ordered configuration at the bastnaesite surface.

MD simulations were conducted to investigate the hydrophobic surface state of cerium-bastnaesite surface with three different levels of hydroxamate adsorption. Below monolayer coverage (50% coverage), interfacial water molecules can accommodate and interact with bastnaesite surface between spaces of adsorbed hydroxmate due to incomplete coverage by hydroxamate molecules. This gives rise to the partial degree of hydrophilicity of the surface. Contact angle results from MD simulations with different levels of hydroxamate coverage show that, when hydroxamate coverage increases, which corresponds to an increase in hydroxamate adsorption density, the contact angles from MD simulations also increase indicating an increase in the hydrophobicity. This is consistent with the observation from experimental contact angle measurements.

CHAPTER 4

SUMMARY AND CONCLUSIONS

The major objective of this dissertation is to examine the surface chemistry of semisoluble salt minerals, including the interfacial wetting characteristics and surface charge for different fluorite surfaces (111, 100 and 110 surfaces) as well as the rare earth mineral, bastnaesite. Particularly, the effect of crystal surface structure on the wetting characteristics and surface charge of fluorite surfaces were investigated and discussed. Besides traditional contact angle measurements, the wetting characteristics of the rare earth mineral bastnaesite were also investigated using molecular dynamics simulation (MDS), which includes the hydration state of the bastnaesite surface. Finally, the interfacial chemistry of bastnaesite was considered with respect to the adsorption features of octyl hydroxamic acid. The following discussion summarizes the accomplishments and contributions.

4.1 Fluorite

Surface properties of specific surfaces have not been reported, including the wetting characteristics and surface charge features. The wetting characteristics of different fluorite surfaces (111, 100 and 110) were investigated using contact angle measurements, molecular dynamics simulation (MDS) and sum frequency vibrational spectroscopy (SFVS). Nonequilibrium contact angle results indicate that the 111 surface of fluorite exhibits modest hydrophobicity, with a contact angle of ~20^{o}, while the 100 and 110

surfaces are completely hydrophilic as indicated by contact angles of 0^o. MD simulations for a water drop at the 111 and 110 surfaces of fluorite as well as detailed analysis of the interfacial water structure from both MDS and SFVS were also conducted. Results support the findings from experimental contact angle measurements.

The surface charge characteristics of different fluorite surfaces (111, 100 and 110) were examined from flat plate streaming potential measurements. Results show that the cleaning procedure has a significant effect on the surface charge of fluorite for the nonequilibrium state. When cleaning fluorite with only DI water, both the 111 and 100 surfaces show a negative surface charge and the surfaces exhibit some degree of hydrophobicity, indicating the presence of contamination, which might account for the apparent negative surface charge of both surfaces. When the surfaces are free from contamination, a positive zeta potential was obtained for all three surfaces. Such a finding seems to contradict to the fact that fluoride ions are exposed at the 111 surface of fluorite, and thus a negative surface charge might be expected. This was argued based on dipole moment distribution analysis from MD simulations which show that a sublayer calcium ions are playing a significant role in contributing to the surface charge and giving rise to the positive sign. The finding of a positive surface charge of the 100 surface of fluorite in the absence of contamination suggests that calcium ions are exposed at the surface.

Under equilibrium condition (solution saturated with CaF_2), when the aqueous phase is prepared as a saturated calcium fluoride solution, changes in the surface properties were observed. All the surfaces appear to recrystallize as the 111 surface and exhibit contact angles of ~20^o. Furthermore, the sign of the surface charge of the 111 fluorite surface changes from a negatively charged surface in water to a positively charged

surface in saturated calcium fluoride solution. It is expected that preferential hydration of lattice fluoride ions results in a surface excess of calcium ions (Miller et al., 2004).

4.2 Bastnaesite

The surface chemistry aspects of bastnaesite were examined based on solution chemistry calculations and stability diagrams. In this way, surface charge characteristics and collector adsorption features were examined, including the corresponding hydrophobic surface state at low concentrations of hydroxamate using both experimental and MD simulation methods.

Stability diagrams show that different species stay stable in the system at different pH values. The effect of CO_2 pressure has not been considered previously and was discussed in this dissertation research. It was found that CO_2 pressure gives rise to changes in the stability diagrams. In a closed system, transformations of bastnaesite to cerium fluoride at low pH values (acidic pH) and to cerium hydroxide at high pH occurs. When CO_2 is present in the system, cerium hydroxide stability field disappears for CO_2 pressures considered and bastnaesite becomes the only stable phase at high pH values. The stability diagram with $10^{-3.5}$ atmosphere CO_2 was then used to explain the electrophoresis results for bastnaesite and correlation of surface charge and a stability diagram was established. At different pH values, it is expected that the zeta potential measured actually represents the surface charge associated with different species stable at the surface. CeF_3 is stable at low pH values and the surface is positively charged from electrophoresis results. CeF_3 connects to $CeFCO_3$ stability field at higher pH and the surface becomes positively charged. The PZC of bastnaesite was found to be pH ~8.1 and confirms results from the literature (Li, 1967; Ren et al., 1997; Ren et al., 2000). Besides,

cerium and fluoride species speciation-distribution diagrams for the bastnaesite-H_2O system open to the atmosphere were also obtained and results show that cerium ions form complexes with fluoride and carbonate ions, which may play a role in the surface charge characteristics of bastnaesite.

Octyl hydroxamic acid (OHA) from Cytec was used for examination of collector adsorption features at the bastnaesite surface. First, the solubility of OHA at pH 9.3 was determined by the dynamic light scattering (DSL) technique and the solubility limit was estimated to be about 1×10^{-3} M. Then low concentrations of hydroxamic acid were prepared for adsorption isotherm determination and to describe the hydrophobic state of the bastnaesite surface.

Chemisorption region of hydroxamate at the bastnaesite surface has not been studied. Previous research at UC Berkeley (Pradip, 1981) considered the multilayer physisorption region. Adsorption density results at low concentrations of hydroxamate were determined by solution depletion using high sensitivity TOC analysis. The results show that the adsorption density increases with increasing hydroxamate concentration. Monolayer adsorption occurs at about 1×10^{-4} M, considering the hydroxamate cross sectional area to define the monolayer condition. Below this concentration, only submonolayer coverage is achieved. Chemisorption at submonolayer coverage was explained and discussed. Below monolayer coverage, the adsorption of hydroxamate at the bastnaesite surface is expected to be a surface reaction (chemisorption) process. The adsorption stability below monolayer coverage has been examined by washing with acetone, alcohol and DI water, and the bastnaesite surface still maintained its hydrophobic state. Direct evidence for chemisorption has not been established. The hydroxamate collector can react

with the surface as well as with RE cations from lattice sites through a chelating reaction (Pradip and Fuerstenau, 1983). Possible reactions are discussed based on aqueous species available in the system from the speciation distribution diagrams.

Wetting characteristics of bastnaesite had not been described previously. The bastnaeiste surface was found to be hydrophilic from contact angle measurements and MD simulations. These two methods were then used to investigate the hydrophobic surface state of bastnaesite at low levels of hydroxamate adsorption. Results from both experimental contact angle measurements and MD simulation results show that the contact angle increases with increasing hydroxamate adsorption density, indicating an increase in the hydrophobicity of the bastnaesite surface.

The SFVS technique was used to identify conditions for what appears to be the formation of a well-ordered monolayer. The results suggest that even at a 50% monolayer coverage, hydroxamate molecules are in a well-ordered configuration at the bastnaesite surface.

REFERENCES

Abeidu, A. M., 1972, "The separation of monazite from zircon by flotation," *Journal of the Less Common Metals*, Vol. 29, No. 2, pp.113-119.

Alder, B. J., and Wainwright, T. E., 1959. "Studies in molecular dynamics. I. general method," *The Journal of Chemical Physics*, Vol. 31, No. 2, pp. 459-466.

Amankonah, J. O., and Somasundaran, P., 1985, "Effects of dissolved mineral species on the electrokinetic behavior of calcite and apatite," *Colloids and Surfaces*, Vol. 15, No. 0, pp. 335-353.

Austen, K. F., Wright, K., Slater, B., and Gale, J. D., 2005, "The interaction of dolomite surfaces with metal impurities: A computer simulation study," *Physical Chemistry Chemical Physics*, Vol. 7, No. 24, pp. 4150-4156.

Bain, C. D., 1995, "Sum-frequency vibrational spectroscopy of the solid/liquid interface," *Journal of the Chemical Society, Faraday Transactions*, Vol. 91, No. 9, pp. 1281-1296.

Becraft, K. A., and Richmond, G. L., 2001, "In situ vibrational spectroscopic studies of the CaF_2/H_2O interface," *Langmuir*, Vol. 17, No. 25, pp. 7721-7724.

Becraft, K. A., Moore, F. A., and Richmond, G. L., 2003, "Charge reversal behavior at the CaF_2/H_2O/SDS interface as studied by vibrational sum frequency spectroscopy," *The Journal of Physical Chemistry B*, Vol. 107, No. 16, pp. 3675-3678.

Becraft, K. A., Moore, F. A., and Richmond, G. L., 2004, "In-situ spectroscopic investigations of surfactant adsorption and water structure at the CaF_2/aqueous solution interface," *Physical Chemistry Chemical Physics*, Vol. 6, No. 8, pp. 1880-1889.

Berendsen, H. J. C., Grigera, J. R., and Straatsma, T. P., 1987a, "The missing term in effective pair potentials," *The Journal of Physical Chemistry*, Vol. 91, No. 24, pp. 6269-6271.

Berendsen, H. J. C., Van Gunsteren, W. F., Egberts, E., and De Vlieg, J., 1987b, "Dynamic simulation of complex molecular systems," *Supercomputer Research in Chemistry and Chemical Engineering*, K. F. Jensen, ed., October 22, 1987, pp.106-122, ACS.

Brown, T.E., Lemay H. E. H., Bursten, B. E, Murphy, C.,Woodward, P., 2008, *Chemsitry: The Central Science*, New York: Prentice Hall, 1232 pp.

Calara, J. V., and Miller, J. D., 1976, "Determination of madelung constants for infinite and semi-infinite lattices by direct summation," *The Journal of Chemical Physics*, Vol. 65, No. 2, pp.843-844.

Cheng, J., Hou, Y., and Che, L., 2007, "Flotation separation on rare earth minerals and gangues," *Journal of Rare Earths*, Vol. 25, No. 1, pp. 62-66.

Cheng, T. W., Holtham, P. N., and Tran, T., 1993, "Froth flotation of monazite and xenotime," *Minerals Engineering*, Vol. 6, No. 4, pp. 341-351.

Cheng, T. W., 2000, "The point of zero charge of monazite and xenotime," *Minerals Engineering*, Vol. 13, No. 1, pp.105-109.

Chi, R., and Wang, D., 1996, *Rare Earth Mineral Processing and Extraction Technology*, China Science Press, 100 pp.

Conboy, J. C., Messmer, M. C., and Richmond, G. L., 1996, "Investigation of surfactant conformation and order at the liquid−liquid interface by total internal reflection sum-frequency vibrational spectroscopy," *The Journal of Physical Chemistry*, Vol. 100, No. 18, pp. 7617-7622.

Conboy, J. C., Messmer, M. C., and Richmond, G. L., 1997, "Dependence of alkyl chain conformation of simple ionic surfactants on head group functionality ss studied by vibrational sum-frequency spectroscopy," *The Journal of Physical Chemistry B*, Vol. 101, No. 34, pp.6724-6733.

de Leeuw, N. H., Parker, S. C., and Rao, K. H., 1998, "Modeling the competitive adsorption of water and methanoic acid on calcite and fluorite surfaces," *Langmuir*, Vol. 14, No. 20, pp. 5900-5906.

de Leeuw, N. H., and Cooper, T. G., 2003, "A computational study of the surface structure and reactivity of calcium fluoride," *Journal of Materials Chemistry*, Vol. 13, No. 1, pp. 93-101.

deBruyn, P.L., and Agar, G. E., 1962, "Surface chemistry in flotation," In *AIME*, D. W. Fuerstenau, ed., New York.

Drelich, J., Wilbur, J. L., Miller, J. D., and Whitesides, G. M., 1996, "Contact angles for liquid drops at a model heterogeneous surface consisting of alternating and parallel hydrophobic/hydrophilic strips," *Langmuir*, Vol. 12, No. 7, pp. 1913-1922.

Drzymala, J., 1994a, "Characterization of materials by hallimond tube flotation. Part 1: Maximum size of entrained particles," *International Journal of Mineral Processing*, Vol. 42, No. 3-4, pp. 139-152.

Drzymala, J., 1994b, "Hydrophobicity and collectorless flotation of inorganic materials," *Advances in Colloid and Interface Science*, Vol. 50, pp. 143-185.

Du, H., 2008, "Flotation Chemistry of Selected Alkali Halide Salts and Naturally Hydrophobic Minerals: A Molecular Dynamics Simulation Study," Ph. D. Thesis, Univeristy of Utah, Salt Lake City, UT., 223 pp.

Du, Q., Freysz, E., and Shen, Y. R., 1994a, "Vibrational spectra of water molecules at quartz/water interfaces," *Physical Review Letters*, Vol. 72, No. 2, pp.238-241.

Du, Q., Freysz, E., and Shen, Y. R., 1994b, "Surface vibrational spectroscopic studies of hydrogen bonding and hydrophobicity," *Science*, Vol. 264, No. 5160, pp. 826-828.

Eriksson, R., Merta, J., and Rosenholm, J. B., 2007, "The calcite/water interface: I. Surface charge in indifferent electrolyte media and the influence of low-molecular-weight polyelectrolyte," *Journal of Colloid and Interface Science*, Vol. 313, No. 1, pp. 184-193.

Fa, K., Jiang T., Nalaskowski, J., and Miller, J. D., 2003, "Interaction forces between a calcium dioleate sphere and calcite/fluorite surfaces and their significance in flotation," *Langmuir*, Vol. 19, No. 25, pp. 10523-10530.

Fa, K., 2004, "Interfacial Chemistry in the Fluorite and Calcite Flotation Systems," Ph. D. Thesis, University of Utah, Salt Lake City, UT., 235 pp.

Fa, K., Nguyen, A. V., and Miller, J. D., 2006, "Interaction of calcium dioleate collector colloids with calcite and fluorite surfaces as revealed by AFM force measurements and molecular dynamics simulation," *International Journal of Mineral Processing*, Vol. 81, No. 3, pp. 166-177.

Fischer, P., and Buckingham, A. D., 1998, "Surface second-order nonlinear optical activity," *Journal of the Optical Society of America B*, Vol. 15, No. 12, pp. 2951-2957.

Free, M. L., and Miller, J. D., 1996, "The significance of collector colloid adsorption phenomena in the fluorite/oleate flotation system as revealed by FTIR/IRS and solution chemistry analysis," *International Journal of Mineral Processing*, Vol. 48, No. 3–4, pp. 197-216.

Freysz, E., Du, Q., and Shen, Y. R., 1994, "Sum frequency vibrationnal spectroscopy of water molecules at interfaces," *Annales de physique*, Vol. 19, No. C1, pp. C1-95-C1-102.

Fuerstenau, D. W, and Pradip, "Mineral flotation with hydroxamate collectors," *Reagents in the Mineral Industry*, M. J., Jones, R., Oblatt, ed., 1984, The Institution of Mining and Metallurgy.

Fuerstenau, D. W., Pradip, and Herrera-Urbina, R., 1992, "The surface chemistry of bastnaesite, barite and calcite in aqueous carbonate solutions," *Colloids and Surfaces*, Vol. 68, No. 1–2, pp. 95-102.

Gerdel, M.A., and Smith, R. W., "The role of lignin sulfonate in flotation of bastnaesite from barite," *Rare Earths, Extraction, Preparation and Applications*, R. G., Bautista and M. M., Wong, ed., 1989, TMS.

Goldburg, W. I., 1999, "Dynamic light scattering," *American Journal of Physics*, Vol. 67, No. 12, pp. 1152-1160.

González-Caballero, F., Cabrerizo, M. A., Bruque, J. M., and Delgado, A., 1989, "Flotation properties of celestite in aqueous solutions of ionic surfactants," *International Journal of Mineral Processing*, Vol. 26, No. 1–2, pp. 51-63.

Greenwood, N. N, Earnshaw, A., 1997, *Chemistry of the Elements*, Butterworth Heinemann, 1600 pp.

Gruner, J. W., 1934, "The Crystal structures of talc and pyrophyllite," *Zeitschrift für Kristallographie - Crystalline Materials*, Vol. 88, No. 1, pp. 1-476.

Gupta, V., Nath, S., and Subhash C., 2002, "Role of water structure on phase separation in polyelectrolyte–polyethyleneglycol based aqueous two-phase systems," *Polymer*, Vol. 43, No. 11, pp. 3387-3390.

Rao, K. H., and Forssberg, K. S. E., 1991, "Mechanism of fatty acid adsorption in salt-type mineral flotation," *Minerals Engineering*, Vol. 4, No. 7–11, pp. 879-890.

Heberling, F., Trainor, T. P., Lützenkirchen, J., Eng, P., Denecke, M. A., and Bosbach, D., 2011, "Structure and reactivity of the calcite–water interface," *Journal of Colloid and Interface Science*, Vol. 354, No. 2, pp. 843-857.

Helbig, C., Baldauf, H., Mahnke, J., Stöckelhuber, K. W., and Schulze, H. J., 1998, "Investigation of langmuir monofilms and flotation experiments with anionic/cationic collector mixtures," *International Journal of Mineral Processing*, Vol. 53, No. 3, pp. 135-144.

Herrera-Urbina, R., Pradip, and Fuerstenau, D. W., 2013, "Electrophoretic mobility and computations of solid-aqueous solution equilibria for the bastnaesite-H_2O system," *Minerals and Metallurgical Processing*, Vol. 30, No. 1, pp. 18-23.

Hopkins, A. J., McFearin, C. L., and Richmond, G. L., 2005, "Investigations of the solid–aqueous interface with vibrational sum-frequency spectroscopy," *Current Opinion in Solid State and Materials Science*, Vol. 9, No. 1–2, pp. 19-27.

Houot, R., Cuif, J., Mottot, Y., and Samama, J., 1991, "Recovery of rare earth minerals, with emphasis on flotation process," *Materials Science Forum*, Vol. 70-72, pp. 301-324.

Hu, Y., Lu, Y., Veeramasuneni, S., and Miller, J. D., 1997, "Electrokinetic behavior of fluoride salts as explained from water structure considerations," *Journal of Colloid and Interface Science*, Vol. 190, No. 1, pp. 224-231.

Janczuk, B., Bruque, J. M., Gonzalez-Martin, M. L., and Moreno del Pozo, J., 1993, "Wettability and surface tension of fluorite," *Colloids and Surfaces A: Physicochemical and Engineering Aspects*, Vol. 75, pp. 163-168.

Jang, W. H., and Miller, J. D., 1993, "Verification of the internal reflection spectroscopy adsorption density equation by Fourier transform infrared spectroscopy analysis of transferred Langmuir-Blodgett films," *Langmuir*, Vol. 9, No. 11, pp. 3159-3165.

Jang, W. H., Drelich, J., and Miller, J. D., 1995, "Wetting characteristics and stability of langmuir-blodgett carboxylate monolayers at the surfaces of calcite and fluorite," *Langmuir*, Vol. 11, No. 9, pp. 3491-3499.

Jang, W. H., and Miller, J. D., 1995, "Molecular orientation of langmuir-blodgett and Self-assembled monolayers of stearate species at a fluorite surface as described by linear dichroism theory," *The Journal of Physical Chemistry*, Vol. 99, No. 25, pp.10272-10279.

Kataoka, S., Gurau, M. C., Albertorio, F., Holden, M. A., Lim, S. M., Yang, R. D., and Cremer, P. S., 2004, "Investigation of water structure at the TiO_2/aqueous interface," *Langmuir*, Vol. 20, No. 5, pp. 1662-1666.

Kellar, J. J., Young, C. A., Knutson, K., and Miller, J. D., 1991, "Thermotropic phase transition of adsorbed oleate species at a fluorite surface by in situ FT-IR/IRS spectroscopy," *Journal of Colloid and Interface Science*, Vol. 144, No. 2, pp. 381-389.

Kim, J., Kim, G., and Cremer, P. S., 2001, "Investigations of water structure at the solid/liquid interface in the presence of supported lipid bilayers by vibrational sum frequency spectroscopy," *Langmuir*, Vol. 17, No. 23, pp.255-7260.

Koneshan, S., Jayendran C. R., Lynden-Bell, R. M., and Lee, S. H., 1998, "Solvent structure, dynamics, and ion mobility in aqueous solutions at 25 °C," *The Journal of Physical Chemistry B*, Vol. 102, No. 21, pp. 4193-4204.

Krasowska, M., and Malysa, K., 2007, "Kinetics of bubble collision and attachment to hydrophobic solids: I. Effect of surface roughness," *International Journal of Mineral Processing*, Vol. 81, No. 4, pp. 205-216.

Lam, C. N. C., Ko, R. H. Y., Yu, L. M. Y., Ng, A., Li, D., Hair, M. L., and Neumann, A. W., 2001, "Dynamic cycling contact angle measurements: study of advancing and receding contact angles," *Journal of Colloid and Interface Science*, Vol. 243, No. 1, pp. 208-218.

Lam, C. N. C., Wu, R., Li, D., Hair, M. L., and Neumann, A. W., 2002, "Study of the advancing and receding contact angles: liquid sorption as a cause of contact angle hysteresis," *Advances in Colloid and Interface Science*, Vol. 96, No. 1–3, pp 169-191.

Lambert, A. G., Davies, P. B., and Neivandt, D. J., 2005, "Implementing the theory of sum frequency generation vibrational spectroscopy: A tutorial review," *Applied Spectroscopy Reviews*, Vol. 40, No. 2, pp. 103-145.

Lee, S. H., and Rasaiah, J. C., 1996, "Molecular dynamics simulation of ion mobility. 2. Alkali metal and halide ions using the SPC/E model for water with simple truncation of ion-water potential," *Journal of Physical Chemistry*, Vol. 100, No. 4, pp. 1420-5.

Li, C., 1967, "Solubility and electrokinetic behavior of synthetic bastnaesite., Materials Science and Mineral Engineering," M. S. Thesis, Unviersity of California, Berkeley, CA., 72 pp.

Li, F., Wang, J., and Zeng, X., 1989, "A process on the recovery of RE minerals with a chelating collector," *Rare Earths, Extraction, Preparation and Applications*, R. G., Bautista, M. M., Wong, ed., 1988, TMS.

Liljeblad, J. F. D., and Tyrode, E., 2012, "Vibrational sum frequency spectroscopy studies at solid/liquid interfaces: Influence of the experimental geometry in the spectral shape and enhancement," *The Journal of Physical Chemistry C*, Vol. 116, No. 43, pp. 22893-22903.

López-Valdivieso, A., Robledo-Cabrera, A., and Uribe-Salas, A., 2000, "Flotation of celestite with the anionic collector sodium dodecyl sulfate. Effect of carbonate ions," *International Journal of Mineral Processing*, Vol. 60, No. 2, pp. 79-90.

Lu, R., Gan, W., Wu, B., Zhang, Z., Guo, Y., and Wang, H., 2005, "C−H stretching vibrations of methyl, methylene and methine groups at the vapor/alcohol (n = 1−8) interfaces," *The Journal of Physical Chemistry B*, Vol. 109, No. 29, pp. 14118-14129.

Lu, Y., Drelich, J., and Miller, J. D., 1998, "Oleate adsorption at an apatite surface studied by Ex-Situ FTIR internal reflection spectroscopy," *Journal of Colloid and Interface Science*, Vol. 202, No. 2, pp. 462-476.

Lu, Y., and Miller, J. D., 2002, "Carboxyl stretching vibrations of spontaneously adsorbed and LB-transferred calcium carboxylates as determined by FTIR internal reflection spectroscopy," *Journal of Colloid and Interface Science*, Vol. 256, No. 1, pp. 41-52.

Luo, J., and Chen, X., 1984, "Research into the recovery of high grade rare earth concentrate from Baotou complex iron ore," *Mineral Processing and Extractive*

Metallurgy (Trans. IMM C), edited by Michael, and Gill, ed., Institue of Materials, Minerals and Mining.

MacPhail, R. A., Strauss, H. L., Snyder, R. G., and Elliger, C. A., 1984, "Carbon-hydrogen stretching modes and the structure of n-alkyl chains. 2. Long, all-trans chains," *The Journal of Physical Chemistry*, Vol. 88, No 3, pp. 334-341.

Marinakis, K. I., and Shergold, H. L., 1985, "The mechanism of fatty acid adsorption in the presence of fluorite, calcite and barite," *International Journal of Mineral Processing*, Vol. 14, No. 3, pp. 161-176.

Martínez-Luévanos, A., Uribe-Salas, A., and Lopez-Valdivieso, A., 1999, "Mechanism of adsorption of sodium dodecylsulfonate on celestite and calcite," *Minerals Engineering*, Vol. 12, No. 8, pp. 919-936.

Mayo, S. L., Olafson, B. D., and Goddard, W. A., 1990, "Dreiding: A generic force field for molecular simulations," *The Journal of Physical Chemistry*, Vol. 94, No. 26, pp. 8897-8909.

Melchionna, S., Ciccotti, G., and Holian, B. L., 1993, "Hoover NPT dynamics for systems varying in shape and size," *Molecular Physics*, Vol. 78, No. 3, pp.533-44.

Miller, J. D., and Hiskey, J. B., 1972, "Electrokinetic behavior of fluorite as influenced by surface carbonation," *Journal of Colloid and Interface Science*, Vol. 41, No. 3, pp. 567-573.

Miller, J. D., Misra, M., Yehia, A., and Hu, J. S., 1987, "Fluoride activation in oleate flotation of collophanite," *Minerals and Metallurgical Processing*, Vol. 4, No. 3, pp. 133-139.

Miller, J. D., Hu, J. S., and Jin, R., 1989, "Thermochemistry of oleate adsorption at the fluorite/water interface," *Colloids and Surfaces*, Vol. 42, No. 1, pp. 71-84.

Miller, J. D., Fa, K., Calara, J. V., and Paruchuri, V. K., 2004, "The surface charge of fluorite in the absence of surface carbonation," *Colloids and Surfaces A: Physicochemical and Engineering Aspects*, Vol. 238, No. 1–3, pp. 91-97.

Miranda, P. B., and Shen, Y. R., 1999, "Liquid interfaces: A study by sum-frequency vibrational spectroscopy," *The Journal of Physical Chemistry B*, Vol. 103, No. 17, pp. 3292-3307.

Moulin, P., and Roques, H., 2003, "Zeta potential measurement of calcium carbonate," *Journal of Colloid and Interface Science*, Vol. 261, No. 1, pp. 115-126.

Nickolov, Z., Wang, X., and Miller, J. D., 2004, "Liquid/air interfacial structure of alcohol-octyl hydroxamic acid mixtures: A study by sum-frequency spectroscopy," *Spectrochimica Acta Part A: Molecular and Biomolecular Spectroscopy*, Vol. 60, No. 12, pp. 2711-2717.

Nihonyanagi, S., Ishiyama, T., Lee, T., Yamaguchi, S., Bonn, M., Morita, A., and Tahara, T., 2011, "Unified molecular view of the air/water interface based on experimental and theoretical χ(2) spectra of an isotopically diluted water surface," *Journal of the American Chemical Society*, Vol. 133, No. 42, pp. 16875-16880.

Oberndorfer, J., and Dobiáš, B., 1989, "Adsorption mechanism of anionic surfactants on sparingly soluble minerals," *Colloids and Surfaces*, Vol. 41, No. 0, pp. 69-76.

Orthgiess, E., and Dobiáš, B., 1994, "Complexing agents as modifiers in mineral flotation - mechanism studies," *Colloids and Surfaces A: Physicochemical and Engineering Aspects*, Vol. 83, No. 2, pp. 129-141.

Ostroverkhov, V., Waychunas, G. A., and Shen, Y. R., 2004, "Vibrational spectra of water at water/α-quartz (0001) interface," *Chemical Physics Letters*, Vol. 386, No. 1–3, pp. 144-148.

Ozkan, A., and Yekeler, M., 2004, "Coagulation and flocculation characteristics of celestite with different inorganic salts and polymers," *Chemical Engineering and Processing: Process Intensification*, Vol. 43, No. 7, pp. 873-879.

Pavez, O., Brandao, P. R. G., and Peres, A. E. C., 1996, "Adsorption of oleate and octyl-hydroxamate on to rare-earths minerals," *Minerals Engineering*, Vol. 9, No. 3, pp. 357-366.

Perdikatsis, B, and Burzlaff, H., 1981, "Strukturverfeinerung am talk Mg3[(OH)2Si4O10]," *Zeitschrift fur Kristallographie*, Vol. 156, pp. 177-186.

Pereira, C. A., and Peres, A. E. C., 1997, "Flotation concentration of a xenotime pre-concentrate," *Minerals Engineering*, Vol. 10, No. 11, pp. 1291-1295.

Pradip, 1981, "The Surface Properties and Flotation of Rare-Earth Minerals," Ph. D. Thesis, University of California, Berkeley, CA., 210 pp.

Pradip, and Fuerstenau, D. W., 1983, "The adsorption of hydroxamate on semi-soluble minerals. Part I: Adsorption on barite, calcite and bastnaesite," *Colloids and Surfaces*, Vol. 8, No. 2, pp. 103-119.

Pradip, and Fuerstenau, D. W., 1985, "Adsorption of hydroxamate collectors on semisoluble minerals Part II: Effect of temperature on adsorption," *Colloids and Surfaces*, Vol. 15, No. 0, pp. 137-146.

Pradip, and Fuerstenau, D. W., 1988, "Alkyl hydroxamates as collectors for the flotation of bastnaesite rare-earth ores," *Rare Earths, Extraction, Preparation and Applications*, R. G., Bautista, M. M., Wong, ed., 1988, TMS.

Pradip, and Fuerstenau, D. W., 1991, "The role of inorganic and organic reagents in the flotation separation of rare-earth ores," *International Journal of Mineral Processing*, Vol. 32, No. 1–2, pp. 1-22.

Puchin, V. E., Puchina, A. V., Huisinga, M., and Reichling, M., 2001, "Theoretical modelling of steps on the CaF_2(111) surface," *Journal of Physics: Condensed Matter*, Vol. 13, pp. 2081-2094.

Pugh, R., and Per S., 1985, "Solution chemistry studies and flotation behaviour of apatite, calcite and fluorite minerals with sodium oleate collector," *International Journal of Mineral Processing*, Vol. 15, No. 3, pp. 193-218.

Raghavan, S., and Fuerstenau, D. W., 1975, "The adsorption of aqueous octyl hydroxamate on ferric oxide," *Journal of Colloid and Interface Science*, Vol. 50, No. 2, pp. 319-330.

Rahman, A. 1964, "Correlations in the motion of atoms in liquid argon," *Physical Review*, Vol. 136, No. 2A, pp. A405-A411.

Rao, K. H., Antti, B., and Forssberg, E., 1990, "Mechanism of oleate interaction on salt-type minerals, Part II. Adsorption and electrokinetic studies of apatite in the presence of sodium oleate and sodium metasilicate," *International Journal of Mineral Processing*, Vol. 28, No. 1–2, pp 59-79.

Rao, K. H., Cases, J. M., and Forssberg, K. S. E., 1991, "Mechanism of oleate interaction on salt-type minerals: V. Adsorption and precipitation reactions in relation to the solid/liquid ratio in the synthetic fluorite—sodium oleate system," *Journal of Colloid and Interface Science*, Vol. 145, No. 2, pp 330-348.

Redeker, I. H., and Bentzen, E. H., "Plant and laboratory practice in nonmetallic mineral flotation," In *Chemical Reagents in the Mienral Processing Industry*, D. Malhotra and F. G. William, ed., 1986, Society of Mining Engineers.

Reichling, M., Wilson, R. M., Bennewitz, R., Williams, R. T., Gogoll, S., Stenzel, E., and Matthias, E., 1996, "Surface colloid evolution during low-energy electron irradiation of CaF2(111)," *Surface Science*, Vol. 366, No. 3, pp. 531-544.

Ren, J., Lu, S., Song, S., and Niu, J., 1997, "A new collector for rare earth mineral flotation," *Minerals Engineering*, Vol. 10, No. 12, pp. 1395-1404.

Ren, J., Song, S., Lopez-Valdivieso, A., and Lu, S., 2000, "Selective flotation of bastnaesite from monazite in rare earth concentrates using potassium alum as depressant," *International Journal of Mineral Processing*, Vol. 59, No. 3, pp. 237-245.

Richmond, G. L. 2002. "Molecular bonding and interactions at aqueous surfaces as probed by vibrational sum frequency spectroscopy," *Chemical Reviews* 102 (8):2693-2724.

Rohl, A. L., Wright, K., and Gale, J. D., "Evidence from surface phonons for the (2 × 1) reconstruction of the ($10\bar{1}4$) surface of calcite from computer simulation," *American Mineralogist*, Vol. 88, No. 5-6, pp. 921-925.

Roy, S., and Hore, D. K., 2012, "Simulated structure and nonlinear vibrational spectra of water next to hydrophobic and hydrophilic solid surfaces," *The Journal of Physical Chemistry C*, Vol. 116, No. 43, pp. 22867-22877.

Schick, M., Dabringhaus, H., and Wandelt, K., 2004, "Macrosteps on CaF 2 (111)," *Journal of Physics: Condensed Matter*, Vol. 16, No. 6, pp. L33-L37.

Schrödle, S., and Richmond, G. L., 2008, "In situ non-linear spectroscopic approaches to understanding adsorption at mineral–water interfaces," *Journal of Physics D: Applied Physics*, Vol. 41, No. 3, pp. 033001.

Schwer, C., and Kenndler, E., 1991, "Electrophoresis in fused-silica capillaries: The influence of organic solvents on the electroosmotic velocity and the zeta. potential," *Analytical Chemistry*, Vol. 63, No. 17, pp. 1801-1807.

SHIMADZU, *TOC-V CPH/CPN & TOC-Control V Software User Manual*, SHIMADZU Corporation, Process & Environmental Instrumentation Divsion.

Siffert, D., and Fimbel, P., 1984, "Parameters affecting the sign and magnitude of the eletrokinetic potential of calcite," *Colloids and Surfaces*, Vol. 11, No. 3–4, pp. 377-389.

Smith, R. W., and Shonnard, D., 1986. "Electrokinetic study of the role of modifying agents in flotation of salt-type minerals," *AIChE Journal*, Vol. 32, No. 5, pp. 865-868.

Smith, W., and Forester, T. R., 1996, "DL_POLY user manual," *Journal of Molecular Graphics*, Vol. 14, pp. 136.

Sondi, I., Bišćan, J., Vdović, N., and Škapin, S. D., 2009, "The electrokinetic properties of carbonates in aqueous media revisited," *Colloids and Surfaces A: Physicochemical and Engineering Aspects*, Vol. 342, No. 1–3, pp. 84-91.

Suzuki, T., Hirose, G., and Oishi, S., 2004, "Contact angle of water droplet on apatite single crystals," *Materials Research Bulletin*, Vol. 39, No. 1, pp. 103-108.

Tyrode, E., and Liljeblad, J. F. D., 2012, "Water structure next to ordered and disordered hydrophobic silane monolayers: A vibrational sum frequency spectroscopy study," *The Journal of Physical Chemistry C*, Vol. 117, No. 4, pp. 1780-1790.

Van Loon, L. L., and Allen, H. C., 2004, "Methanol reaction with sulfuric acid: A vibrational spectroscopic study," *Journal of Physical Chemistry B*, Vol. 108, No. 45, pp. 17666-17674.

Van Loon, L. L., Minor, R. N., and Allen, H. C., 2007, "Structure of butanol and hexanol at aqueous, ammonium bisulfate, and sulfuric acid solution surfaces investigated by vibrational sum frequency generation spectroscopy," *Journal of Physical Chemistry A*, Vol. 111, pp. 7338-46.

Verreault, D., Hua, W., and Allen, H. C., 2012, "From conventional to phase-sensitive vibrational sum frequency generation spectroscopy: Probing water organization at aqueous interfaces," *The Journal of Physical Chemistry Letters*, Vol. 3, No. 20, pp. 3012-3028.

Viswanathan, K. V., Shukla, S. K., and Majumdar, K. K., 1970, "Adsorption of long chain electrolytes at the solid-liquid interface. Part I: The adsorption of monazit-water system," *Transactions of the Indian Institute of Metals*, pp. 6-10.

Wang, H., Gan, W., Lu, R., Rao, Y., and Wu, B., 2005, "Quantitative spectral and orientational analysis in surface sum frequency generation vibrational spectroscopy (SFG-VS)," *International Reviews in Physical Chemistry*, Vol. 24, No. 2, pp. 191-256.

Wang, J., Clar, C. R., and Schreiber, H., 2007, "Extended lifetime of fluoride optics," *Proceedings SPIE 6720, Laser-Induced Damage in Optical Materials*, J. E. Gregory, A. H., Guenther, K. L., Lewis, D., Ristau, M. J., Soileau, C. J. Stolz, ed., 2007, Society of Photo Optical.

Wang, J., and Maier, R. L., 2004, "Color center formation on CaF2 (111) surface investigated by low-energy-plasma-ion surfacing," Frontiers in Optics 2004/Laser Science XXII/Diffractive Optics and Micro-Optics/Optical Fabrication and Testing, October , 2004, Rochester, New York, Optical Society of America.

Wang, X., 2004, "The Surface Chemistry of Phosphate Mineral Flotation with Alcohol Solutions of Octyl Hydroxamic Acid," Ph. D. Thesis, Univerity of Utah, Salt Lake City, UT., 220 p.

Wang, X., Liu, J., and Miller, J. D., 2008, "Adsorption and self-assembly of octyl hydroxamic acid at a fluorite surface as revealed by sum-frequency vibrational spectroscopy," *Journal of Colloid and Interface Science*, Vol. 325, No. 2, pp. 398-403.

Werder, T., Walther, J. H., Jaffe, R. L., Halicioglu, T., and Koumoutsakos, P., 2003, "On the water−carbon interaction for use in molecular dynamics simulations of graphite and carbon nanotubes," *The Journal of Physical Chemistry B*, Vol. 107, No. 6, pp. 1345-1352.

Wolfrum, K., Graener, H., and Laubereau, A., 1993, "Sum-frequency vibrational spectroscopy at the liquid—air interface of methanol. Water solutions," *Chemical Physics Letters*, Vol. 213, No. 1–2, pp. 41-46.

Wu, L., and Forsling, W., 1995, "Surface complexation of calcium minerals in aqueous solution. III. Ion exchange and acid-base properties of hydrous fluorite surfaces," *Journal of Colloid and Interface Science*, Vol. 174, No. 1, pp. 178-184.

Ye, S., Nihonyanagi, S., and Uosaki, K., 2001, "Sum frequency generation (SFG) study of the pH-dependent water structure on a fused quartz surface modified by an

octadecyltrichlorosilane (OTS) monolayer," *Physical Chemistry Chemical Physics*, Vol. 3, No. 16, pp. 3463-3469.

Yeganeh, M. S. Dougal, S. M., and Pink, H. S., 1999, "Vibrational spectroscopy of water at liquid/solid interfaces: Crossing the isoelectric point of a solid surface," *Physical Review Letters*, Vol. 83, No. 6, pp. 1179-1182.

Yin, X., 2012, "Anisotropic Surface Features of Selected Phyllosilicates," Ph.D. Thesis, University of Utah, Salt Lake City, UT., 155 pp.

Yörükoğlu, A., Obut, A., and Girgin, I., 2003, "Effect of thiourea on sulphuric acid leaching of bastnaesite," *Hydrometallurgy*, Vol. 68, No. 1–3, pp. 195-202.

Young, C.A., and Miller, J. D., "In-situ FT-IR/IRS and MLRS examination of adsorbed oleate at fluorite and calcite surfaces," TMS Annual Meeting, 1999, San Diego, California.

Zawala, J., Drzymala, J., and Malysa, K., 2007, "Natural hydrophobicity and flotation of fluorite," *Physicochemical Problems of Mineral Processing*, Vol. 41, pp. 5-11.

Zawala, J., Drzymala, J., and Malysa, K., 2008, "An investigation into the mechanism of the three-phase contact formation at fluorite surface by colliding bubble," *International Journal of Mineral Processing*, Vol. 88, No. 3-4, pp. 72-79.

Zembala, M., and Adamczyk, Z., 1999, "Measurements of streaming potential for mica covered by colloid particles," *Langmuir*, Vol. 16, No. 4, pp. 1593-1601.

Zhang, X., Wang, X., Yin, X., Du, H., and Miller, J. D., "Interfacial chemistry features of selected fluorite surfaces," *International Symposium on Separation Technologies for Minerals, Coal, and Earth Resources*, February 27, 2011 - March 2, 2011, Denver, CO, SME.

Zhu, X. D., Suhr, H., and Shen, Y. R., 1987, "Surface vibrational spectroscopy by infrared-visible sum frequency generation," *Physical Review B*, Vol. 35, No. 6, pp. 3047-3050.

Zhuang, X., Miranda, P. B., Kim, D., and Shen, Y. R., 1999, "Mapping molecular orientation and conformation at interfaces by surface nonlinear optics. *Physical Review B*, Vol. 59, No. 19, pp. 12632-12640.